Testing and Modelling of the Mechanical Properties of Fibre-matrix Interfacial Transition Zone

Yanchen He

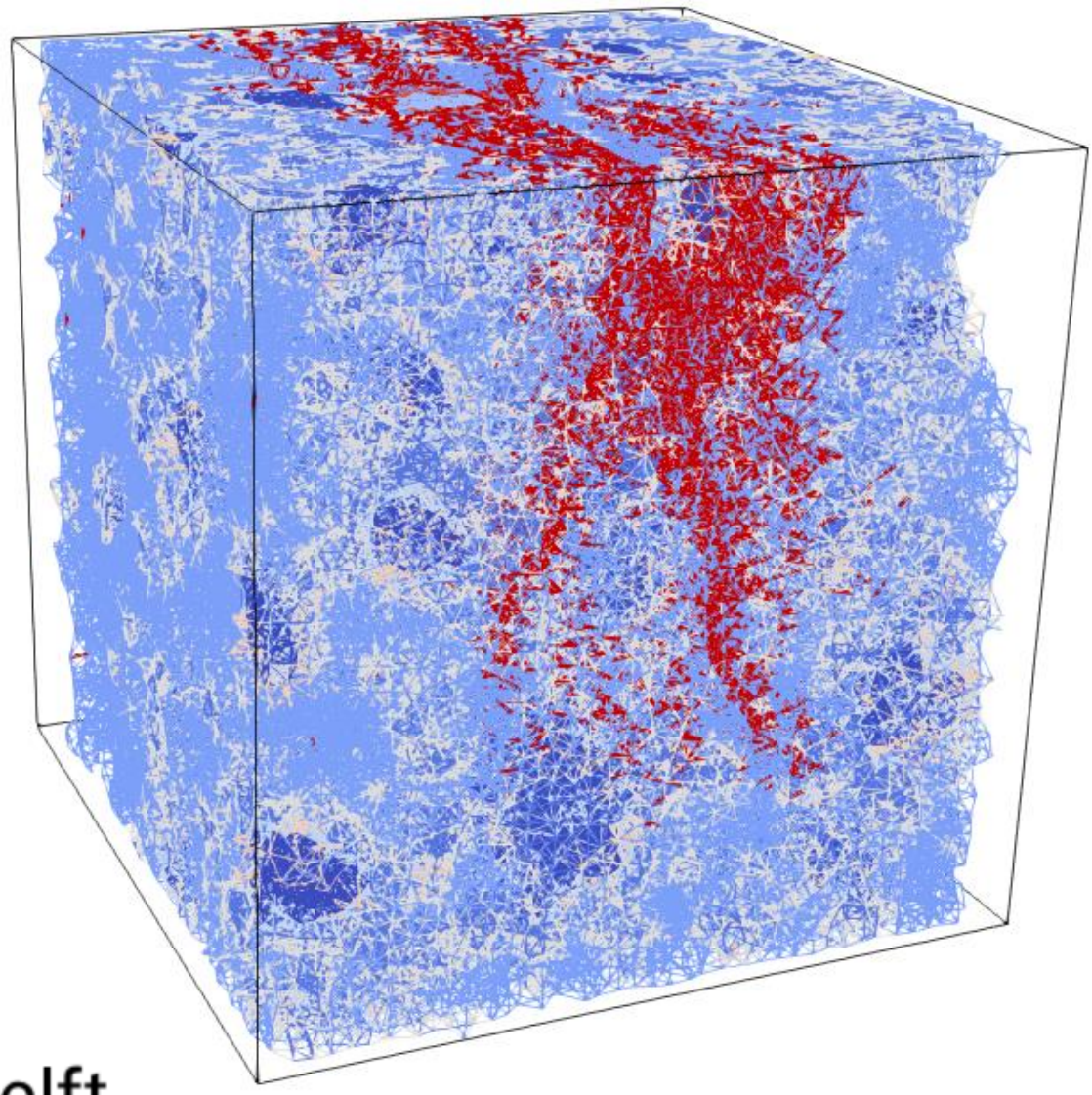

TU Delft

Testing and Modelling of the Mechanical Properties of Fibre-matrix Interfacial Transition Zone

by

Yanchen He

To obtain the degree of Master of Science
at the Delft University of Technology
to be defended publicly on July 31, 2024 at 09:45

Student number: 5708400

Thesis committee:

Prof. Dr. Ir. E. Schlangen	TU Delft, Chair and Supervisor
Dr. Ir. M. Lukovic	TU Delft
Shan He	TU Delft, Daily Supervisor

Abstract

The Interfacial Transition Zone (ITZ) in Fiber Reinforced Concrete (FRC) is the microscopic zone between the fibres and the cement matrix, which is essential to the overall performance of the composites. To explore the micro-mechanical properties of the ITZ, a combined experimental and numerical study was carried out targeting this microscopic area. Specifically, an indentation splitting test was developed and the single fibre pullout test was conducted. Those two test methods were then simulated to give a comprehensive understanding of the mechanical behaviour and fracture patterns of the interface.

For the indentation splitting test, micro-cubes (300 μm long) containing a segment of vertically aligned microfibre were prepared using CEM I, CEM III and CEM III mixed with limestone powder at varying water-to-cement (w/c) ratios from 0.3 to 0.5. These specimens were then subjected to a splitting test under a nano-indenter equipped with a wedge tip, and the results were compared to those of microcubes without fibres. Mechanical properties including load capacity, deformation at peak, stiffness and fracture energy were analysed. Following the experiment, lattice models with simplified and realistic microstructure were built. For the lattice model with simplified microstructure, the mechanical properties of local phases were calibrated with the experimental results. The modelling result shows that the material properties of the ITZ are approximately equivalent to 20% of the paste properties regardless of the w/c ratio. The lattice models with realistic microstructure were built based on 3D CT scans of the micro prisms. For the lattice model with real microstructure, two material assignment methods, thresholding and greyscale mapping, were compared. The simulation results showed significant differences between the two methods, which may be attributed to the empirical parameters used to calculate tensile strength.

Furthermore, the single fibre pullout test was conducted to examine the interphase properties and compared with the experimental result of the indentation splitting tensile test. Results show that CEM I demonstrates the highest chemical bond energy (G_d) among the tested materials, decreasing significantly with an increase in the w/c ratio. In contrast, CEM III+L displays an inconsistent trend, with the highest G_d observed at a w/c ratio of 0.4. However, the experimental results for frictional bond strength (τ_0) and slip-hardening coefficient (β) do not exhibit

significant trends or differences. The simulation of single fibre pullout accurately captures the initial load phases up to full debonding.

The developed indentation splitting test offers a valuable method for assessing the tensile properties of the ITZ. The modelling results indicate that the mechanical properties of the ITZ are approximately 20% of those of the bulk paste. This finding can be integrated into larger-scale simulations by incorporating the effects of the ITZ. Coupled with the lattice model, this approach provides an effective way to enhance the fibre-matrix ITZ of FRC. Additionally, the insights from this study can be leveraged to optimize the design and performance of FRC, potentially leading to cost savings and extended durability in construction projects.

Contents

ABSTRACT ..... **I**

CONTENTS ..... **III**

1. INTRODUCTION **1**

1.1 Background information 2

1.2 Problem Statement 2

1.3 Research Objectives and Scope 3

1.4 Outline of the Thesis 3

2. LITERATURE REVIEW **5**

2.1 Fibre Reinforced Concrete 6

2.2 Bonding Properties of the Interfacial Transition Zone 7

2.3 Micromechanical Testing and Characterization 10

2.4 Models of the Mechanical Behaviour of ITZ 12

3. TESTING OF MICRO-CUBES ON INDENTATION-SPLITTING BEHAVIOUR **14**

3.1 Introduction 15

3.2 Materials and Tests 15

3.2.1 Materials *15*

3.2.2 Sample Preparation *16*

3.2.3 Test *17*

3.3 Result and Discussion 19

3.3.1 Microstructural Characterisation *19*

3.3.2 Mechanical Properties of Micro-cubes *21*

3.3.3 Influence of Fibre Inclusion *32*

3.4 Conclusions 35

4. MODELLING OF MICRO-CUBES ON INDENTATION SPLITTING BEHAVIOUR **36**

4.1 Introduction 37

4.2 Modelling Approach 37

4.2.1 Lattice Model with Simplified Microstructure *38*

4.2.2 Lattice Model with Real Microstructure *43*

4.3 Results and Discussion 47

4.3.1 Lattice Model with Simplified Microstructure *47*

4.3.2 Lattice Model with Real Microstructure *53*
4.4 CONCLUSIONS 57
5. TESTING AND MODELLING ON SINGLE FIBRE PULLOUT BEHAVIOUR 58
5.1 INTRODUCTION 59
5.2 MATERIALS AND TESTS 59
5.2.1 Materials and Sample Preparation *59*
5.2.2 Test *59*
5.2.3 Modelling Approach *61*
5.3 RESULT AND DISCUSSION 62
5.3.1 Experimental Result *62*
5.3.2 Modelling Result *66*
5.4 CONCLUSIONS 68
6. CONCLUSION AND RECOMMENDATIONS 70
6.1 CONCLUSION 71
6.2 RECOMMENDATIONS 72
APPENDIX 74
A. THE EXPERIMENTAL RESULTS OF THE SINGLE FIBRE PULLOUT TEST 74
BIBLIOGRAPHY 83

1

Introduction

Chapter 1 introduces the research background along with the motivation, and the research problem, objective and scope are also discussed.

1.1 Background information

Fibre-reinforced concrete (FRC) is concrete that has randomly aligned fibres dispersed through it, as specified by ACI 116R, Cement and Concrete Terminology [1]. Leveraging the inherent benefits of fibres, including exceptional tensile strength, high toughness, and high durability, FRC could defer the initiation of cracks and decelerate crack propagation effectively. Literature indicates that polypropylene (PP), polyethene (PE), and polyvinyl alcohol (PVA) fibres are the most widely used synthetic fibres in cementitious composites [2-6]. Even with a wealth of information on durability and mechanical performance, an in-depth knowledge of the microstructural alterations brought about by the addition of polymeric fibre to the cementitious system is still lacking.

1.2 Problem Statement

The quasi-brittle nature of cement-based materials has caused poor performance of concrete in tension. Even at a low level of tensile stress, cracks can initiate and degrade concrete properties over time. Fibre reinforcement has, therefore, been used in concrete to overcome brittleness and to extend its service life. Leveraging the inherent benefits of fibres, including exceptional tensile strength, high toughness, and high durability, FRC could defer the initiation of the first crack and decelerate crack propagation effectively. Common types of fibres used in FRC include polymer fibres, steel fibres, carbon fibres, and natural fibres. Among these, polymer fibres are the most widely used synthetic fibres in cementitious composites. Even with a wealth of information on durability and mechanical performance at the macro scale, there remains a lack of in-depth knowledge about the microstructural alterations brought about by the addition of polymeric fibre to the cementitious system.

The Interfacial Transition Zone (ITZ) in FRC is the microscopic zone between the fibres and the cement matrix, which is essential to the overall performance of the composites. Due to its porous nature, it is commonly believed that the ITZ represents a weak link among constituents governing the mechanical properties of the composite [7]. Fibres primarily exhibit two failure mechanisms: cohesive failure and adhesive failure. In the case of adhesive failure, debonding occurs at the contact surface between the fibre and cement. On the other hand, for cohesive failure, debonding predominantly occurs within the heterogeneous ITZ [8]. In instances where fibres possess a hydrophilic surface (PVA fibres in this case), the bond failure is primarily governed by a cohesive fracture within the transition zone [9]. To enhance the fracture resistance to cohesive failure, the appropriate bond properties are required for the high energy

absorption through the debonding and pure friction phase of fibres [10-12]. A poor bond can lead to inefficient load and energy transmission between the matrix and fibre, whereas an excessive bond might minimize the composite fracture energy owing to fibre rupture. Therefore, the efficiency of force transfers between fibre and matrix plays a critical role in the overall performance of FRC structures. Therefore, the evaluation of ITZ properties is particularly important to enhance the overall material properties of FRC.

In previous studies, the nano-indentation and fibre pullout tests were conducted to assess the bonding properties of the fibre-matrix interfacial transition zone [13-17]. Nano-indentation provided data on the elastic modulus and hardness of each ITZ phase, while the fibre pullout test yielded information on debonding load and debonding energy. However, there is a gap between the length scale of these two testing methods, namely at the nanoscale and the mesoscale. The mechanical properties of the ITZ have never been thoroughly investigated. Therefore, it is expected that the studies on ITZ of fibre-matrix at the micro-scale could fill the gap between nanoscale and mesoscale.

1.3 Research Objectives and Scope

This research aims to obtain the tensile properties of the ITZ between microfibre and cement-based matrix and to develop a numerical model that can simulate the behaviour of ITZ. Specifically, the tensile properties of the ITZ were investigated by performing an indentation-splitting tensile test on micro-prims. The tensile properties encompass micro-splitting tensile strength, bonding strength, and pullout energy. In addition, a lattice model was also applied to simulate splitting and fibre pullout behaviour. Once the model is validated by the experimental result, the obtained mechanical properties of the ITZ can be used as input for the single fibre pullout test or upscaled for future studies that consider the ITZ phase.

1.4 Outline of the Thesis

To achieve the research aim, this thesis is subdivided into six chapters. Chapter 1 introduces the research background along with the motivation, and the research problem, objective and scope are also discussed. Chapter 2 provides a review of studies focusing on the fibre-matrix ITZ, summarizing various mechanical tests and their limitations. The analytical and numerical models of the ITZ have also been reviewed. In Chapter 3, experimental details including the materials used are discussed, and the results of the indentation splitting tensile test are presented in this chapter. Following that, the simulation of the indentation splitting tensile test was applied

to investigate the mechanical behaviour and fracture propagation within the microcubes in Chapter 4. Chapter 5 details the experimental and modelling procedures and results of the single fibre pullout test, discussing the relationship between the microscale test results and the outcomes of the pullout test. Finally, Chapter 6 summarizes the conclusions drawn from both experimental and numerical results and proposes recommendations for future research.

2

Literature Review

Chapter 2 provides a review of studies focusing on the fibre-matrix ITZ, summarizing various mechanical tests and their limitations. The analytical and numerical models of the ITZ have also been reviewed.

2.1 Fibre Reinforced Concrete

Concrete is the most widely used building material in the world due to its low cost and ease of production. Despite its excellent compressive properties, concrete exhibits poor tensile strength and high brittleness which makes it easier to crack and less durable. To mitigate these shortcomings, a lot of studies have been conducted to incorporate fibres into the matrix. The fibre-reinforced cementitious composites (FRCC) were first investigated by Romualdi and Mandel and subsequently drew interest on a global scale [18]. The inclusion of fibre could effectively bridge crack surfaces and contribute to the overall strength and durability of the material. Over the last couple of decades, there has been a growing interest among researchers to develop strain hardening fibre reinforced cementitious composites (SHFRCC) containing randomly distributed short fibres of relatively low-volume fractions. Naaman and Shah [19] created FRCCs that achieved strain-hardening behaviour in tension by incorporating a high volume (2–2.5%) of macro steel fibres with a length of 25 mm. For an extended period, engineering cementitious composites (ECC), which were created by Li in the 1990s [20], have been regarded as representative strain-hardening cementitious composites (SHCC) due to their outstanding tensile ductility, which exceeds 300 times that of conventional concrete [21]. A high-modulus polyethylene (PE) fibre, Spectra, was utilised in the development of the initial version of ECC. This fibre demonstrated a tensile strain capacity of 5.6% and a compressive strength of 65.6 MPa [22]. A structural ECC based on polyvinyl alcohol (PVA) fibre was introduced by Li et al. [23] in the early 2000s. This ECC displayed a tensile strength of up to 5.0 MPa and a strain capacity of up to 4.6%. The surface of the PVA fibre was modified through oil coating to prevent rupture in the cementitious matrix as a result of strong chemical bonding. As illustrated in Fig. 2.1, a PVA-ECC that is suitable must exhibit a tensile strain capacity of over 4% with saturated multiple fractures. Depending on the matrix composition, the compressive strength of ECCs is known to range from 30 to 70 MPa [24].

It is also well concerned with the development of high-performance concrete , particularly for the heavily loaded lower-story columns of concrete structures and lighter beams with shallower sections [25]. However, concrete that is densely packed or has high compressive strength is more brittle; certain HSC structures have demonstrated an increased propensity for early-age cracking. Richard and Cheyrezy developed ultra-high-performance fibre-reinforced concrete (UHPFRC) in the mid-1990s to attain both high ductility and ultra-high-strength properties (f'_c of greater than 150 MPa [26]. It has been regarded as one of the most effective construction materials due to its exceptional mechanical strengths, ductility, durability, and fatigue resistance. The incorporation of 2% (by volume) micro straight steel fibres can overcome the

high brittleness of ultra-high strength matrix (f_c > 150 MPa), resulting in strain-hardening behaviour in tension. The strain capacity of UHPFRC with conventional micro straight steel fibres is approximately 0.44% in Fig. 2.1 [27]. This capacity can be increased by up to approximately 0.8% by utilising long straight or twisted steel fibres [28].

To develop high-strength cementitious composites that exhibit a tensile strain capacity comparable to that of ECC, which is approximately 4% (as shown in Fig. 2.1), it is essential to focus on the formulation of high-performance Strain-Hardening Cementitious Composites (SHCC). These advanced materials must not only achieve high strength but also maintain superior ductility and durability. For high-performance SHCCs, the minimum required compressive strength has been determined to be 55 MPa, alongside a tensile strain capacity of at least 4% [27]. This combination ensures that the composites can endure significant tensile deformations while maintaining structural integrity, thereby enhancing their application potential in demanding structural environments where both strength and flexibility are crucial.

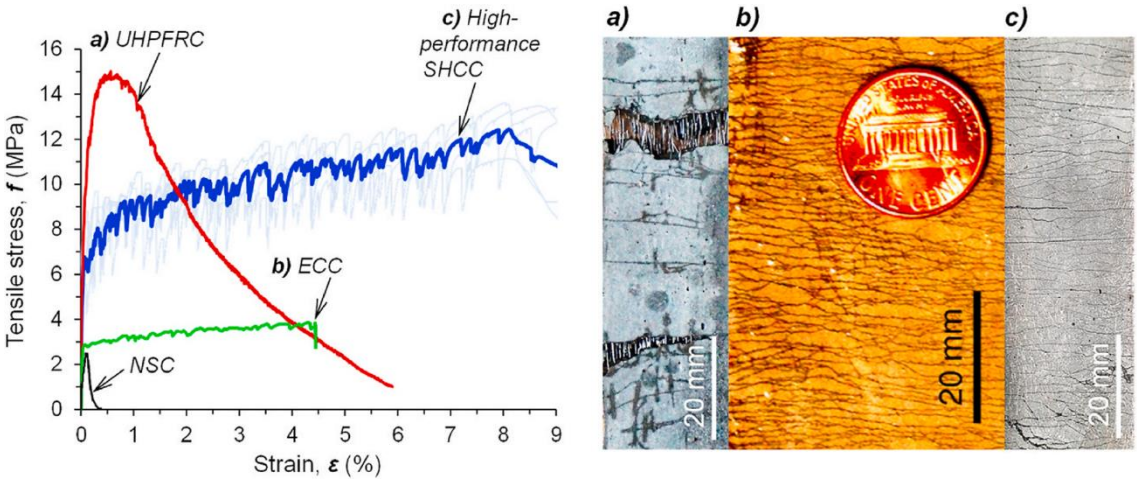

Fig. 2.1 Comparative tensile stress-strain curves and crack patterns of UHPFRC, ECC, and high-performance SHCC [27]

2.2 Bonding Properties of the Interfacial Transition Zone

The ITZ in FRC is the microscopic zone of the cement-based matrix surrounding the microfibres, which has a more porous microstructure as compared to the bulk matrix. Due to this porosity, it is commonly believed that the ITZ represents a weak link among constituents. Since the efficiency of force transfers between fibre and matrix plays a critical role in the overall performance of FRC structures, the properties of the ITZ govern the overall mechanical properties of the composite [7].

The bonding property of the fibre-matrix ITZ is widely acknowledged to have a significant impact on the mechanical performance of FRC at multiple scales [14, 29, 30]. The stress-strain relationship determines the response of the structure at the macroscale. At a smaller scale, known as the mesoscale, it is possible to observe the combination of fibres and the concrete matrix, which includes the aggregate and cementitious matrix. The fracture resistance of FRC is primarily determined by the strength of the concrete matrix. However, the behaviour of FRC after cracking is influenced independently by the parameters of fibre reinforcement and the bond between the fibre and the matrix. While exposed to tensile stress, it can be separated into two components. One component is resisted by the concrete matrix, while the second component is resisted by the fibres [31]. The stress distribution in fibres is affected by the ability of stress transfer between fibres and the cementitious matrix, which is governed by the bonding property [32]. Moreover, the nanostructure within the ITZ has a significant influence on the bonding characteristics at the nanoscale, ultimately impacting the mechanical properties of FRC [14].

The failure modes of the interface between the fibre and matrix can generally be classified into three groups based on the location of the failure: debonding failure, fibre failure, and matrix failure. Fig. 2.2shows the three failure modes (a, b, c) of the fibre–matrix interface [33]. Cracks develop until they reach the interface and continue to grow when the fibre is fractured or pulled out when structures are subjected to tensile load [34]. In this process, the friction, adherence, and anchoring force between the fibres and matrix generate forces that aim to prevent slippage. In Fig. 2.2a, the pullout phenomenon of fibres at lower loads will result from a weak bond between the matrix and fibre surface, and fibres are unable to make any significant contribution to the development of cracks and are more likely to debond from the matrix. In contrast, the mechanical performance of the FRC would be enhanced by the stress transmission from the concrete matrix to the fibre, which would be facilitated by a relatively strong bonding property. However, the fibre cannot completely contribute to the post-crack strength when the fibre–matrix bond becomes excessively strong, as this results in the rupture of fibres, as shown in Fig. 2.2b. Consequently, the overall efficacy of FRC structures is significantly influenced by the efficiency of force transfers between the fibre and matrix. This critical function of the fibre is accomplished by ensuring the transmission of forces between the relatively brittle concrete matrix and the fibre [35].

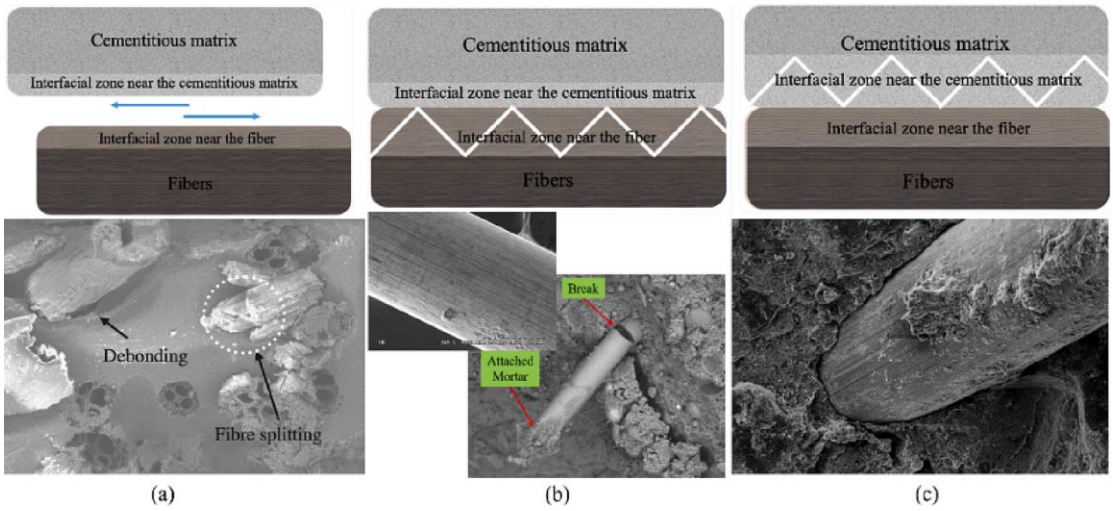

Fig. 2.2 Failure modes of fibre–matrix interface: (a) debonding failure, (b) failure in fibres, (c) failure in the cementitious matrix. [33]

The theory of adhesion, which is associated with the bonding mechanism, is an investigation of the bonding behaviour between the concrete matrix and fibres. The atomic arrangement, molecular conformation, and chemical composition of the matrix and fibres are not the only factors that determine the mechanisms of bonding behaviour; the morphological characteristics of the fibres and the interlocking ability of the matrix and fibres also play an important part [36-38]. Numerous theories have been created to date to understand the mechanism of interfacial bonding. Each of them has a unique hypothesis that serves as a comprehensive explanation of the bonding phenomenon and excludes alternative explanations. The primary obstacle to the development of a comprehensive bonding theory is the inability to precisely characterize the matrix-fiber interaction zone. The mechanical and physicochemical properties of the interfacial zone, which are covered by the outer materials, remain challenging to quantify, although scientific advancements have introduced a variety of sophisticated instruments for analyzing the interface features [33]. Electrostatic attraction, chemical bonding, and mechanical interlocking are the primary bonding mechanisms associated with the interaction between the fibre and cementitious matrix [39]. Electrostatic attraction and chemical bonding exist on a nanoscale at the matrix-fibre interface, while mechanical bonding can occur on a wider length scale at the contact surface, ranging from microns to millimetres. Electrostatic bonding is the interaction of the opposite charges (cationic and anionic) at the contact surface of the matrix and fibre, leading to electrostatic attraction. Consequently, an interface forms that consists of two charged layers. The bonding strength is determined by the charge density. This action may be essential if the surface of the fibre is treated with a coupling agent, although it cannot significantly impact the interface's bonding strength in cementitious materials. Chemical bonding is predicated on the primary bonding at the contact surface, which includes atomic and

ionic bonds, while physical bonding is predicated on acid-based interactions or Van der Waal forces. The substrate's surface chemistry determines the available chemical bonding.

The previous research on fibre–matrix composites and small-scale chemical bonding at the interface did not receive sufficient attention. Nevertheless, chemical reactions at the interface are a critical component of interfacial connection. The introduction of one or more functional groups to the fibre surface would be beneficial to improve the fibre–matrix ITZ by developing new surface treatment methods that are stronger than and bridge over the ITZ [40, 41]. When the matrix penetrates and latches onto the substrate's peaks, holes, fissures, or other imperfections, the mechanical interlocking mechanism characterizes the bonding. It is the primary bonding resource at the fibre–matrix interface for fibre-reinforced cementitious composites, dominantly influencing the shape of the R-curve and the fracture resistance of the composites. The R-curve illustrates the relationship between the stress intensity factor and actual crack extension [42, 43]. This bonding behaviour can occur on a broader length scale at the contact surface, ranging from microns to millimetres. Many internal stresses in cementitious composites occur in addition to the basic geometrical factors. These can be generated by the shrinkage of the cementitious matrix, the difference in thermal expansion between the fibres and the matrix during the cooling process, or chemical processes, such as alkali-silica reaction (ASR) expansion [44], which can improve the mechanical interlocking. The clamping pressure induced by shrinkage is a critical factor that should be taken into account when measuring the frictional stresses during the fibre pullout process [45].

2.3 Micromechanical Testing and Characterization

To understand the load transfer and failure mechanism at the ITZ, micromechanical tests (e.g, micro-indentation, fragmentation and pullout tests) are usually applied. Mandell et al. [46] applied the micro-indentation method to measure the debonding force in situ firstly on the fibre-reinforced polymer composites. Similar to existing nano-indentation tests, a steel probe was employed to apply a load on the surface of the sample. However, due to constraints in specimen preparation and testing techniques, it is necessary to verify the occurrence of fibre debonding through multiple surface checks. Moreover, the debonding tends to transpire on a larger scale, involving a ring of 6-7 fibres, thereby requiring improvement in both reliability and reproducibility. Recent reports document the utilization of nanoindentation as a versatile instrument for loading micrometre-sized specimens. The elastic modulus and hardness of each phase in fibre-matrix ITZ are characterized by applying nanoindentation [13-15, 47, 48]. However, the relation between nanoindentation results and the input local mechanical

properties for different phases is always debated, and it is necessary to measure the mechanical properties.

Kelly and Tyson [49] introduced the fragmentation test, which was later expanded to include composites by Fraser et al. [50]. The fragmentation of the sample proceeds, until the fragment length reaches a critical value, at which point the load, is transferred by shear. The sample is subjected to a monofilament tensile test along the fibre's axis during the test. This method is straightforward to implement and is particularly advantageous for evaluating the shear strength of the fibre–matrix interface, particularly when the interface is strong.

The pullout test is one of the oldest methods to test the interface properties. With significant advancements and improvements in recent years, the pullout test has been developed as a micromechanical test used to evaluate interfacial fibre-matrix bonding. It involves evaluating the force required for extracting a monofilament fibre from its matrix sheath by performing a tensile test on the material that is partially embedded [4, 33]. The pullout force, which is associated with the breakdown phenomena at the interface, is recorded as the debonding load when it reaches its critical value. Two important criteria that are utilised to assess the pullout process are the maximum debonding load and the debonding energy, both of which heavily depend on the mechanical properties of ITZ. The obstacle lies in connecting this experimental quantity to a specific parameter of ITZ. Owing to technical and instrumental limitations, research on the ITZ of fibre-matrix is primarily conducted through simulations. As a result, the mismatch in the examined scale length makes it impossible to validate these models. Consequently, micro-scale experimental data are required to validate and calibrate the micromechanical modelling of the ITZ. Therefore, it is expected that the studies on ITZ of fibre-matrix at micro-scale could fill the gap between nanoscale and mesoscale (single fibre pullout test).

Owing to technical and instrumental limitations, research on the ITZ of fibre-matrix is primarily conducted through simulations. As a result, the mismatch in the examined scale length makes it impossible to validate these models. Thus, micro-scale experimental data become essential for the validation and calibration of micromechanical models of the ITZ. H. Zhang et al. introduced a micro-cube indentation splitting test method, from which the nominal splitting tensile strength is inferred based on the peak load observed in the load-displacement curve [51]. The same micro-cube fabrication technique was applied in this study to investigate the splitting tensile strength of the ITZ, incorporating the newly proposed fibre mid-position method by the authors. Additionally, the wedge indentation test has been applied in other domains to study

the fracture behaviour of specific materials, including cortical bone [52] and silica glass fibre [53].

2.4 Models of the Mechanical Behaviour of ITZ

Analytical and numerical methods are employed by numerous researchers to investigate the bonding behaviours in addition to experiments. The load-displacement behaviour of fibre pullout experiments and the inherent interfacial properties have been predicted using a variety of theoretical models [54-56]. generally, these solutions are attained by relying on a limited number of simple assumptions. The state of plane strain [57] in the assembly is a frequently used assumption to establish the relation between radial and shear stresses in the equilibrium equations. Nevertheless, the plane-strain assumption is not a reliable approximation for interfaces that are precisely bonded and have a load transfer length that is exceedingly short (a few fibre radii). Another such simplification is the ignoring of the radial dependence of axial stresses, either in the matrix or the fibre or in both. This is allowed only when the embedded fibres are adequately long. Owing to the mathematically involved nature of this boundary value problem, a few investigators have chosen to impose boundary conditions in an approximate sense. For example, Hsueh [58-60] developed an analytical solution that was based on the shear-lag theory. Nairn (1997) [61] demonstrated that the shear-lag analysis is most appropriate for composites with a high fibre-to-matrix stiffness ratio. Additionally, composites with low fibre volume fractions are predicted to yield inaccurate results by a shear-lag analysis. Nevertheless, the total energy prediction obtained through shear-lag analysis is relatively precise; as a result, a shear-lag theory has been employed to investigate the fracture mechanics of embedded fibres [62].

Many researchers have modelled the interphase region as a homogeneous material in order to produce tractable models. Nevertheless, a small number of studies have taken into account the inhomogeneous character of interphase by adopting a stair-case variation of material properties across the thickness of the interphase layer [63, 64]. Alternately, a few researchers proposed an effective interphase model (EIM) and a uniform replacement model (URM) to replace the fibre and the surrounding interphase with an effective homogeneous fibre to convert a three-phase composite into a two-phase composite [65]. Several researchers regarded the interphase as an inhomogeneous material by smoothly varying the material properties as a function of radius, for mathematical convenience and to more accurately reflect the variation of properties within the interphase region. The material properties are typically evaluated in these models by implementing an empirical law [66, 67]. Given the difficulty of obtaining an explicit closed-

form 3D solution for such problems, numerous researchers have implemented numerical methods, particularly FE analysis [68-70]. Arain et al. [68] designed a 2D axis-symmetric model to simulate the single fibre pullout behaviour. The linear elastic behaviour is considered for the interface properties between the fibre and the cementitious matrix, and the interface was designed as a perfectly bonded zero thickness pair using the CONTA172 and TARGE169 by cohesive zone model (CZM) Mode-II. Chaohui et al. [69] proposed a modified interfacial friction law considering an enhancement factor. The friction, which is caused by interfacial pressure between fibre and matrix, was considered in the analytical models for different shaped fibres. While previous models have made significant advances in simulating fibre pullout behaviour, ITZ is frequently regarded as a homogenized phase in simulations, even though it is the primary determinant. The cohesive contact within the ITZ is primarily determined by the chemical bond, specifically the hydrogen bonds that are formed between the fibre and various hydration phases. The constitution of hydration products is dependent upon the ITZ structure of various material compositions. Furthermore, the sliding behaviour and pullout strength of the fibre are influenced by the porosity and strength of each phase in the ITZ. Given that the microscale is the critical scale for researching and comprehending the fracture behaviour of ITZ [71, 72], the analysis and comprehension of the fibre pullout behaviour are improved by considering the microstructure of ITZ. Additionally, the numerical model exhibits improved generality and reliability when the actual microstructure is taken into account [73, 74].

3

Testing of Micro-cubes on Indentation-splitting Behaviour

In Chapter 3, experimental details including the materials used are discussed, and the results of the indentation splitting tensile test are presented in this chapter.

3.1 Introduction

The effects of microfibre inclusion on the tensile properties of ITZ were investigated in this chapter. For this purpose, a fibre positioning and micro-dicing technique was developed to prepare micro-cube specimens containing a single filament of PVA fibre. Considering that the thickness of the fibre-matrix ITZ is usually around 100-150 μm [18-20], the length of microcubes was chosen as 300 μm. To investigate the tensile behaviour of ITZ, the micro-splitting tensile test was conducted by applying a line force at the centre of the top surface using a wedge tip mounted on a nanoindenter. The microstructure features and porosity of the ITZ were characterised by X-ray computed tomography (XCT). The fracture pattern of fibre/without fibre specimens was examined by Scanning Electron Microscope (SEM).

3.2 Materials and Tests

3.2.1 Materials

The materials involved in this study include the CEM I 42.5 N, limestone powder and CEM III/B 42.5 N. Table 1 presents the material and experimental mix proportions applied. The groups that included PVA fibres were designed to investigate the properties of ITZ, while the remaining groups served as fibre-free reference groups. The CEM III/B 42.5 N cement, sourced from ENCI in the Netherlands), is composed of 20-34% clinker and 66-80% blast furnace slag (BFS). The filler was Calcitec® limestone powder from Carmeuse (Belgium) with a particle size distribution comparable to that of the cement. To achieve the required workability, the superplasticiser MasterGlenium 51, based on polycarboxylate and produced by BASF (Germany) was used, containing 35.0% solid content by mass. The microfibre used to create the ITZ is a PVA (Polyvinyl alcohol) microfibre from Kuraray (Japan) with a 1.2% by-weight oiling coating. This coating forms a hydrophobic barrier between the cement-based matrix and the hydrophilic surface of PVA, without influencing the microstructure of ITZ [48]. The nominal diameter of the fibre is 39 μm, as specified by the manufacturer. The mechanical and physical properties of the PVA fibre are presented in Table 2.

Table 1 Material and experimental mix proportions

Group	Binder type	W/c ratio	Filler-to-binder ratio
1	CEM I	0.3	-
2	CEM I	0.4	-
3	CEM I	0.5	-
4	CEM III/B	0.3	-
5	CEM III/B	0.4	-
6	CEM III/B	0.5	-
7	CEM III/B + limestone	0.3	0.5
8	CEM III/B + limestone	0.4	0.5
9	CEM III/B + limestone	0.5	0.5

Table 2 Mechanical and physical properties of PVA fibres

Diameter (μm)	Density (kg/m^3)	Nominal tensile strength (MPa)	Young's modulus (GPa)	Surface oil content (wt.%)
39	1300	1640	41.1	1.2

3.2.2 Sample Preparation

At first, a prismatic mould was fitted with five 150 mm long PVA fibres spaced equally apart. The fresh mixtures were poured into the mould after 1 minute of mixing at low speed and two minutes of mixing at high speed. After releasing trapped air with a 2-minute vibration on a vibration table, the mould was covered with a plastic lid at room temperature for 24h. After demoulding, the cement paste prism was cured in a climate room (20°C and ≥ 98% RH) for 28 days. The hydration of specimens was interrupted with isopropanol at the end of curing.

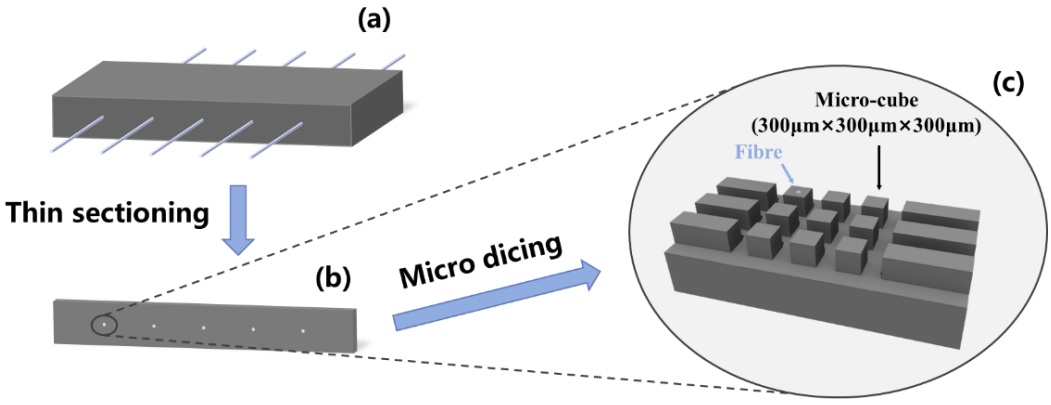

Fig. 3.1 Schematic illustration of micro-cube production: (a) prismatic cement paste specimen embedded with five longitudinally distributed fibres. (b) sliced specimen after thin sectioning. (c) 3×3 microcubes array after micro dicing.

Afterwards, the cement paste prism embedded with fibres was sliced through thin sectioning by a diamond saw (see Fig. 3.1.a to Fig. 3.1.b). The thickness of the slices is roughly 2 mm. Two types of specimens, with fibre and reference without fibre, were prepared to compare the influence of the ITZ. Since the polymeric fibre is transparent, it could be easily located by the optical microscope under transmitted light mode, shown as the bright dot in Fig. 3.2a. MicroAce Seried 3 Dicing Saw was used to fabricate the microcubes from the slices. To ensure that the fibres were in the centre of the specimen, the central axis of the blade was shifted upwards by 570 μm with the fibres in the centre during cutting, schematically shown in Fig. 3.2b. Since only five fibre cubes could be fabricated on each slice, after setting up two mutually perpendicular directions, a 3 by 3 microcube matrix was produced, consisting of one cube with fibre in the upper left corner and the remaining eight cubes without, as shown in Fig. 3.1c. Fig. 3.2c represents the untested microcubes as observed under an optical microscope. In this study, the number of samples with fibre or without fibre for each w/c ratio was 10.

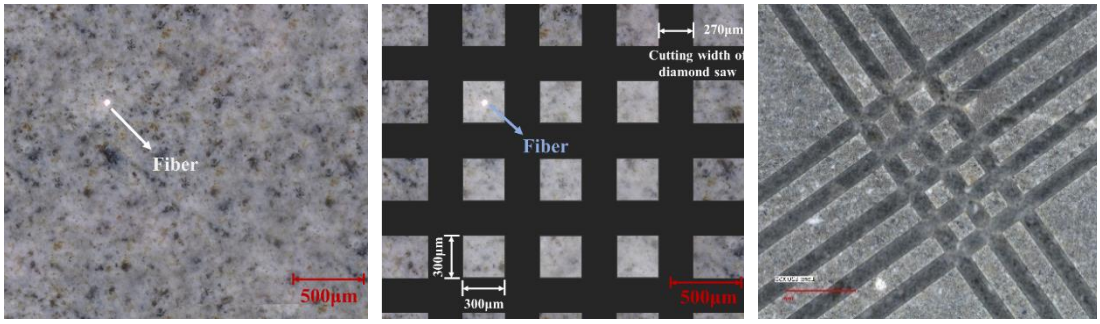

(a) (b) (c)

Fig. 3.2 Sliced surface under the optical digital microscope: (a) the position of the fibre is located by the transmitted light mode. (b) schematic diagram of micro dicing saw cutting microcubes. (c) untested microcubes as observed under an optical microscope.

3.2.3 Test

An Agilent G200 Nano Indenter equipped with a diamond wedge tip was used to conduct the microcube splitting test. The length and radius of the cylindrical edge are 200 μm and 9.6 μm, respectively. As shown in Fig. 3.3, a line load is applied at the centre of the top surface, with a constant displacement increment of 50 nm/s until the cube fails. The specific geometric structure of the diamond wedge tip is illustrated in Fig. 3.4.

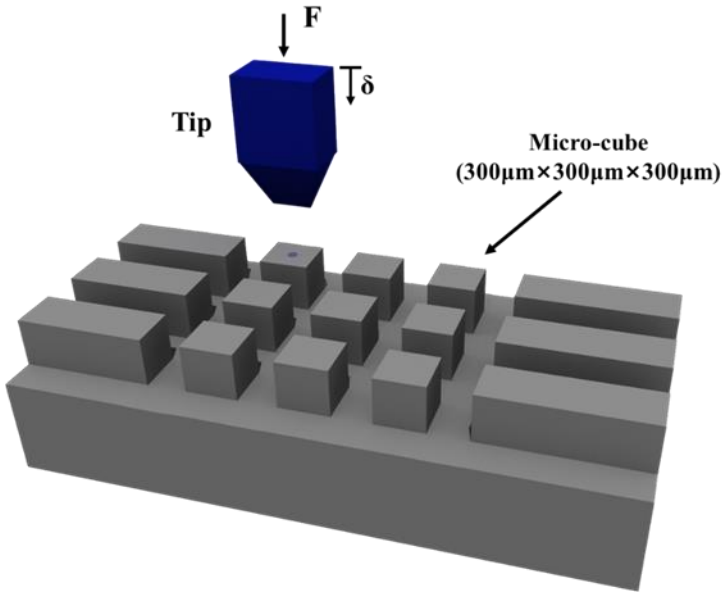

Fig. 3.3 Schematic illustration of micro-splitting test.

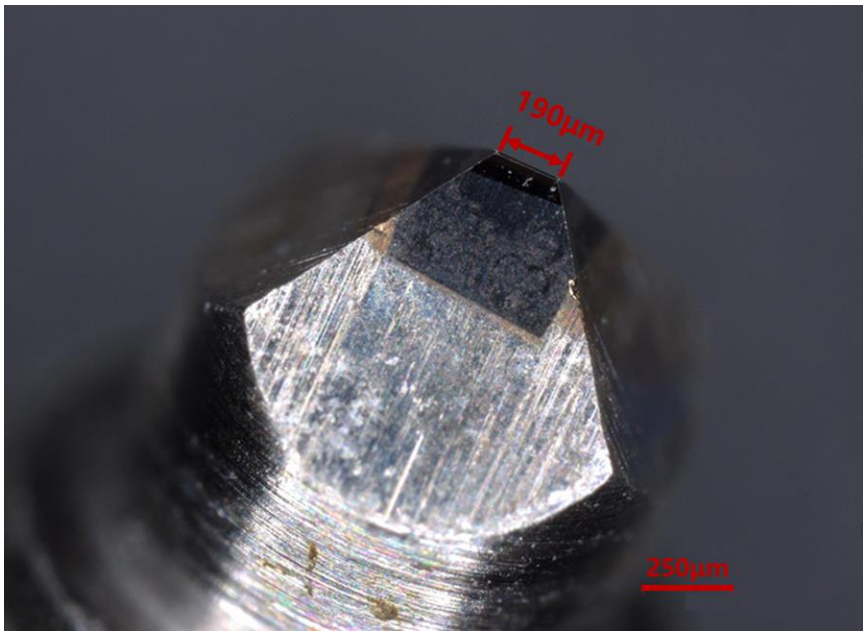

Fig. 3.4 Diamond wedge tip under optical microscope.

The nanoindentation tests were performed by applying the continuous stiffness measurement (CSM), which is insensitive to thermal drift and records the small-volume deformation accurately [75]. The harmonic frequency, displacement, and surface detection of CSM oscillation are 45 Hz, 2 nm, and 100 N/m respectively. An optical digital microscope (Keyence VHX-7000) was applied to locate the fibre position under transmitted light mode. The secondary electron detector in a field emission scanning electron microscope (FEI QUANTA FEG 650) was employed to inspect the specimens after testing. A generated microbeam is scanned using a Micro CT scanner (CoreTOM) to analyse the porosity in the cement paste. The

microbeam was fixed on the holder and located on the rotatable stage. The X-ray source tube worked at 70 Kev/200mA. 900 images with an exposure of 6 s were acquired on a digital GE DXR detector. The voxel resolution under these conditions was 5.64 μm^3. The 3D visualisation was conducted using Dragonfly software.

3.3 Result and Discussion

3.3.1 Microstructural Characterisation

Compared to conventional nano-indentation tests with Berkovich indenters, results obtained from the indentation splitting test are more representative of the global mechanical performance of micro-cubes, for that the crack typically propagates through the ITZ due to its porous nature. Given that the thickness of PVA fibre-matrix ITZ generally ranges from 100-150 μm [7], the micro-cubes were designed with a dimension of 300 μm. The produced micro-cube arrays were observed by an environmental scanning electron microscope (ESEM), revealing that each micro-cube was flawlessly fabricated, as shown in Fig. 3.5. Every array has nine specimens overall, arranged in a 3×3 configuration. In each micro-cube array, only the top-left specimen contains fibre, while the remaining 8 specimens are without fibres. To prevent interference with adjacent specimens during the splitting tensile test, where a specimen may split into left and right halves at the wedge tip, testing is limited to only the top-left and bottom-right corners (one specimen with fibre and one without) within each array.

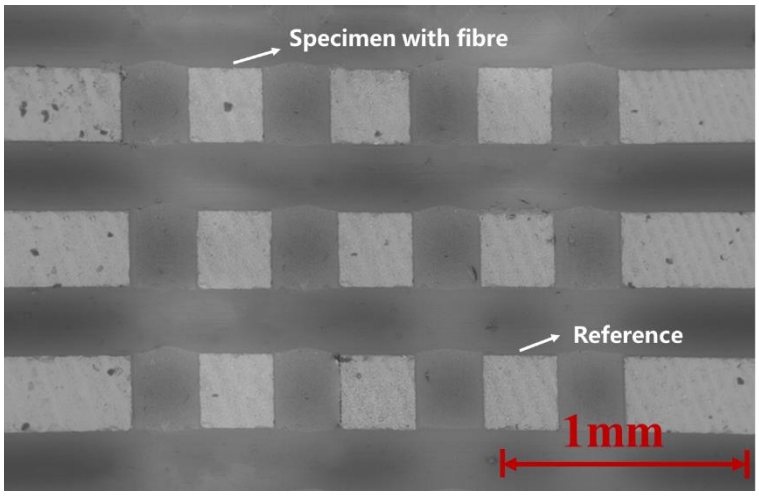

Fig. 3.5 SE image of microcubes: One specimen with fibres is located in the upper left corner and the rest are without fibres.

Fig. 3.6 shows the SE image of the failed specimens with and without fibre. Since the maximum tensile stress is always present in the central axis below the tip, it is clear that the specimen

without fibres is divided into left and right sections. Except for the cement paste, the fibre was also splitting into two halves by the indenter tip. For the specimen with fibres, there is a noticeable secondary crack on the right side in addition to the primary crack in the middle

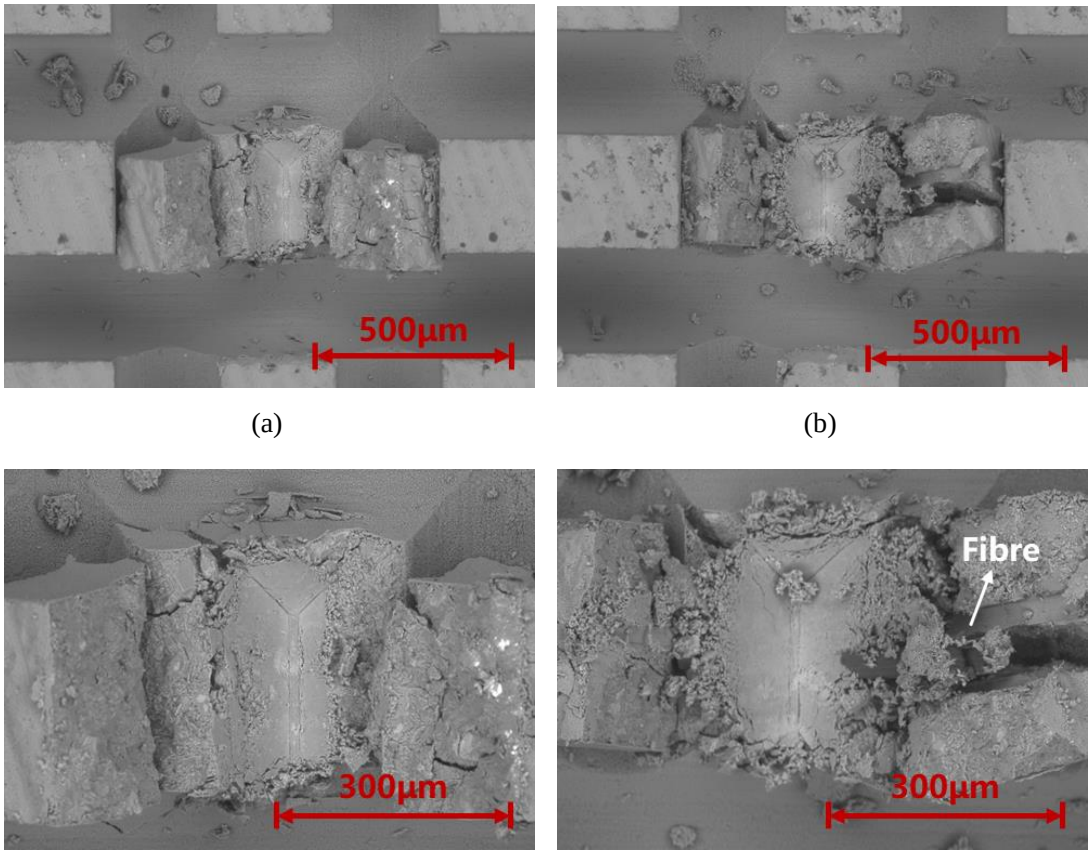

Fig. 3.6 SE image of failed specimen: (a)Reference, (b)Fibre, (c) Magnified reference, (d) Magnified fibre.

Fig. 3.7a presents a 3D scan of a specimen with fibre by the X-ray computed tomography technique (XCT). The four phases of anhydrous cement, inner hydration products, outer hydration products, and capillary pores could be easily identified based on the variation in grey value. The porosity of the specimen is visualized in Fig. 3.7b. Following thresholding in accordance with the grey value, the volume of fibres is also included in the pore visualization due to the average atomic numbers of fibres and pores are similar. The specimen has a single, clearly visible fibre in the centre, and the pore size and porosity decrease as the distance from the fibre surface increases, which aligns with the finding in [7]. The ITZ has a larger porosity than cement paste, and owing to its irregular pore distribution, it is susceptible to stress concentration at specific high porosity regions.

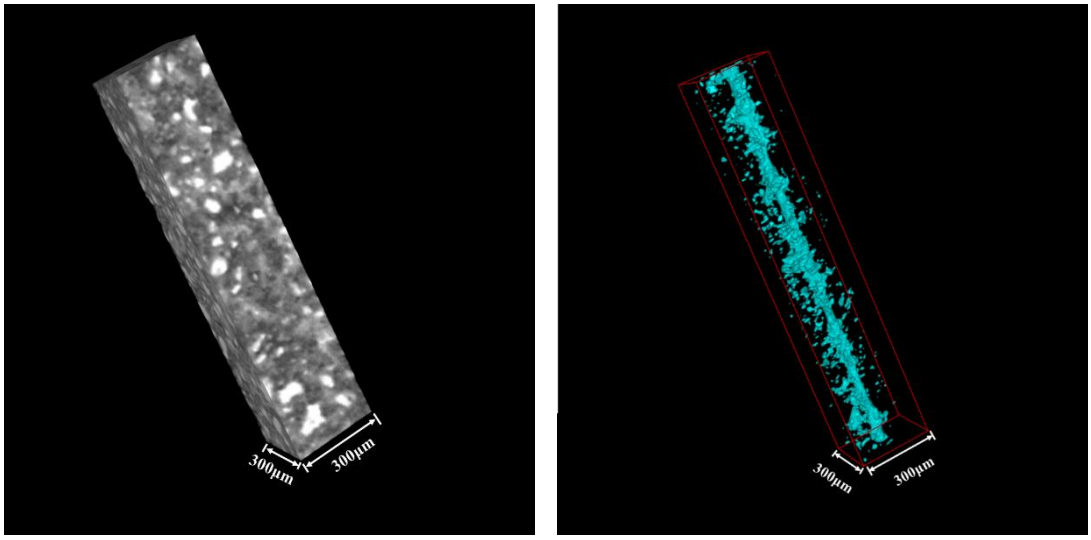

(a) (b)

Fig. 3.7 Schematic view of XCT experiment: (a)Greyscale image composed of four phases: anhydrous cement, inner hydration products, outer hydration products, and capillary pore. (b)Visualization of pores in specimens

3.3.2 Mechanical Properties of Micro-cubes

A typical load-displacement curve generated by the nanoindentation test is shown in Fig. 3.8. This graph clearly shows two regimes and the maximum load point at the failure stage. The load on the sample increases monotonically in regime (I) until it reaches the critical splitting load (maximum load). The system shifts from a stable regime (I) to an unstable regime (II) once the load exceeds the maximum load. The wedge indenter tip had an overshoot due to the structural collapse of the micro-cube, as indicated by the horizontal line. Currently, it is not feasible to capture the post-peak behaviour of the specimen since the displacement control of the nano-indenter is insufficiently rapid. Moreover, the system is unable to detect a snap-back and the behaviour may be brittle. It should be noted that the observed displacement includes the local imprinting of the indenter on the micro-cube. Consequently, the stiffness or modulus of the tested micro-cubes cannot be directly determined from the recorded load-displacement curves. It should be noted that the original load of the specimens with fibres starts to increase significantly after the displacement reaches 7 μm, as shown in Fig. 3.8. This may be because the indenter initially made contact with the fibre before the wedge completely engaged with the top surface of the microcube. The lower modulus of PVA fibres leads to a reduction in composite stiffness, thereby slowing down the development of cracks. Therefore, this portion of the curve with a smaller slope was manually removed in the subsequent calculations to avoid its impact on the calculations of displacement, stiffness, and fracture energy of the specimen.

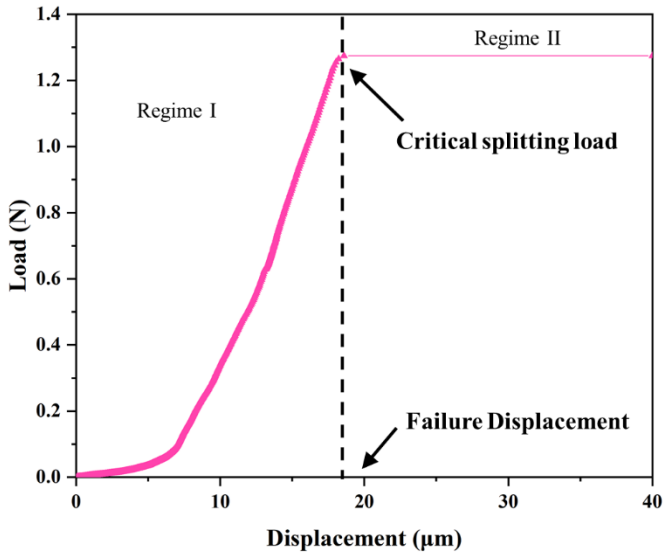

Fig. 3.8 Load-displacement curve generated by nanoindentation test.

Representative load-displacement curves of specimens with and without fibre are shown in Fig. 3.9 (CEM I, w/c ratio of 0.4). As previously stated, the overshoot behaviour of the indenter is represented by the horizontal line in regime II. The figure shows that the reference specimen has a peak force between 1.5 and 2.5 MPa, which is higher than the fibre specimen (between 0.75 and 1.5 MPa). In addition, the displacement of fibre specimens is higher than that of the reference group, suggesting that the presence of fibres reduces the stiffness of the microprism.

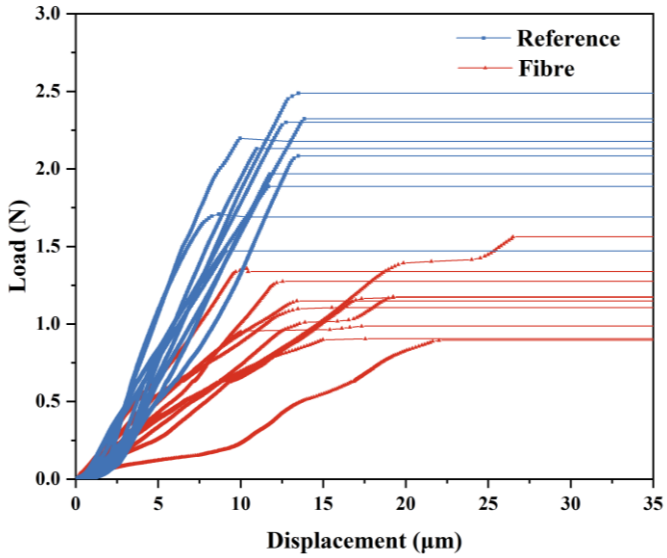

Fig. 3.9 Load-displacement response of CEM I reference and fibre specimens under a w/c ratio of 0.4

The indentation splitting results of microcubes for each w/c ratio are summarized in Fig. 3.10-13. The median is indicated by the central black line in each box, while the 25th and 75th

percentiles are indicated by the top and bottom margins of the box, respectively. Dashed lines connect the mean values at each w/c ratio. The whiskers extend to the most extreme data points excluding the outliers. Values that deviate from the bottom or top of the box by more than 1.5 times the interquartile range are regarded as outliers. Fig. 3.10 presents the changes of peak load for the microcubes. As can be seen, for all kinds of material and at all w/c ratios, peak loads of specimens with fibres are significantly lower than those without fibres, suggesting that the presence of fibre and its accompanying ITZ may have significantly altered the microstructure of the microcube. Furthermore, although the peak loads of all types of microcubes show decreasing trends with increasing w/c ratio, CEM I microcubes with fibre exhibited a more substantial decrease in load capacity (42% reduction). In contrast, for CEM III and CEM III+L microcubes the reduction in load capacity was more significant in the reference specimens than in the fibre specimens.

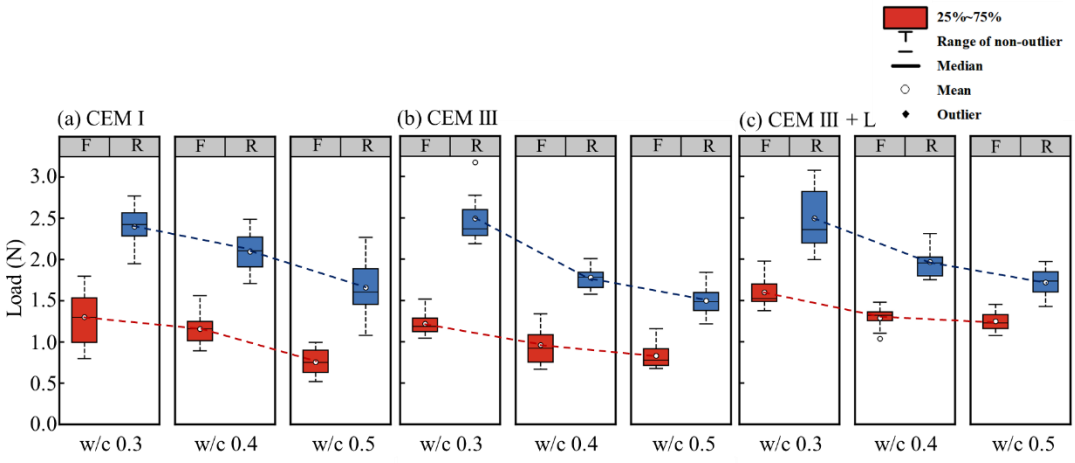

Fig. 3.10 Box plots for the peak load of (a) CEM I, (b) CEM III, and (c) CEM III + L

Fig. 3.11 illustrates the deformation of microcubes at failure during the indentation splitting test. Microcubes containing fibre inclusions experienced significantly greater deformation across all w/c ratios compared to the reference specimens of CEM I. However, for CEM III and CEM III+L, the difference between fibre and reference specimens was less pronounced. Additionally, the deformation behaviour of the microcubes reinforced with fibre showed a dependence on w/c ratios. Except for CEM III with a w/c ratio of 0.4, the deformation of specimens with fibre increased for the other two materials. In contrast, the deformability of the reference microcubes was only slightly affected by changes in w/c ratios. Previous studies have demonstrated that ITZ has a higher porosity than cement paste, and this porosity difference progressively decreases with increasing fibre distance [7]. The porosity of ITZ varies because of variations in the local w/c ratio close to the fibre and the overall w/c ratio. The ductility and failure displacement of the specimens both rose as their porosity increased. Whereas, as the w/c

ratio increased, the highly brittle cement paste characteristics did not alter significantly for the specimens without fibre.

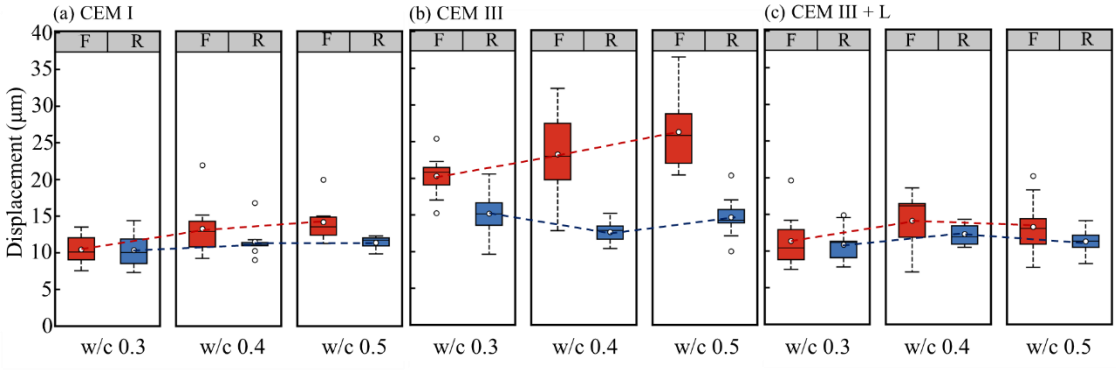

Fig. 3.11 Box plots for the displacement at the failure of (a) CEM I, (b) CEM III, and (c) CEM III + L

Fig. 3.12 presents the stiffness of regime I for fibre and reference microcubes under various w/c ratios. To avoid noise and anomalies in the calculation of stiffness, the data was first normalized by retaining the middle 80% of the load-displacement curve. Linear regression was then applied to this segment to determine stiffness, which is represented by the slope of the linear fit. It can be seen from the figure that the stiffness of all the specimens shows a decreasing trend as the w/c ratio increases.

Due to the high peak load and low failure displacement characteristics of the reference specimens, the stiffness of the reference specimens is higher than that of the fibre specimens across all groups. However, it is evident that the difference between the specimens with and without fibre is much more pronounced in CEM I compared to CEM III and CEM III + L. For the reference specimens of CEM I, this effect is not significant when the w/c ratio increases from 0.3 to 0.4. For CEM III and CEM III + L, there is no significant change in the stiffness of either fibre or reference specimens when the w/c ratio increases from 0.4 to 0.5. It is difficult to have a significant impact on the stiffness of the specimens since the peak load of the CEM III and CEM III+L experimental group does not change significantly with an increase in the w/c ratio from 0.4 to 0.5, and the displacement at failure is also less affected by the w/c ratio. For the CEM I specimens with fibre, its peak load decreased, and failure displacement increased simultaneously with the increase of the w/c ratio, leading to a more pronounced decreasing trend in the stiffness when those changes were superimposed.

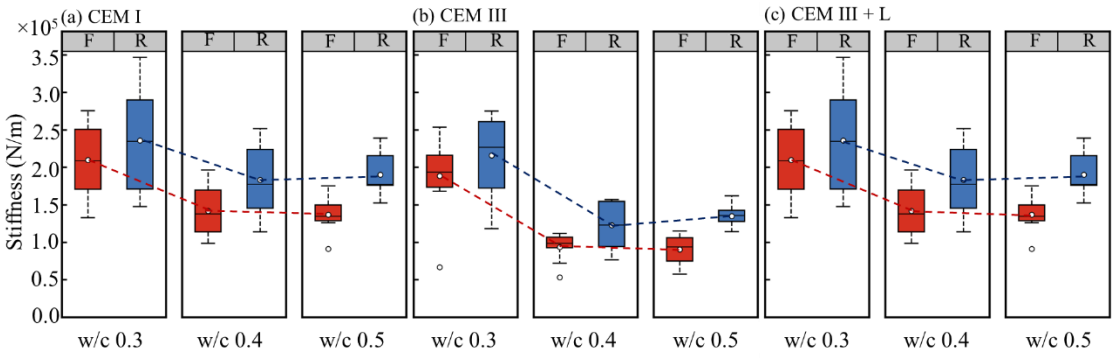

Fig. 3.12 Box plots for the stiffness of (a) CEM I, (b) CEM III, and (c) CEM III + L

The resistance to fracture is another essential property of the fibre-reinforced concrete. The measure of fracture resistance is given by the specific work of fracture, which is calculated by the area integrals under the load-displacement curves in this paper. Widespread microscopic damage occurs throughout the body when the specimen is loaded. Significant damage can be sustained up to a point when the propagation of cracks causes failure. The microcubes failed due to a complicated combination of cracks propagating along the interfaces and fractures of the matrix and load-bearing fibres. Therefore, the fracture toughness of the microcubes depends not only on the properties of the constituents but significantly on the efficiency of bonding across the interface [76].

Fig. 3.13 presents the fracture energy of fibre and reference microcubes under various w/c ratios. The fracture energy was calculated by integrating the area under the load-displacement curve and dividing it by the paste cross-section (excluding the fibre area). The trend for CEM I is similar to that of CEM III: for the specimens with fibres, the magnitude of peak load reduction and increase in failure displacement is similar for w/c ratios of 0.3 and 0.4, so there is no apparent shift in fracture energy; however, when the w/c ratio is further increased, the fracture energy shows a significant decrease. The specimens without fibres had the same pattern that was determined in [77, 78], where fracture energy and brittleness decrease as the w/c ratio increases.

Owing to the presence of a large amount of microcracks in ITZ, the w/c ratio is very significant in determining the fracture energy of concrete. As the w/c ratio increases, the porosity between the paste and the ITZ increases, making the paste weaker [79]. However, for CEM III + L specimens, regardless of the presence of fibres, the fracture energy does not show a significant trend with changes in the w/c ratio.

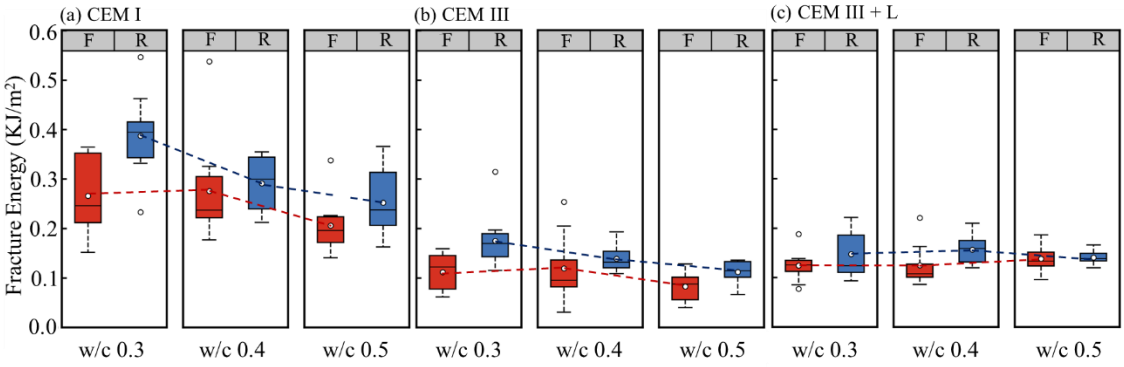

Fig. 3.13 Box plots for the fracture energy of (a) CEM I, (b) CEM III, and (c) CEM III + L

Fig. 3.14-Fig. 3.17 summarizes the indentation splitting results of microcubes for each w/c ratio. The red box plots represent the results for specimens containing fibre, while the blue box plots show the experimental results for reference specimens. The trends in material behaviour with varying w/c ratios have been presented in Fig. 3.10-13 and will not be reiterated here; instead, the focus is on the differences between the materials. As can be seen, regardless of the microcubes with fibres, the peak load of CEM III+L is higher than that of the other two groups, with CEM I being slightly higher than CEM III. However, in terms of failure displacement, the CEM I specimens with fibre exhibit much higher values than the other two groups, while there is no significant difference among the reference specimens of the three materials. Therefore, considering the similar peak loads and much higher failure displacement, the stiffness of CEM I fibre specimens is much lower than that of the other two materials, as shown in Fig. 3.15a. Finally, the fracture energy of CEM I is higher for both fibre and reference specimens compared to the other two materials.

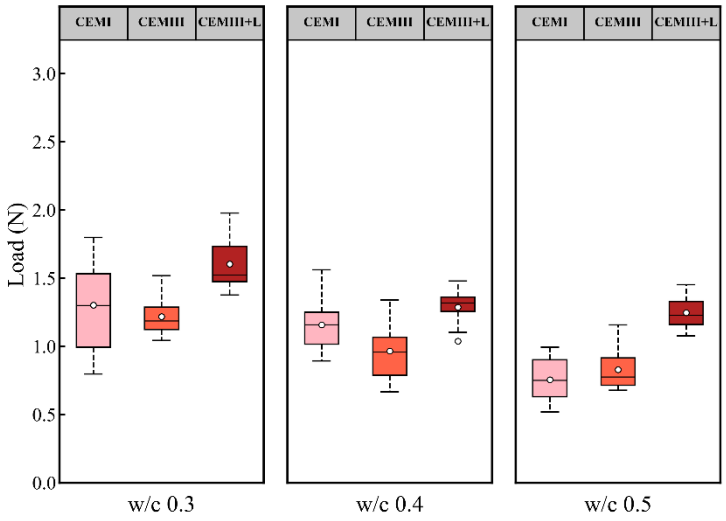

(a)

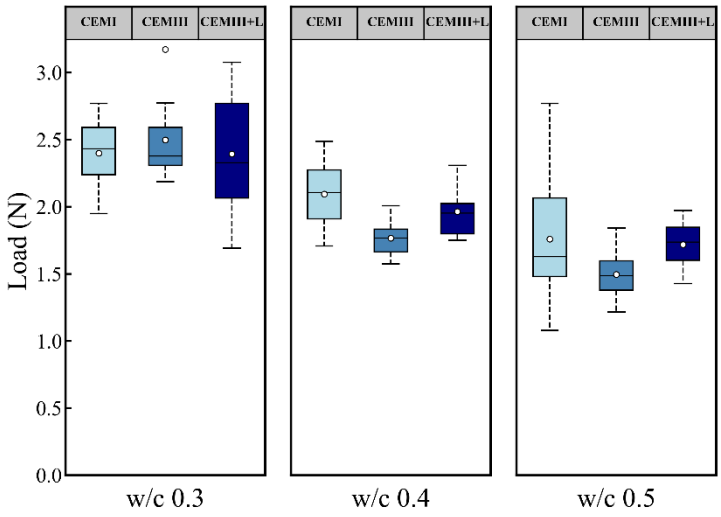

(b)

Fig. 3.14 Box plots for the peak load of different materials at various w/c ratios: (a) Fibre specimens; (b) Reference specimens.

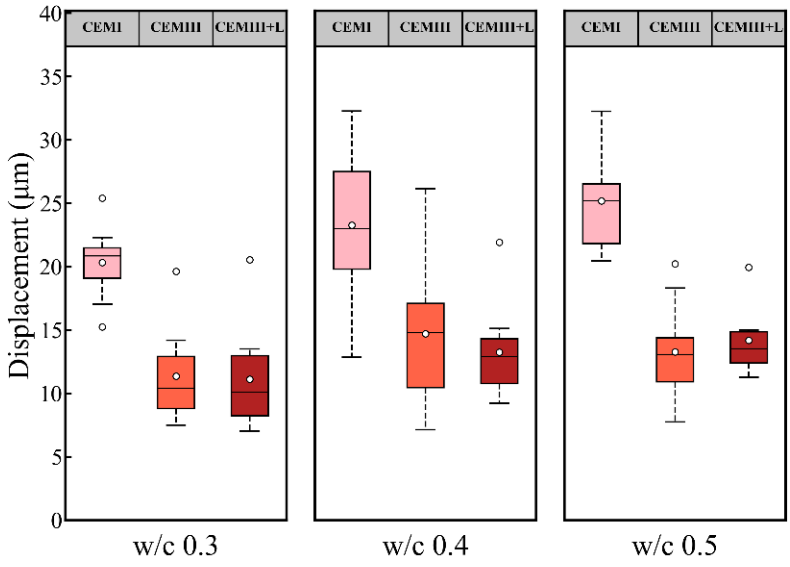

(a)

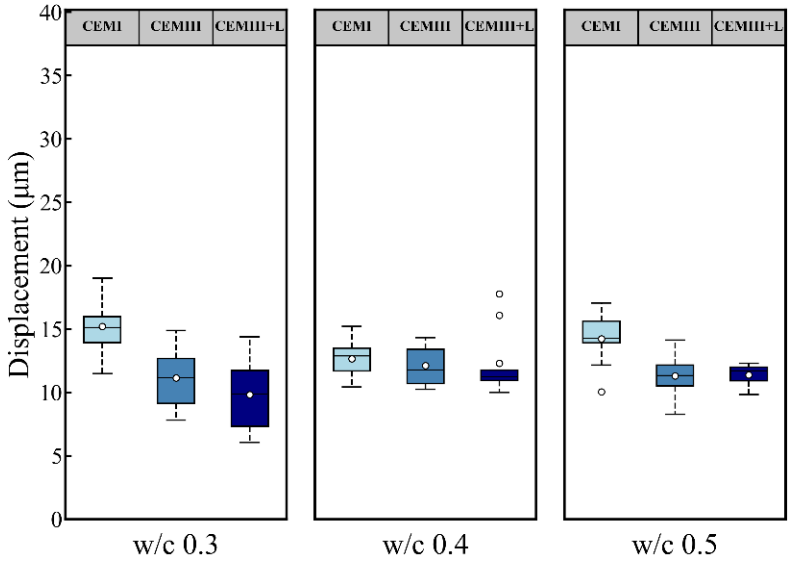

(b)

Fig. 3.15 Box plots for the failure displacement of different materials at various w/c ratios: (a) Fibre specimens; (b) Reference specimens.

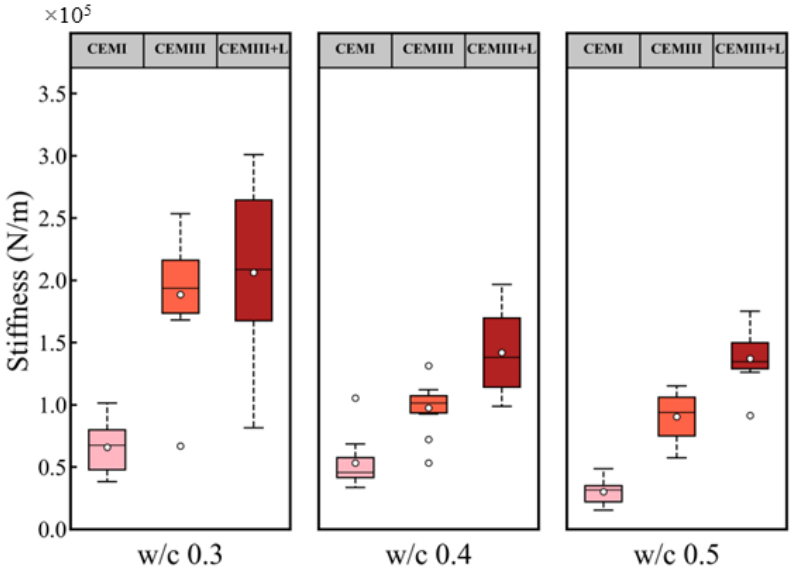

(a)

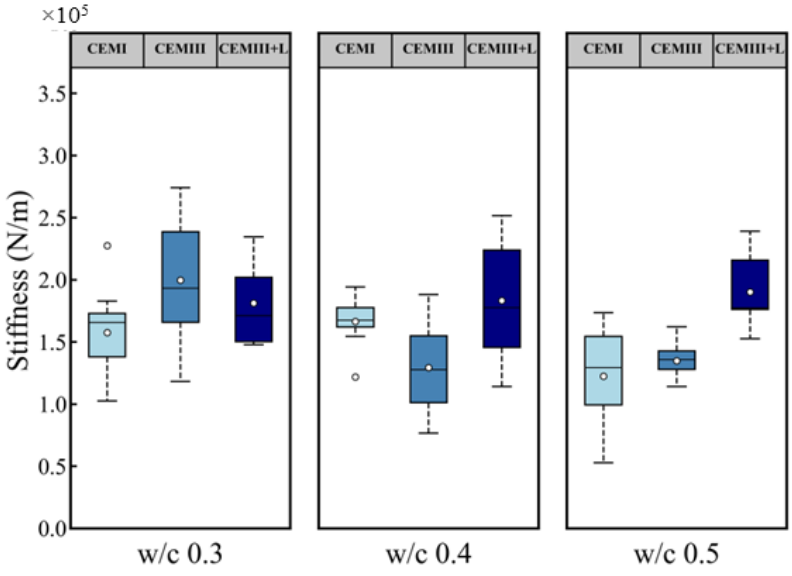

(b)

Fig. 3.16 Box plots for the stiffness of different materials at various w/c ratios: (a) Fibre specimens; (b) Reference specimens.

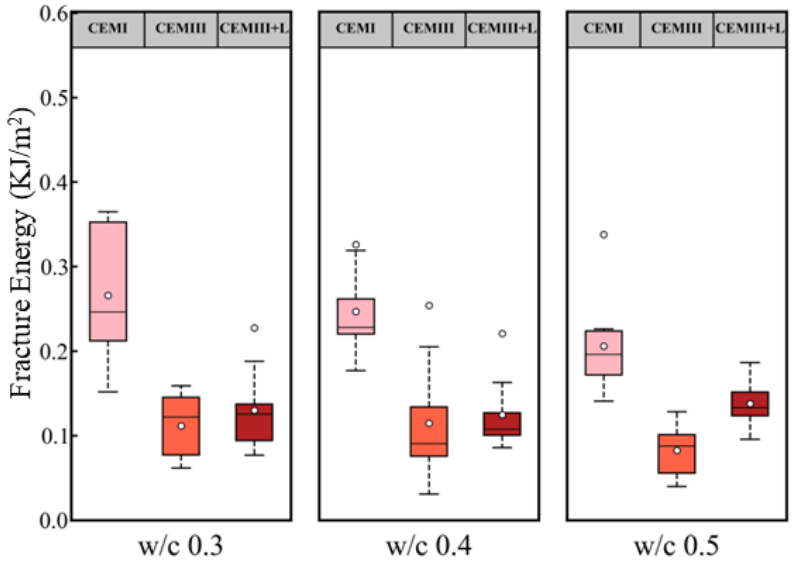

(a)

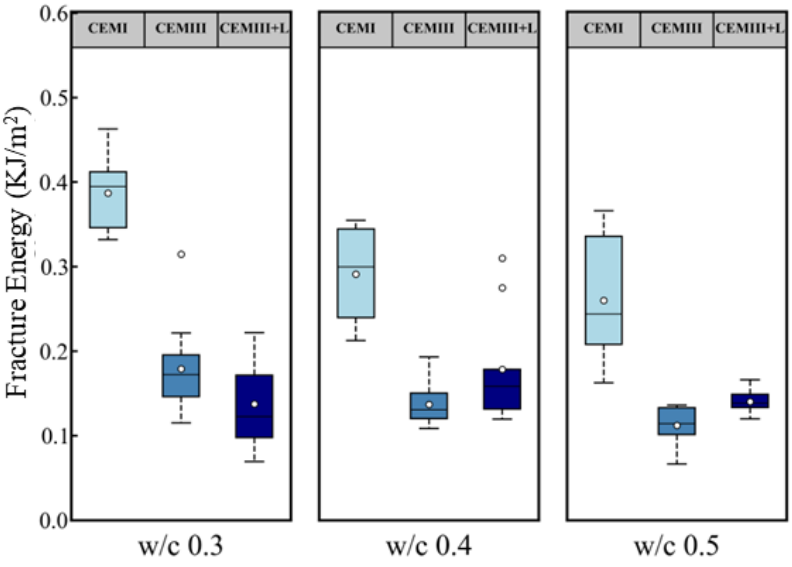

(b)

Fig. 3.17 Box plots for the fracture energy of different materials at various w/c ratios: (a) Fibre specimens; (b) Reference specimens.

In previous research [51], an analogy between the micro-cube splitting test and the standard Brazilian splitting test (NEN-EN 12390-6 Standard) was made to predict the tensile strength using finite element modelling (FEM). A reduction factor α is added to characterise the boundary condition variation based on the Brazilian splitting test. The splitting tensile strength could be calculated by Eq. 1. It should be noted that while the process of determining the nominal splitting strength considers the material as if it were an ideal isotropic elastic material,

the objective of this approach is to define a proper parameter that can be used to represent the global mechanical properties of the material according to the test. This allows for the quantification and comparison of the effects of variations in the microstructure on the yield strength at this scale.

$$f_{st} = \alpha \frac{2P_u}{\pi D^2} \quad \text{Eq. 1}$$

where P is the maximum load, the length of the cube, and the reduction factor α = 0.73. It is worth noting that the change in the length of the loading head can affect the stress distribution and stress concentration effects, thereby influencing the test results. In this case, the length of the indenter tip is shorter than the length of the specimen. Therefore, the standard reduction factor α=0.73 may not be applicable to this specific situation and requires further calibration in subsequent experiments. In specimens containing fibres, the effective calculated cross-sectional area is obtained by subtracting the transverse cross-sectional area of the fibres from the cube cross-sectional area (300 μm×39 μm =78300 μm^2).

Fig. 3.18 displays the splitting tensile strength results for the reference and fibre microcubes for CEM I, CEM III and CEM III+L under various w/c ratios. The calculation process specifically accounts for the effective area of the cementitious matrix, excluding the influence of the fibres themselves. As expected, an increase in the w/c ratio results in a decrease in the splitting tensile strength for both fibre and reference experimental groups. Moreover, at each w/c ratio, the strength of specimens with fibres is significantly lower than that of specimens without fibres. Consequently, it is reasonable to infer that the observed reduction in splitting tensile strength is directly attributable to the presence of the ITZ. For the reference group, the splitting tensile strength of CEM I is higher than that of the other two materials, while CEM III shows a steeper decline. For the fibre group, the splitting tensile strength of CEM III+L is higher than that of the other two materials. Without fibres, CEM I exhibits a higher degree of hydration compared to the other two materials, resulting in a denser hydration product and therefore higher splitting tensile strength. Previous study shows that an appropriate amount of LP incorporation optimizes the packing, leading to a narrower space and more densely compacted C–S–H that improves the percentages of high-density C–S–H and ultra-high-density C–S–H in ITZ [80]. With the addition of fibres, the extra limestone in CEM III+L acts as a filler in the ITZ, making the hydration product structure in the ITZ denser, thereby enhancing its splitting tensile strength. Additionally, Fig. 3.19 shows a tendency for the difference between the groups with and without fibre to increase as the w/c ratio increases. The significance of increasing w/c ratio on the influence of ITZ is discussed in section 3.3.

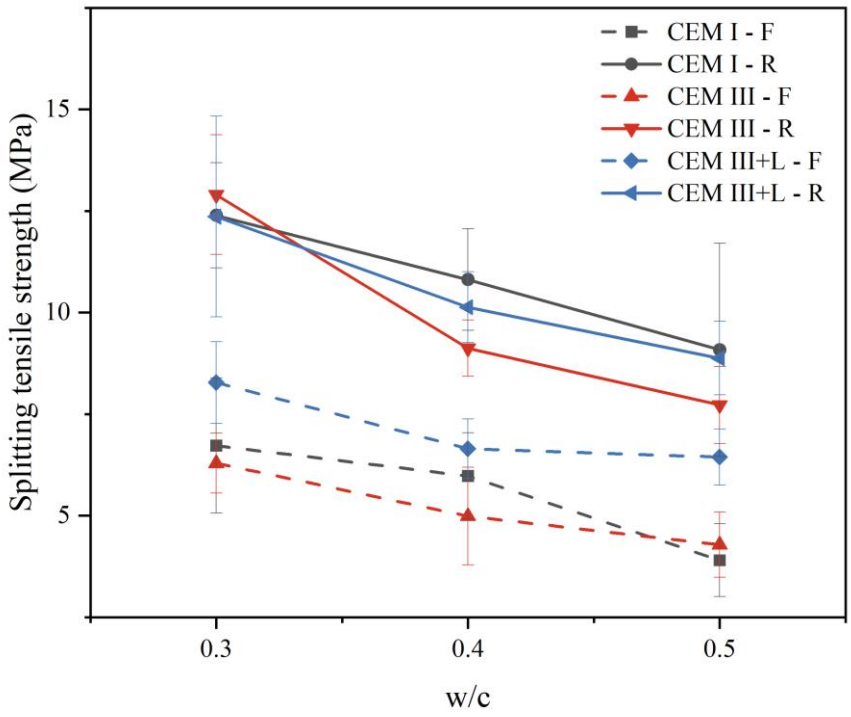

Fig. 3.18 Splitting tensile strength of microcubes

3.3.3 Influence of Fibre Inclusion

In this section, the effect of introducing fibres on the mechanical properties of microcubes at various w/c ratios is discussed. The nominal differences in load, displacement, stiffness, and fracture energy are listed in Table 3, and the variations trend are presented in Fig. 3.19. These trends represent the actual differences divided by the values of reference specimens. Note that the difference here is calculated by the average value of each mechanical property.

Table 3 Differences in various mechanical properties between different materials

Material type	w/c ratio	Load difference (%)	Displacement difference (%)	Stiffness difference (%)	Fracture energy difference (%)
CEM I	0.3	45.7	33.8	60.3	31.4
	0.4	44.7	83.8	67.9	5.2
	0.5	57.0	77.9	75.3	20.8
CEM III	0.3	51.2	1.9	18.9	37.6
	0.4	45.3	21.3	24.7	16.3
	0.5	44.5	17.5	33.0	26.2
CEM III + L	0.3	33.0	13.0	4.9	5.4
	0.4	54.3	5.6	27.8	25.3
	0.5	27.4	24.6	28.0	1.7

In Fig. 3.19a, there is no significant variation in the peak load difference between w/c ratios of 0.3 and 0.4 for CEM I. However, the difference exceeds 55% as the w/c ratio further increases to 0.5. For CEM III, the effect of fibre inclusion slightly decreases with increasing w/c ratio, but the variation is not significant. When limestone powder is added (CEM III + L), the load difference initially increases and then decreases with the increasing w/c ratio.

Regarding the difference in failure displacement as shown in Fig. 3.19b, the inclusion of fibres has a significantly higher impact on CEM I compared to the other two materials. The displacement difference for CEM I increases from 33.8% at a w/c ratio of 0.3 to 83.8% at a w/c ratio of 0.4, and it remains consistent at 77.9% at a w/c ratio of 0.5. At lower w/c ratios, the introduction of fibres has a more pronounced impact on the displacement at failure, whereas at higher w/c ratios, its influence is more noticeable on the peak load. For CEM III and CEM III + L, the displacement difference does not follow a specific trend with varying w/c ratios and is less significant compared to CEM I.

In Fig. 3.19c, a noticeable upward trend in the difference of stiffness with increasing w/c ratio for all materials. Similar to the displacement difference, the impact of fibre inclusion on CEM I is far greater than on the other two materials, surpassing 75% at a w/c ratio of 0.5. This indicates that the influence of fibre introduction on the stiffness of specimens becomes more significant as the w/c ratio increases. The interfacial stiffness influences the maximum force, shear stress and toughness of the composite during the pullout test, which is the crucial parameter that governs the effective efficiency of fibre bridging [81, 82].

Due to the uneven effects of increasing the w/c ratio on the reduction of peak load and the increase in failure displacement caused by the presence of the ITZ, there is no significant trend in the fracture energy difference for all materials. It is proven that the introduction of fibres has a significant negative effect on the stiffness of ITZ, however, the variation of stiffness does not directly correspond with the fracture energy. While lowering the w/c ratio improves the overall performance of FRC, it may not be an effective strategy for enhancing interface performance locally.

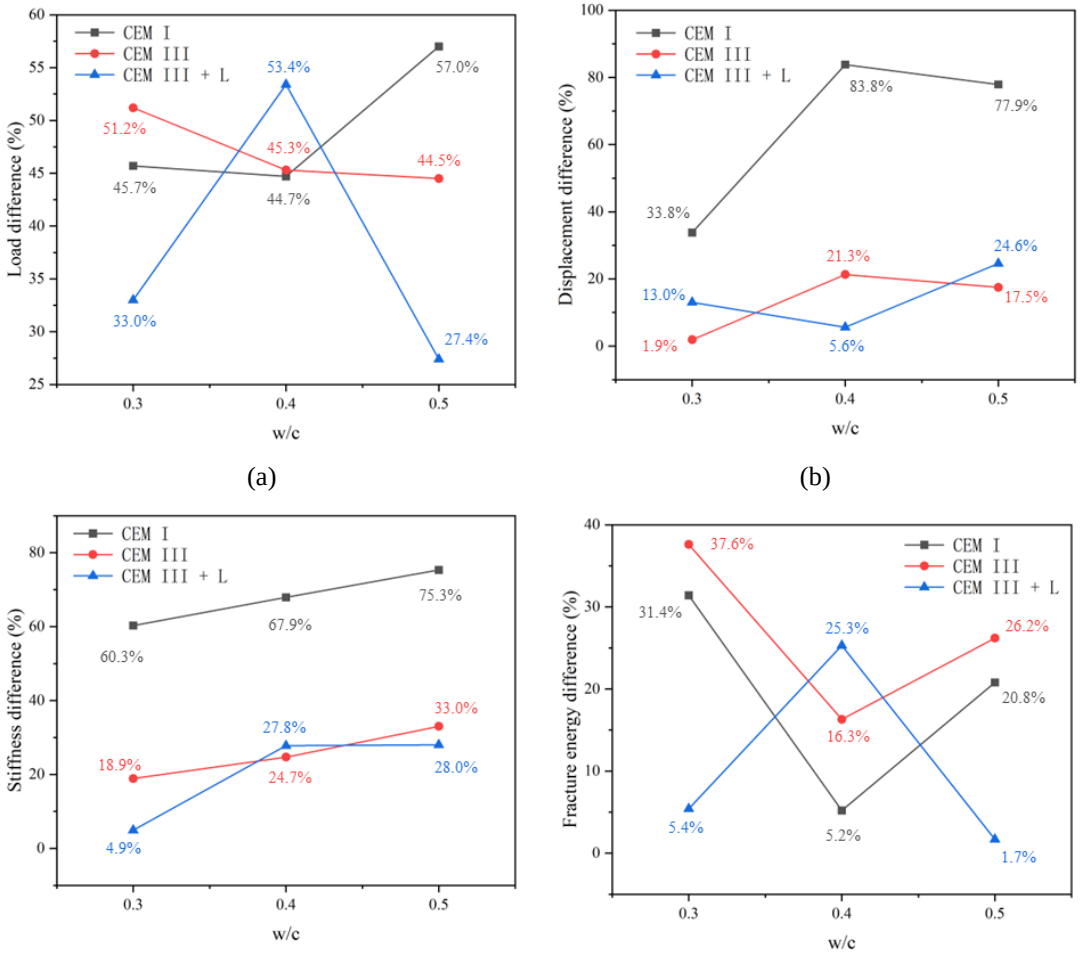

Fig. 3.19 The effect of fibre inclusion on mechanical properties between different materials: (a) Load difference; (b) Displacement difference; (c) Stiffness difference; (d) Fracture energy difference.

3.4 Conclusions

In this Chapter, a framework for fabricating microcubes embedded with single microfibre and testing the fibre-matrix interfacial transition zone (ITZ) was developed, enabling an investigation into the tensile properties of ITZ. The splitting tensile behaviour was tested by a nanoindenter equipped with a wedge tip. The impact of introducing fibres on the mechanical properties of microcubes across different w/c ratios was discussed. The results show that the newly proposed method for fabricating microcubes ensured the integrity of the specimens and the indentation splitting test can serve as an effective evaluation of the tensile behaviour of the fibre-matrix interface. The following conclusion can be drawn:

1. For all kinds of material and at all w/c ratios, the peak load, stiffness and fracture energy of specimens with fibres are significantly lower than those without fibres, suggesting that the presence of fibre may have significantly altered the microstructure of its surrounding cement-based matrix.
2. With the increase in the w/c ratio, all groups show a decreasing trend in peak load and stiffness. The failure displacement does not exhibit a significant change with varying w/c ratios. The fracture energy of CEM I and CEM III decreases with the increase in the w/c ratio, while CEM III+L does not show a clear correlation.
3. The addition of limestone powder (CEM III+L) improves the fracture energy and tensile strength of the micro-cubes with fibre, which can be attributed to the filler effect of limestone. Due to its small particle size, the limestone powder can potentially densify the microstructure of the ITZ. This effect is stronger at higher w/c ratios, demonstrating the importance of optimizing the ITZ for improved mechanical performance.

4

Modelling of Micro-cubes on Indentation-splitting Behaviour

In Chapter 4, the simulation of the indentation splitting tensile test was applied to investigate the individual mechanical behaviour and fracture propagation within the microcube material properties of the ITZ.

4.1 Introduction

In Chapter 3, the tensile property of the microcubes was characterised by the indentation splitting test. In this Chapter, a lattice model was applied to assess the mechanical properties of ITZ and simulate the fracture behaviour of the tested CEM I micro-cubes. The model represents the material as a grid of beam elements that are joined at the ends. Each individual element is assumed to have linear elastic behaviour. To be able to account for shear deformation, a Timoshenko beam element is employed in the network, as the ratio of length to height of the beam elements is low [83]. Subsequently, a series of linear elastic studies are conducted by determining the stress distribution at each element under a prescribed external boundary condition. The relationship between normal force and bending moments in lattice beam elements is expressed by the following generic equation:

$$\sigma=\alpha_N \frac{N}{A}+\alpha_M \frac{\max(M_x,M_y)}{W} \qquad \text{Eq. 2}$$

where A represents the area of the beam cross-section, W represents the cross-sectional moment of resistance, and N represents the normal force along the element. M_x and M_y are the bending movements in the local coordinate system. α_N and α_M represent the normal force influence factor and the bending influence factor. Their values are commonly adopted as 1.0 and 0.05 [84], respectively. In every analysis step, loading is increased until a single beam in the mesh reaches a stress/strength ratio equal to one. Subsequently, the beam is extracted from the mesh and this loading procedure is iterated until a predefined stopping criterion (e.g. load or displacement). Consequently, the fracture pattern of the investigated material volume at each step can be obtained as well as their load-displacement response. The mechanical properties of ITZ that were obtained could serve as a reference for the larger-scale simulation.

4.2 Modelling Approach

The lattice model is employed to investigate the material properties of ITZ and to observe the fracture behaviour of the microcubes. The parallel computing package used in this study was developed by Z. Qian [85], and it could simulate the stress-strain response, cracks pattern and microcracks propagation. During the modelling procedure, three stages are defined: pre-processing, fracture processes simulation and post-processing. Firstly, a lattice network is constructed, and the local mechanical properties are assigned to each lattice element in the pre-processing stage. The boundary conditions are imposed according to the test that is simulated. And then, according to the predefined failure criteria, the critical element will be removed from the system one by one, which represents the propagation of micro-cracks. Finally, the

mechanical response diagram and the crack pattern can be obtained in the post-processing stage. The simulation outcome will be verified by the experimental results. The study involves conducting a simulation in two stages: the lattice model with simplified microstructure and real microstructure. In the simplified model, the material is divided into three phases: fibre, ITZ and cement paste, with the size of the ITZ predefined manually. In the real model, there are two methods for material assignment: one involves thresholding to divide the material into five phases (fibre, pores, inner hydration product, outer hydration product and anhydrous cement), while the other assigns the material properties based on the grayscale value. The detailed procedures for constructing these models will be described in the following sections.

4.2.1 Lattice Model with Simplified Microstructure

A lattice model with a simplified microstructure was constructed to determine the general material properties of the ITZ. The 3D mesh was generated as shown in Fig. 4.1. To control computational cost, the size of the model was set as 30×30×30, and the cubic domain was divided into a cubic grid with a cell edge length of 10 μm. After the network of cells was generated, a sub-cell was defined within each cell. A lattice node was randomly placed within each cell, with its position determined by a randomness factor, which is the ratio between the length of the sub-cell and the cell. As shown in the previous study [86], randomness significantly affects the fracture behaviour of the specimens, as the orientation of the meshes influences crack propagation. A randomness factor of 0.5 was adopted to introduce geometric disorder in the materials and to avoid large variations in the length of elements. Subsequently, Delaunay triangulation was performed to connect the four nearest nodes with lattice elements. The cross-section of the lattice elements was then determined by adjusting this parameter in the model until the simulated global Young's modulus matched the assumed local value. The diameter of the fibre is 39 μm, and the outer diameter of the ITZ is set as 100 μm according to the observation in the previous study [7]. The schematic view of the simplified model is shown in Fig. 4.2. Regarding the boundary conditions shown in Fig. 4.3, the nodes on the bottom surface were clamped to represent the connections between the microcubes and their substrate. A vertical displacement was applied to the nodes in the centre top of the specimen, covering a width of 10 μm and a depth of 30 μm, to simulate the indenter load. To avoid affecting the experimental results, the failure mode of the boundary condition nodes was set to neither tension nor compression.

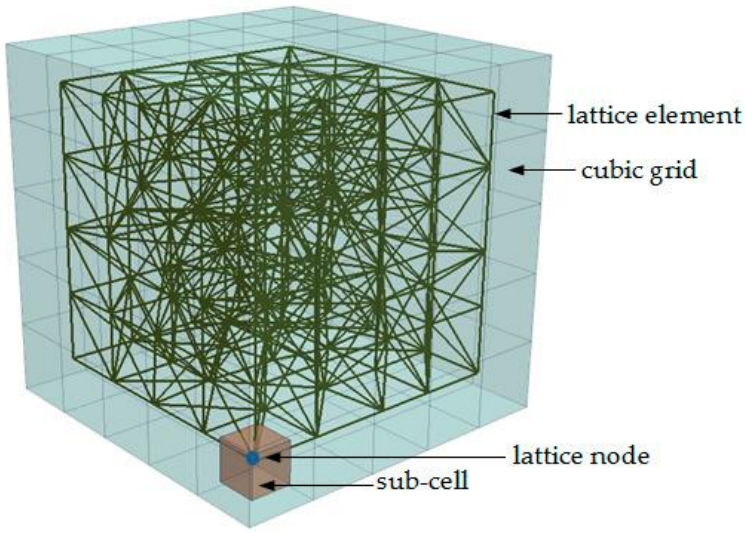

Fig. 4.1 Schematic view of lattice model generation

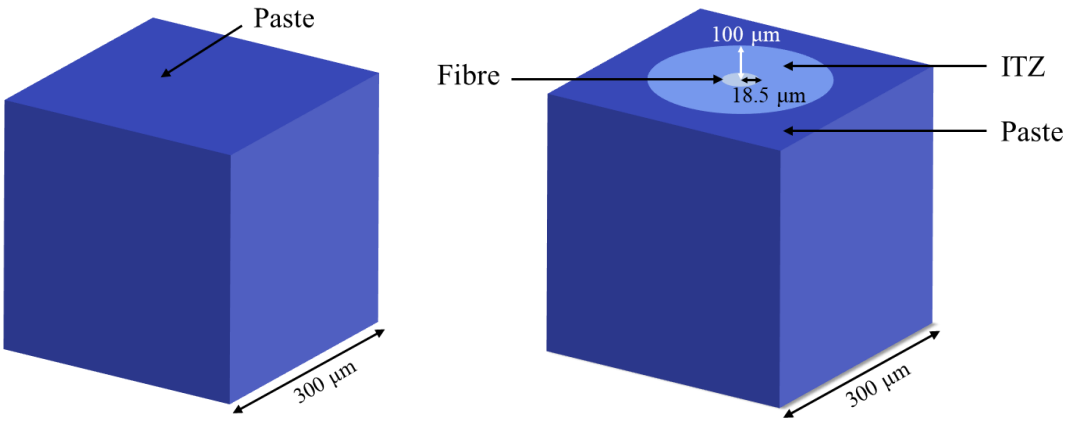

(a) (b)

Fig. 4.2 Schematic view of (a) reference model; (b) fibre model.

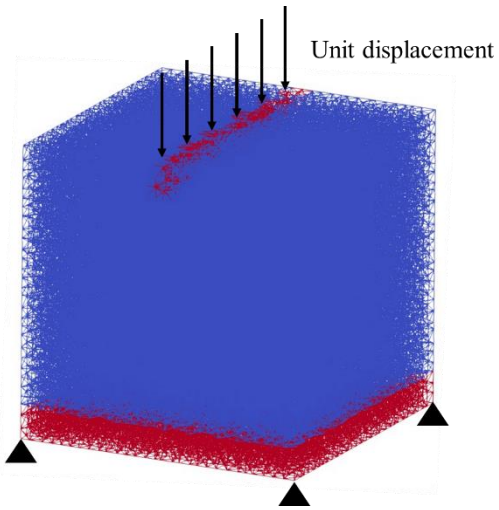

Fig. 4.3 Schematic view of boundary conditions

The reference model consists of a single phase, cement, while the fibre model includes three phases: fibre, ITZ, and paste. For each phase, the nodes within its area were assigned a specific number based on the voxel value, as shown in Fig. 4.4a.

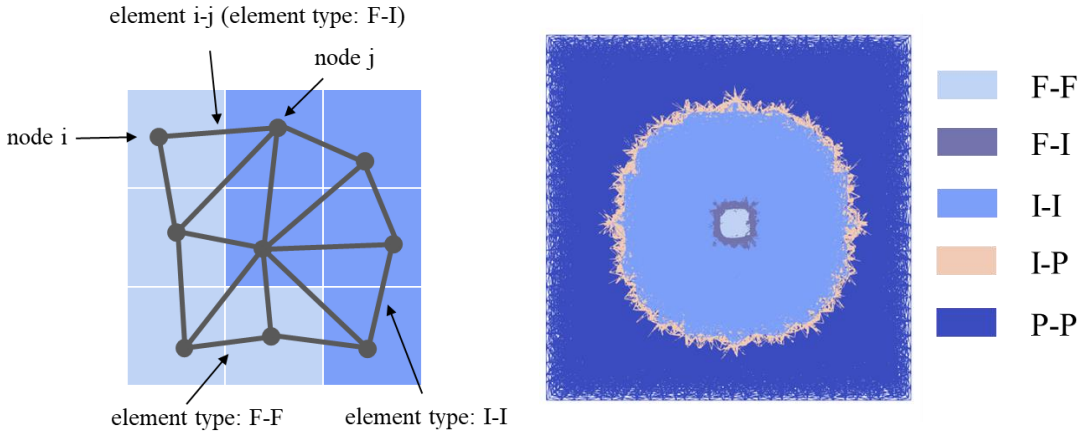

(a) (b)

Fig. 4.4. (a) overlay procedure for 2D lattice mesh; (b) element types (F-fibre; I-ITZ; P-paste).

The element type is determined by the location of its two nodes and five types of lattice elements were generated in the model with simplified microstructure, as shown in Fig. 4.4b. The shear modulus and Young's modulus of element i-j connecting phase I and phase j are determined as [83]:

$$\frac{2}{E_{ij}}=\frac{1}{E_i}+\frac{1}{E_j} \qquad \text{Eq. 3}$$

where E_i, E_j and E_{ij}, are the Young's modulus or shear modulus for phase i, phase j and element which connects phase I and phase j, respectively. The compressive strength and tensile strength take the lower value of the connected two phases, calculated by Eq. 4 as follows:

$$f_{ij}=\min(f_i,f_j) \qquad \text{Eq. 4}$$

where f_i, f_j and f_{ij}, are the compressive strength or tensile strength for phase i, phase j and element which connects phase i and phase j, respectively.

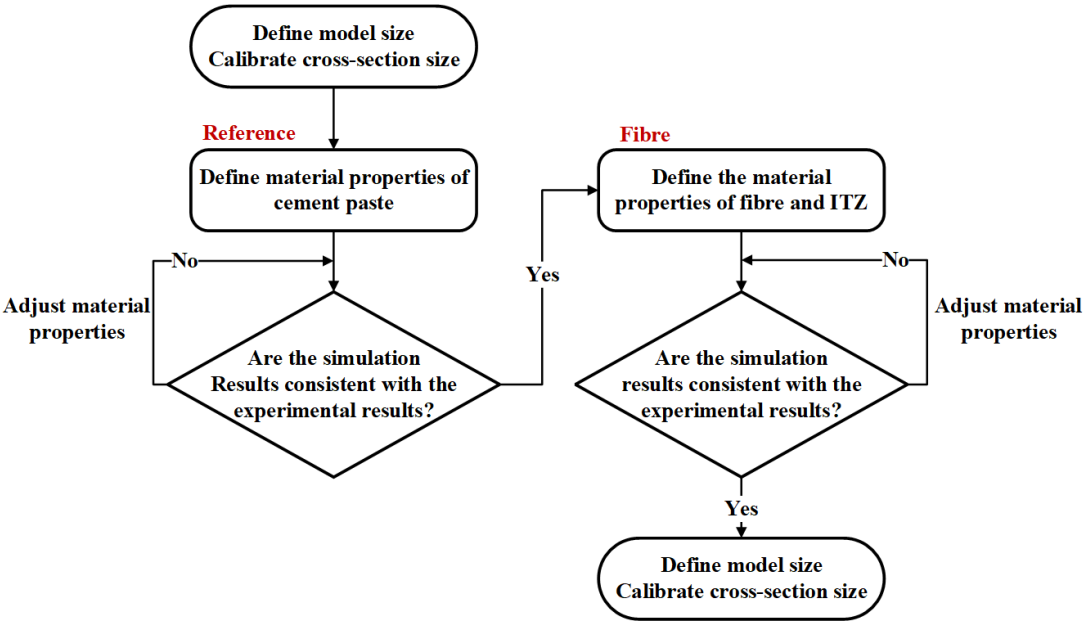

Fig. 4.5 Flowchart for calibrating the input material properties

Fig. 4.5 outlines a systematic procedure for calibrating the input material properties for the simplified model. Firstly, the model size was defined, and the cross-section size was calibrated, both the model size and cross-section size are the same for reference and fibre specimens. Next, the material properties of the cement paste are established and validated against experimental results, adjusting as necessary until consistency is achieved. Following this, the material properties of the fibre and the ITZ are defined. In this step, the material parameters for the ITZ were tested using different reduction factors applied to the validated material properties of the cement paste from the previous step. The detailed process of adjusting and validating the properties of the ITZ will be discussed later. Once both the cement paste and fibre/ITZ properties yield consistent simulation results, the final simulation results are obtained.

The initial material properties input of cement paste were derived from [87] and were adjusted based on the experimental result. The fibre parameters were derived from [6]. The input parameters for both the paste and fibre are listed in Table 4.

Table 4 Local mechanical properties of lattice elements in Fig. 4.2b

Phase		Young's modulus (GPa)	Compressive strength (MPa)	Tensile strength (MPa)
Fibre		12.5	50	50
Paste	w/c 0.3	22	280	22
	w/c 0.4	20	200	19
	w/c 0.5	16	140	16

The ITZ, as a distinct region exists between the fibre and paste. The purpose of creating this simplified model is to determine how much the properties of the ITZ are reduced compared to the paste. Therefore, the ITZ properties are based on the previously validated paste parameters and are tested with three different sets of parameters. In the first set, Young's modulus is reduced by 90%, and the compressive/tensile strength is reduced by 20-80%. In the second set, only Young's modulus is reduced by 20-80%. In the third set, both Young's modulus and compressive/tensile strength are simultaneously reduced by 20-80%. For the ITZ properties testing, the cement paste with a w/c ratio of 0.4 is used as the reference for these reductions.

The simulation results for different trial input sets for ITZ are shown in Fig. 4.6. For set 1, the stiffness of each curve is consistent due to the fixed 90% of Young's modulus, with the maximum load varying according to the reduction percentage. For set 2, the peak load and post-peak behaviour change significantly because the lower Young's modulus makes the material more ductile, resulting in lower load capacity but higher energy absorption. For set 3, both stiffness and peak load vary as the reduction percentage of Young's modulus and compressive/tensile strength change. This set most matches the experimental results; then it was applied to ITZ properties for w/c ratios of 0.3 and 0.5 for further validation.

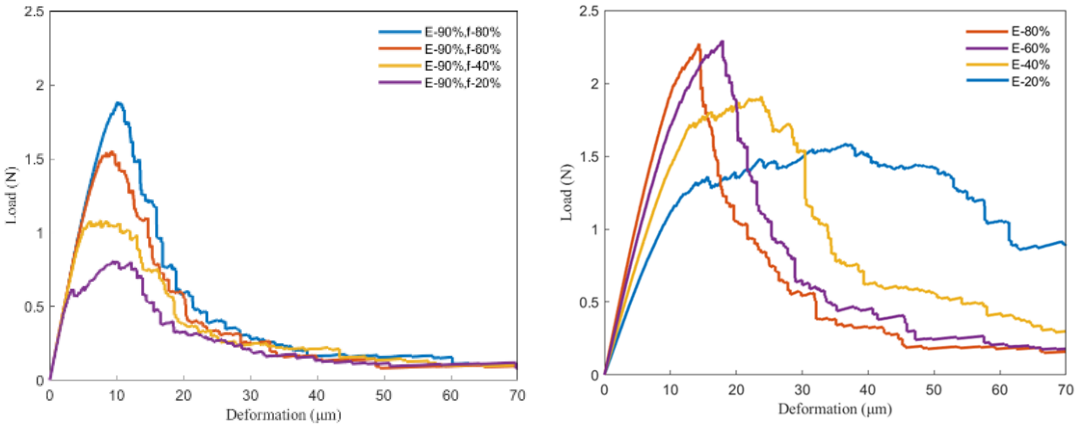

(a) (b)

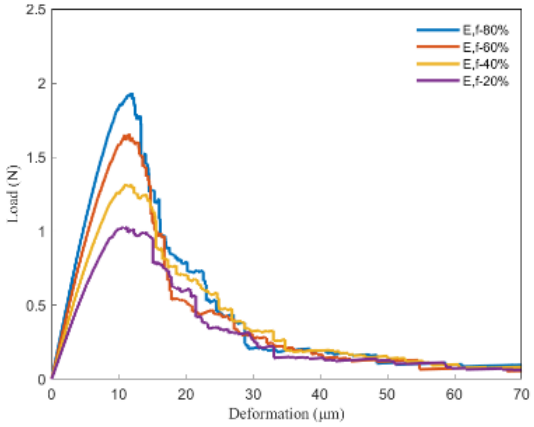

(c)

Fig. 4.6 Simulation result for different trial input sets for ITZ: (a) Set 1: Young's modulus is reduced by 90%, and the compressive/tensile strength is reduced by 20-80%; (b) Set 2: only Young's modulus is reduced by 20-80%; (c) Set 3: both Young's modulus and compressive/tensile strength are simultaneously reduced by 20-80%.

4.2.2 Lattice Model with Real Microstructure

Digital microcube specimens according to the real microstructure were generated by an XCT technique. A Micro CT scanner was used (CoreTOM) to obtain several greyscale images for reconstructing the 3D digital model. The microbeam was fixed on the holder and located on the rotatable stage. The X-ray source tube worked at 70 Kev/200mA. 900 images with an exposure of 6 s were acquired on a digital GE DXR detector. The voxel resolution under these conditions was 5.64 μm^3. The 3D visualization was conducted using Dragonfly software. To reduce the computational cost, the original resolution of the reconstructed slices was down-sampled to 364

μm^3/voxel through the application of a Mean filter. The size of the model was set as 42×42×42 and the cubic domain was divided into a cubic grid with a cell edge length of 7.14 μm.

In this section, two different methods of assigning material properties were compared. The first method involves dividing the specimens into five phases (fibre, pores, outer product, inner product, and anhydrous cement). The lattice node in the voxels, which represent pore phases, is removed, as it does not contribute to the global mechanical performance of the specimen. The second method assigns material properties directly based on the grayscale values of the image, without distinguishing between phases. Apart from the material properties assignment, the other modelling steps are identical to those used for the simplified model.

The process of image segmentation was conducted using an approach known as global thresholding [74, 88]. In this method, the phases were separated from the original grey-scale map by sequentially selecting the appropriate threshold. First, two threshold grey values are selected based on the grey-level histogram depicted in Fig. 4.7: T1, the threshold for the fibre and pore phases/other solid phases, is defined as the grey value at the point where the cumulative fraction curve of the histogram inflected. Due to the similar grayscale values of the fibre and pores, a cylindrical mask was manually added during image processing to distinguish between the fibre and pore phases. T2, the threshold for hydration products/anhydrous cement phase, is a key point where the slope of the histogram rapidly changes. Four phases can be easily identified: the pore phase, the fibre phase, the anhydrous cement phase, and the hydration product phase. Typically, hydration products can be divided into the following three phases through thresholding [88-91]: the inner product C-S-H_{LD}, the outer product C-S-H_{HD}, and C-H. To simplify the process, the C-H phase was not treated as an individual phase and was not explicitly simulated. This simplification is considered to have an insignificant impact on the outcomes of the mechanical properties. However, it is important to regard C-H as a distinct phase in future research. The segmented phases are shown in Fig. 4.8a. After the image segmentation, the binary images representing different phases are taken as inputs for the model. The dimensions of these images are then determined, allowing for the reallocation of a 3D matrix to store the phase data. Subsequently, the binary images corresponding to each phase are appropriately labelled within the 3D matrix. The reconstructed 3D model is shown in Fig. 4.8c, where phases 1-5 represent the anhydrous cement, inner product, outer product, pore and fibre. The material properties input of each phase were derived from [51] and the input parameters are listed in Table 5.

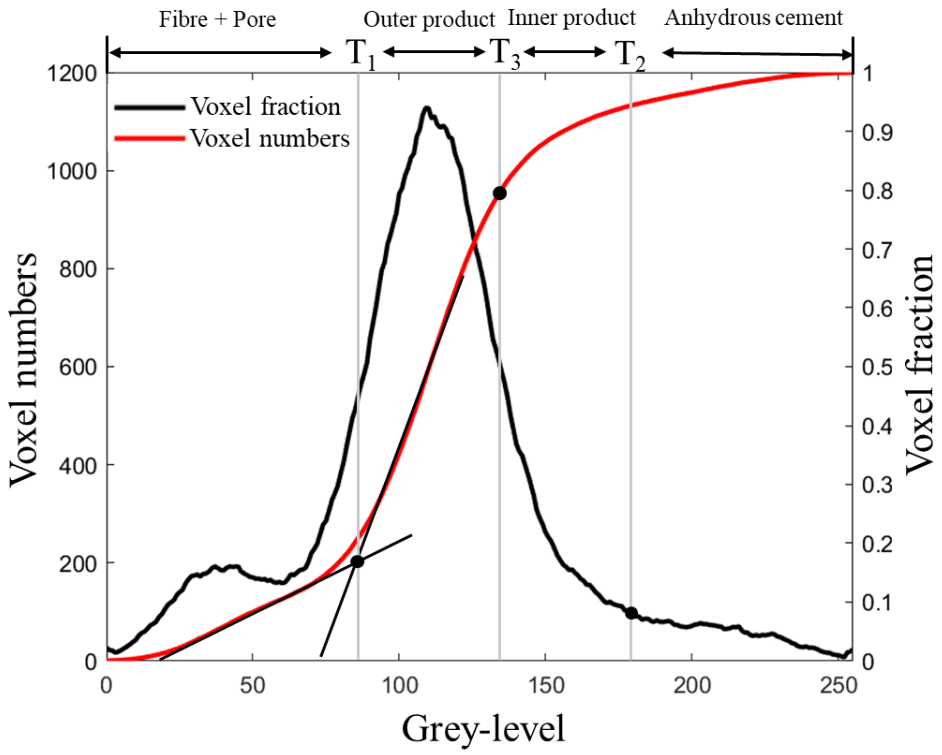

Fig. 4.7 Phases evolution through greyscale level histogram of CT images.

Table 5 Local mechanical properties of different phases for the thresholding method

Phase	Young's modulus (GPa)	Compressive strength (MPa)	Tensile strength (MPa)
Anhydrous cement	99	683	68.3
Inner hydration product	31	92	9.2
Outer hydration product	25	58	5.8
Fibre	12.5	50	1230

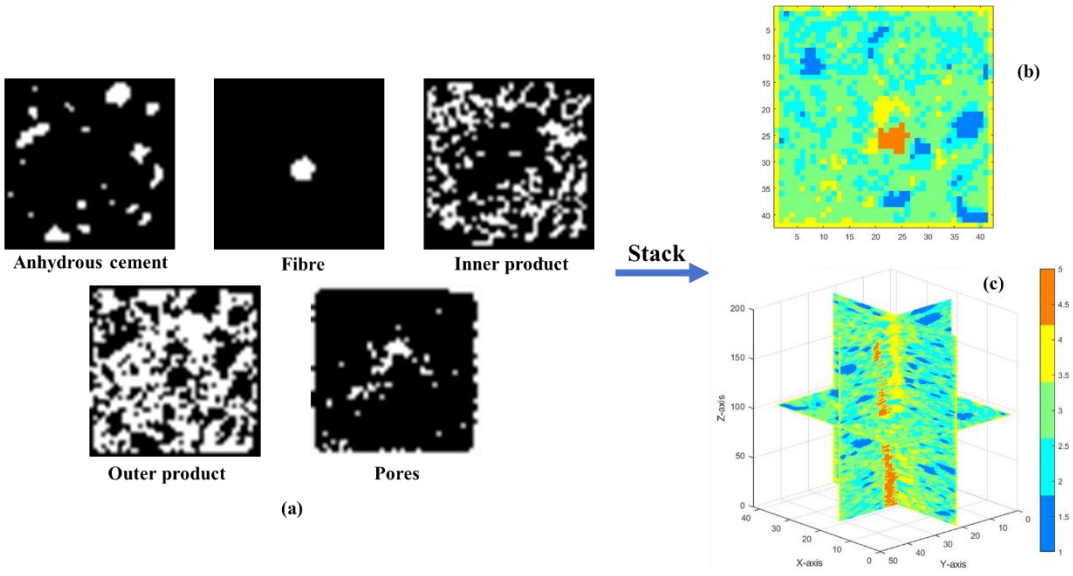

Fig. 4.8 The procedure of 3D digital specimen construction: (a) the binary images of segmented phases; (b) the cross-section of the reconstructed digital specimen; (c) the 3D view of the segmentation matrix (phase 1-Anhydrous cement, phase 2-Inner product; phase 3-Outer product; phase 4-Pore; phase 5-Fibre).

While phase segmentation can be used to determine the spatial distribution of different hydration phases, it is not a generally standardized technique. Numerous segmentation methods are available, making it challenging to determine which method yields more precise outcomes. For instance, the determined volume of the pore phase varies considerably according to the segmentation method used. As the models are constructed, more factors contribute to uncertainty. It would be highly beneficial to reduce the subjectivity in the thresholding process of the multi-phase material structure. Zhang et al. [92] developed a new method for micromechanical simulation of cement paste based on a combination of statistical nanoindentation and XCT technique without the need for explicit identification of distinct phases. The material structure of cement paste was characterized using XCT, along with the associated histogram of grey scale distribution. The statistical nanoindentation technique was employed to quantify the probability density function (PDF) of micromechanical characteristics.

In this part, the material attributes are allocated using this technique and contrasted with the thresholding method previously discussed. The local Young's modulus of a voxel at a certain greyscale level g can be determined as follows:

$$E_{\text{local}}=\text{Min}\left(F(x)\right)+\left(\text{Max}\left(F(x)\right)-\text{Min}\left(F(x)\right)\right)\frac{g-T_g}{(255-T_g)} \qquad \text{Eq. 5}$$

where T_g is the greyscale that corresponds to the voxel having a modulus equal to zero and equals 42 in this case. Min(F(x)) and Max(F(x)) are the minimum and maximum values that can be derived from Young's modulus histogram and are equal to 1 GPa and 120 GPa respectively.

The local tensile strength can be determined as:

$$F_{\text{local}} = \frac{\text{a}E_{local}^{b}}{12} \qquad \text{Eq. 6}$$

where a and b are the empirical constants fitted from the experimental results. In this case, a = 0.004288 and b = 1.626. Relationships mentioned in this section are used in the model as a comparison to the thresholding method.

4.3 Results and Discussion

4.3.1 Lattice Model with Simplified Microstructure

Fig. 4.9 presents a comparison between the simulated load-displacement curves of simplified reference specimen models with w/c ratios of 0.3, 0.4 and 0.5. For comparison, the experimental load-displacement curves of 10 specimens were plotted. As stated above, the horizontal line represents the overshoot behaviour of the indenter. Since the post-peak behaviour cannot be captured experimentally at present, only the ascending branch was used for the comparison. It is obvious that the simulation results for all w/c ratios have a good agreement with the experimentally measured curves in terms of the maximum load and slope of the load-displacement curve (stiffness). Due to the local imprinting of the indenter into the micro-cube occurring at the beginning of the experiments, the measurements are slightly shifted, but the slope remains similar to that of the simulated load-displacement curve. Furthermore, the simulations show a post-peak response, which cannot be observed experimentally due to the previously described equipment limitations. Additionally, the experimental results indicate that the standard deviation of the test results significantly increases as the w/c ratio increases. The high variability is introduced by the inherent heterogeneity of this material at the micro-scale.

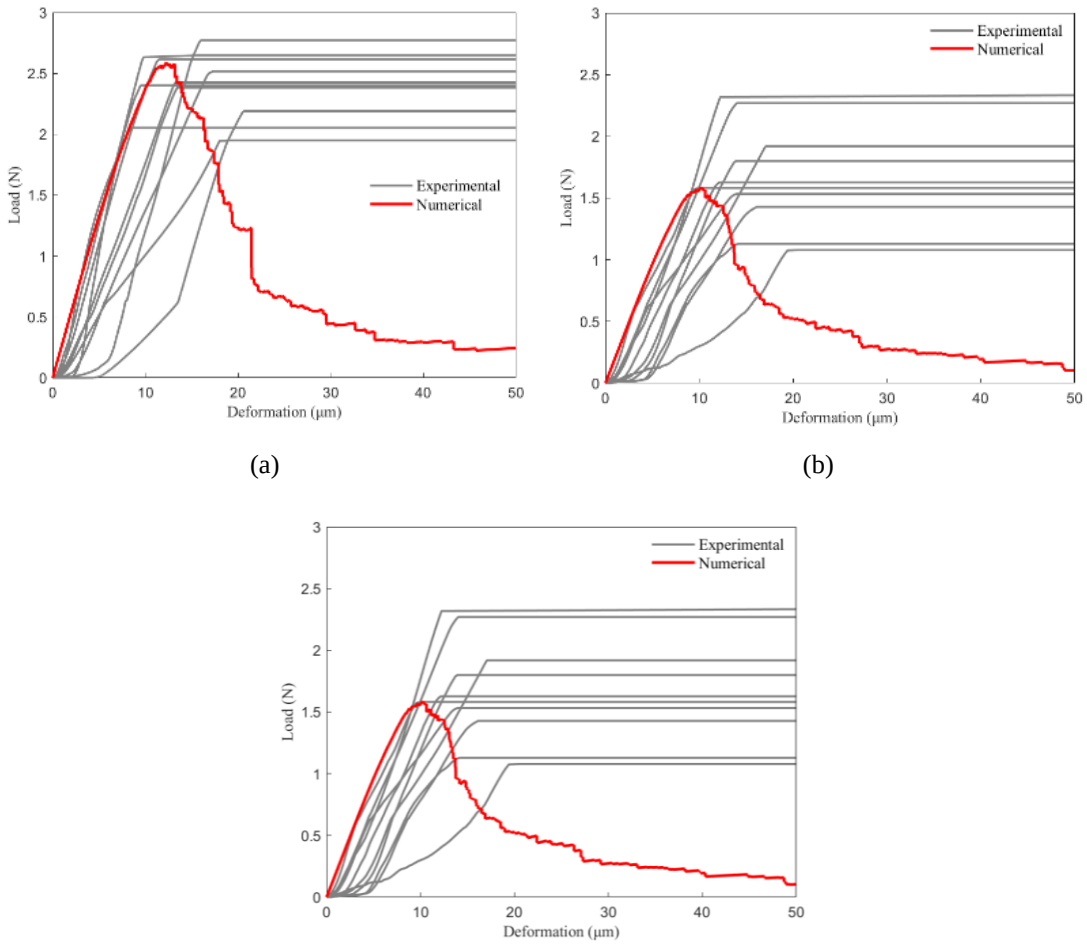

Fig. 4.9 The experimental and numerical results of simplified reference specimen models with w/c ratio of (a) 0.3; (b) 0.4; (c) 0.5

The simulated crack pattern of a reference micro-cube under indentation splitting is shown in Fig. 4.10. There is only one type of element included in the figure, which is the cement paste. The highlighted red elements represent the paste elements that have failed. By observing the trend of these highlighted elements, the crack propagation within the specimen can be clearly observed. The figure only shows the crack development of the w/c ratio of 0.3 since the simulated fracture behaviour of the other two w/c ratios is similar to the w/c ratio of 0.3. Initially, the crack initiates at the centre of the upper part of the specimen, where the indenter applies the load. As the load increases, the crack propagates downward through the middle part of the specimen, indicating that the stress concentration moves towards the interior of the micro-cube. Eventually, the crack extends further, running through the entire central region of the micro-cube, resulting in a complete split of the specimen into two halves. The simulated crack pattern follows the experimental observation as shown in Fig. 3.6.

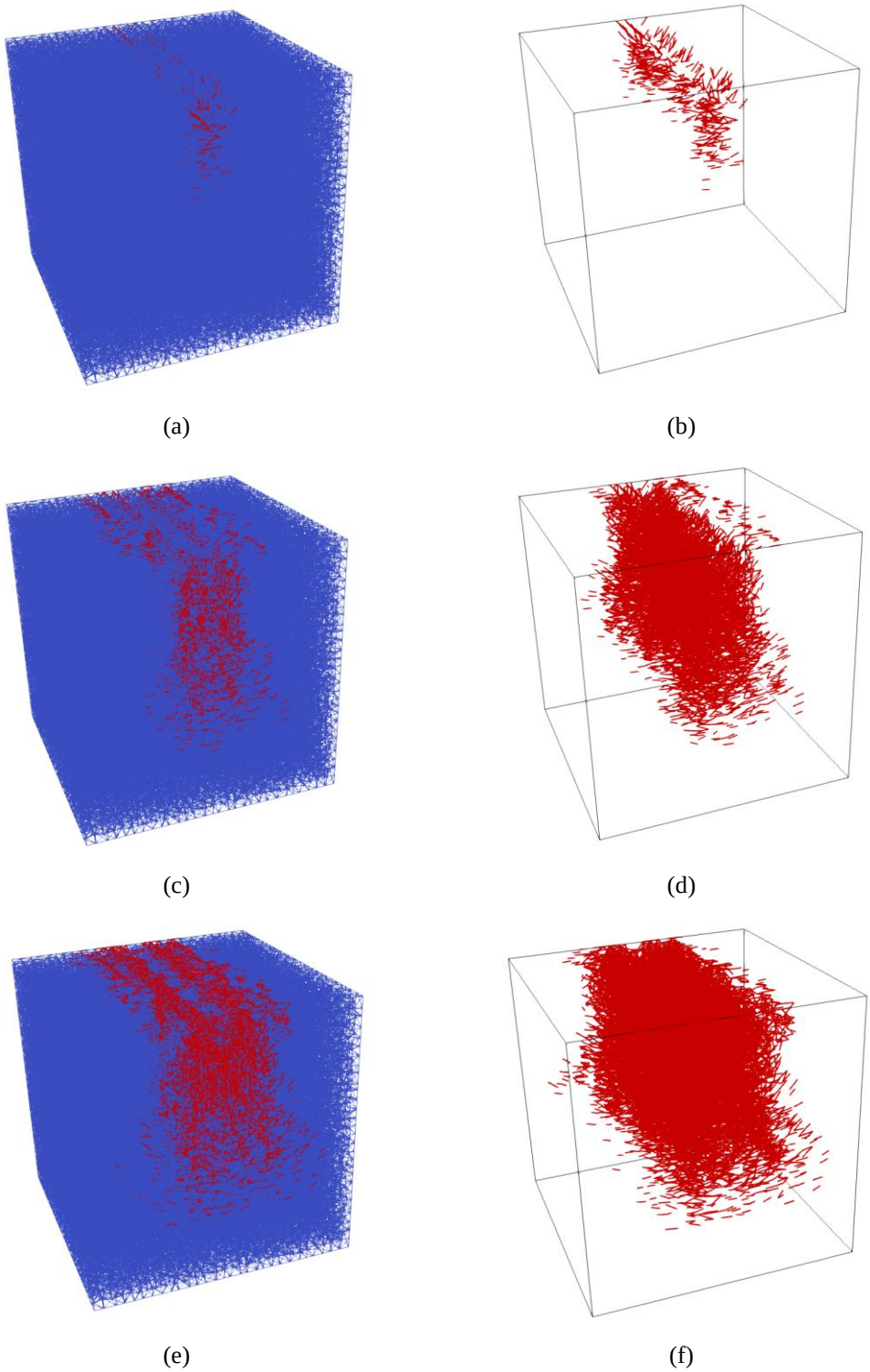

(a) (b)

(c) (d)

(e) (f)

Fig. 4.10 Simulated crack pattern of a reference micro-cube under indentation splitting: (a) crack initiates at the centre of the upper part of the specimen; (b) visualization of the crack at the initial stage; (c) crack propagates from the middle part of the specimen; (d) visualization of the crack at the crack propagation stage; (e) crack propagates through the centre of the micro-cube and it is split in half; (f) visualization of the crack at the final stage.

Fig. 4.11 presents a comparison between the simulated load-displacement curves of simplified fibre specimen models with w/c ratios of 0.3, 0.4 and 0.5. Each subplot compares experimental load-displacement curves with numerical results at different percentages of the material parameter input (20%, 40%, 60%, 80%). Similar to the figures of reference results, the experimental load-displacement curves of 10 specimens were plotted for comparison. The experimental results exhibit a large range of variability, so a red dashed line representing the average experimental results is included to facilitate comparison with the numerical results at different material parameter inputs. As the w/c ratio increases from 0.3 to 0.5, both the experimental and numerical peak loads decrease. For all w/c ratios, the range of the experimental results encompasses the 20% and 40% numerical simulation results, with the average experimental result being closer to the 20% material input simulation. This provides a reference for the material input parameters considering the ITZ in the simulations, suggesting that regardless of the w/c ratio, the material properties of the ITZ are approximately equivalent to 20% of the paste properties. In the single fibre pullout test simulations conducted in Chapter 5, the material parameters for the ITZ were taken as 20% of the paste material properties.

Fig. 4.12 presents the simulated crack pattern of a micro-cube containing fibre under indentation splitting. The model includes five types of elements. The red-highlighted elements in the figure indicate failed elements, with subfigures (c), (f), and (j) marking the types of these failed elements. The figure only shows the crack development for the w/c ratio of 0.3, as the simulated fracture behaviour for the other two w/c ratios is similar to that of 0.3. The crack initial at the centre of the micro-cube, as shown in Fig. 4.12c, where all types of elements below the indenter tip begin to fail. As the load increases, the crack propagates downward from the middle part of the specimen, with microcracks primarily spreading in the ITZ phase and a few fibre elements failing. Eventually, almost all ITZ elements in the centre failed, along with the paste elements beneath the indenter tip. A significant number of fibre elements also fail, consistent with the experimental observations shown in Fig. 3.6d.

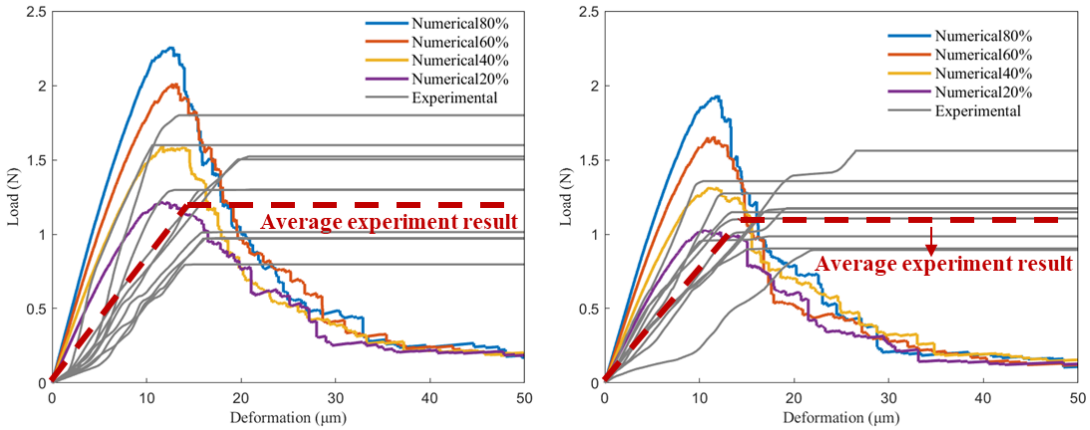

(a) (b)

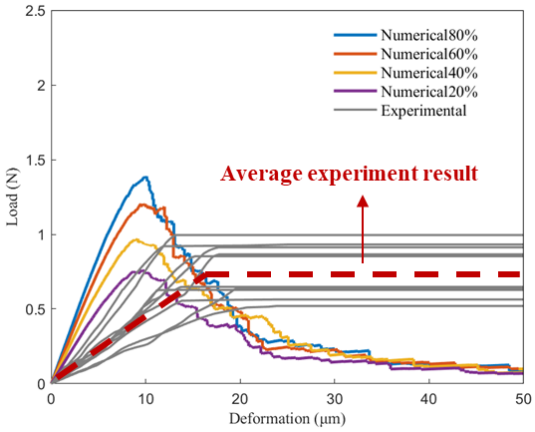

(c)

Fig. 4.11 The experimental and numerical results of simplified fibre specimen models with w/c ratio of (a) 0.3; (b) 0.4; (c) 0.5.

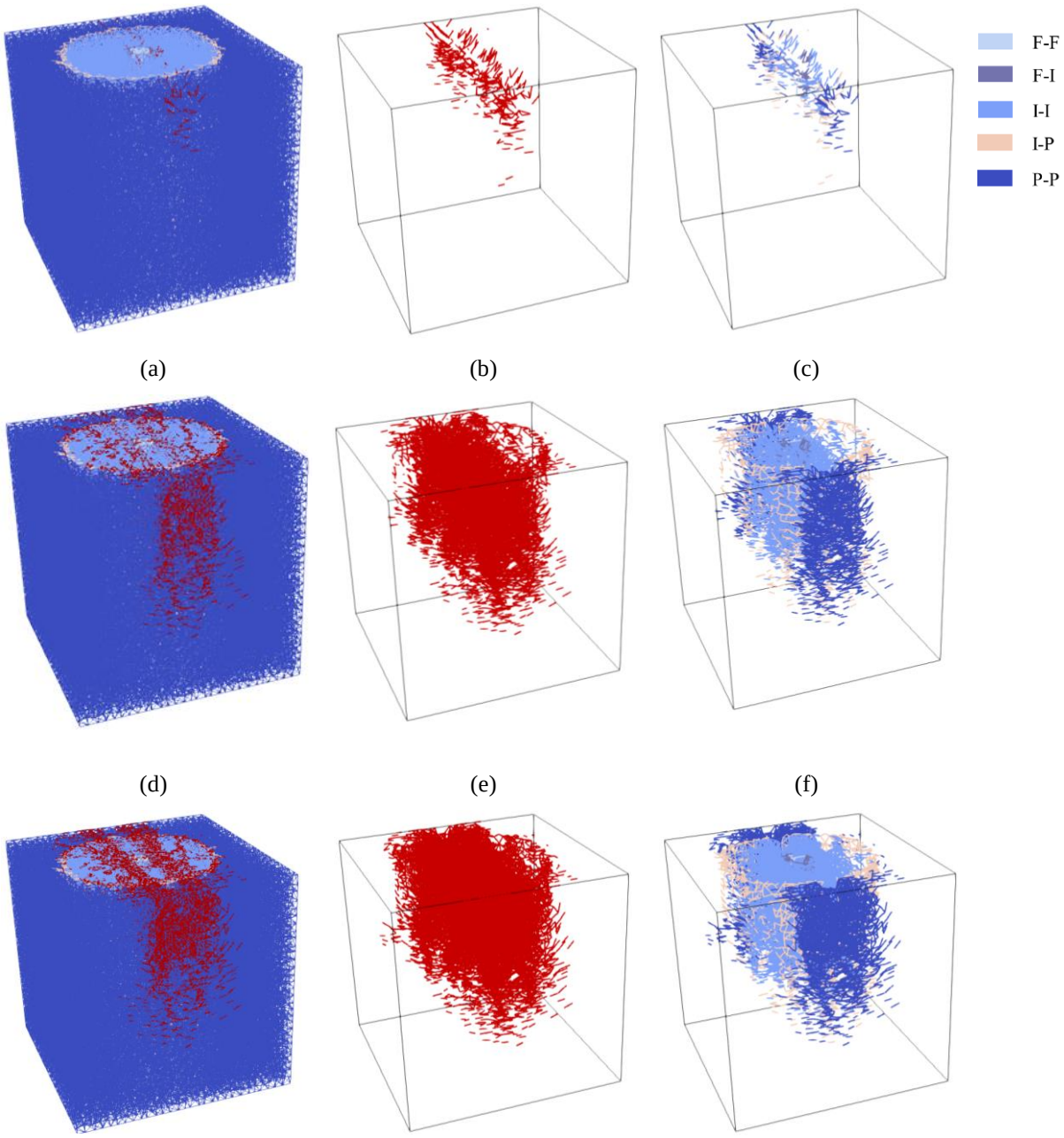

Fig. 4.12 Simulated crack pattern of a micro-cube containing fibre under indentation splitting: (a) crack initiates at the centre of the upper part of the specimen; (b) visualization of the crack at the initial stage; (c) visualization of failed element at the initial stage; (d) crack propagates from the middle part of the specimen; (e) visualization of the crack at the crack propagation stage; (f) visualization of failed element at the crack propagation stage; (g) crack propagates through the centre of the micro-cube and it is split into two halves; (h) visualization of the crack at the final stage; (i) visualization of the crack at the final stage.

4.3.2 Lattice Model with Real Microstructure

Fig. 4.13 illustrates the comparison between the material properties input for greyscale mapping (red lines) and thresholding methods (blue lines) across different metrics: Young's modulus, compressive strength, and tensile strength versus grey level. It is important to note that the purpose of this section is to compare the differences between the two methods. Since the grey level of the fibre is close to that of the pore, the fibre is merged into the pore phase and assigned the same value in the thresholding method.

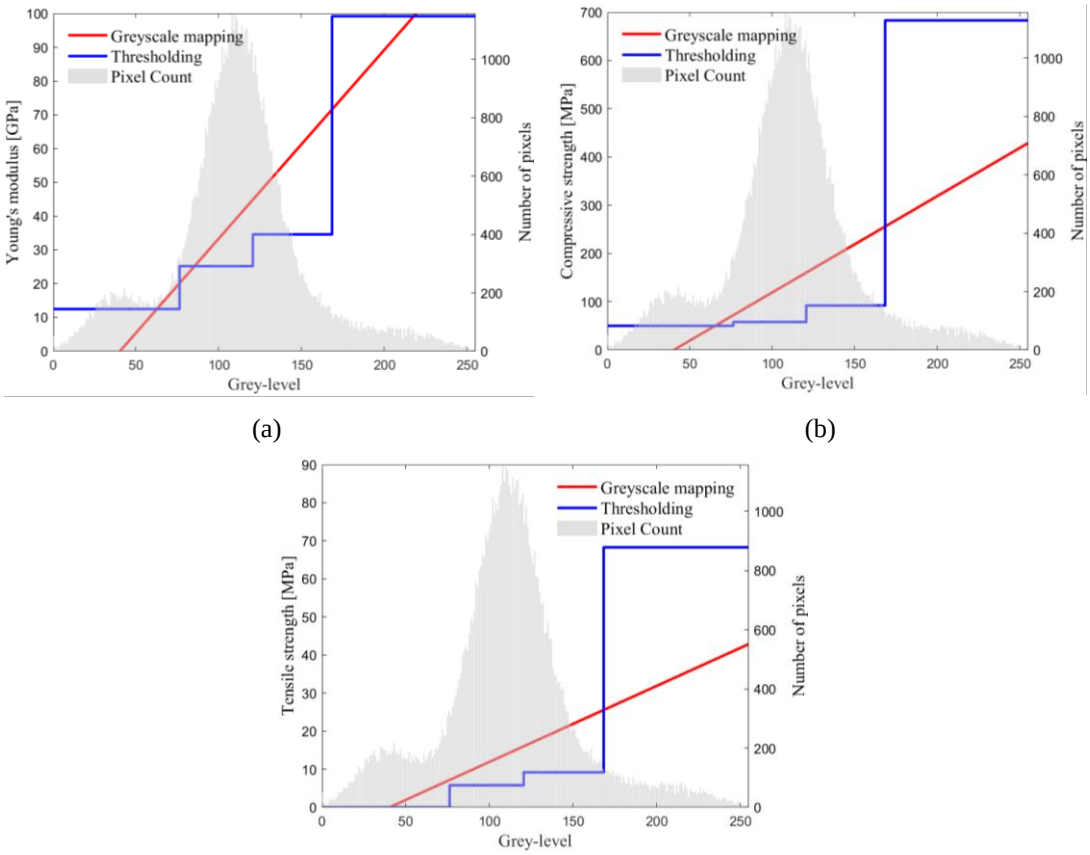

Fig. 4.13 Comparison between the material properties input for greyscale mapping and thresholding method

The numerical results of the thresholding and greyscale mapping methods for a fibre specimen with a w/c ratio of 0.5 are compared in Fig. 4.14. It is evident that there are significant differences between the two methods. The greyscale mapping method shows a peak load approximately twice that of the thresholding method, although both methods yield a similar Young's modulus. In a previous study [92], the two-sample Kolmogorov-Smirnov (K-S) statistic test was used to verify the hypothesis of a linear relationship between the probability density functions of the greyscale values and the input material parameters. It was confirmed

that Young's modulus has a linear relationship with the grey level, and in this section, the simulated results of Young's modulus for both methods are also similar. Another parameter obtained by nanoindentation is microhardness, which can be linked to the ultimate tensile strength of the probed microvolume. However, the linear relationship between hardness and grey level was refuted by the K-S test. Consequently, an empirical model was proposed to correlate hardness with its corresponding Young's modulus. The empirical constants in Eq. 6 were fitted from experimental results in previous literature. However, this study directly uses those empirical constants, which may explain the significant difference observed in the peak load. Furthermore, as shown in Fig. 4.13, the strength input of anhydrous cement is significantly higher than that of greyscale mapping. The discrepancy in material parameter inputs also leads to substantial differences in the results obtained from the two methods.

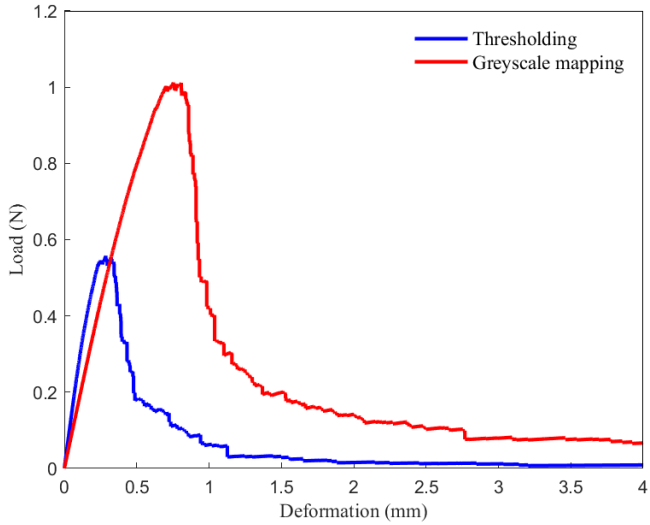

Fig. 4.14 The numerical result of thresholding and greyscale mapping method for fibre specimen with w/c ratio of 0.3

The simulated crack patterns of the model with real microstructure using thresholding and grey-scale mapping methods are shown in Fig. 4.15 and Fig. 4.16, respectively. The result of the model using the thresholding method can be easily visualized with different element types. In Fig. 4.15, the cracks initially appear in the middle of the sample and gradually propagate downward. However, since the input material properties of anhydrous cement are significantly higher than the other phases, the elements representing the anhydrous cement (deep blue elements) have not reached their failure criteria. Therefore, the cracks follow a downward path in the middle of the microcube but extend around the anhydrous cement particles. In the model using the grayscale mapping method, the material parameters of the elements are more uniform compared to the thresholding method, resulting in a fracture pattern similar to the simplified model shown in Fig. 4.12.

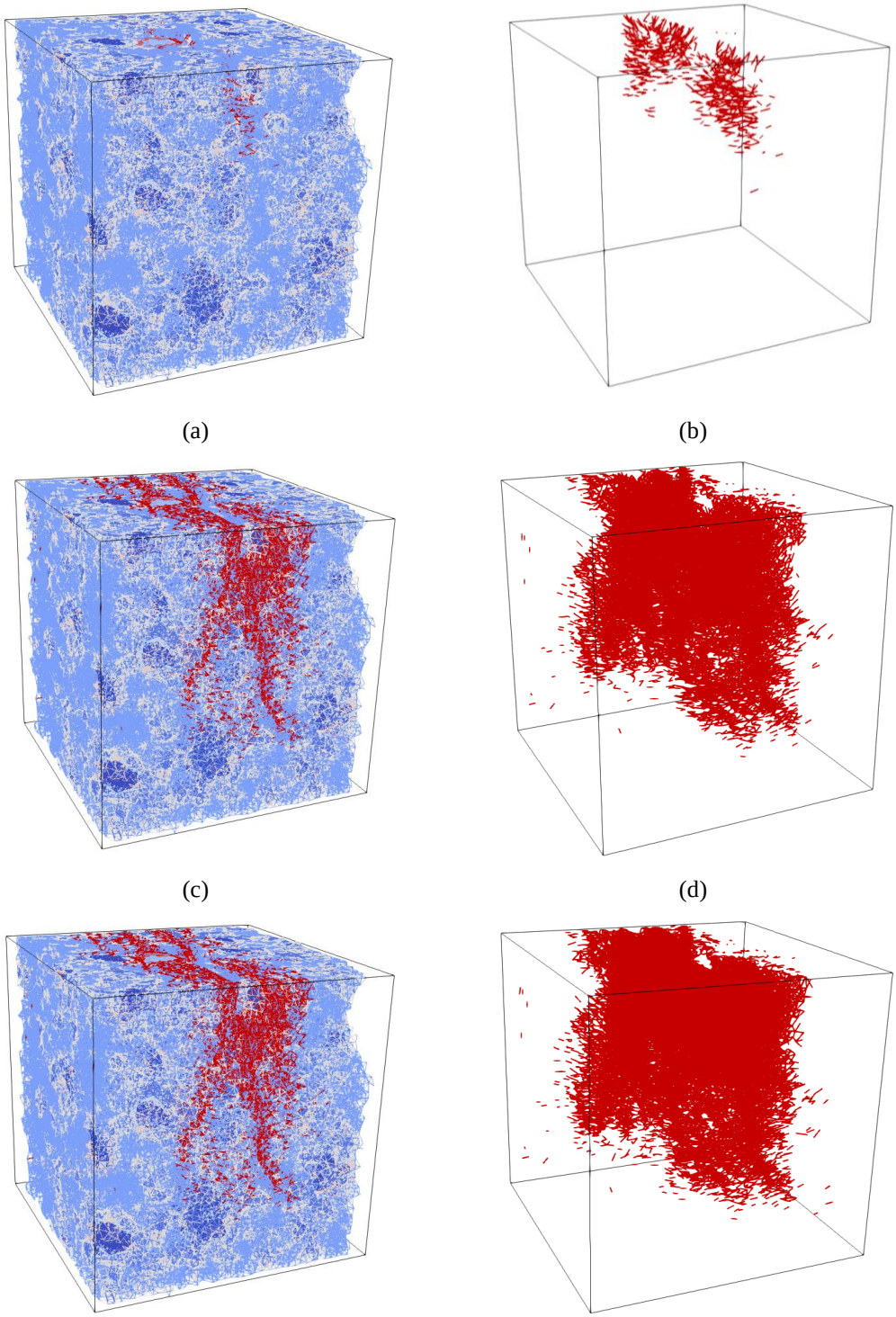

Fig. 4.15 Simulated crack pattern of the real microstructure model using thresholding method: (a) crack initiates at the centre of the upper part of the specimen; (b) visualization of the crack at the initial stage; (c) crack propagates from the middle part of the specimen; (d) visualization of the crack at the crack propagation stage; (e) crack propagates surrounding the anhydrous cement particles; (f) visualization of the crack at the final stage.

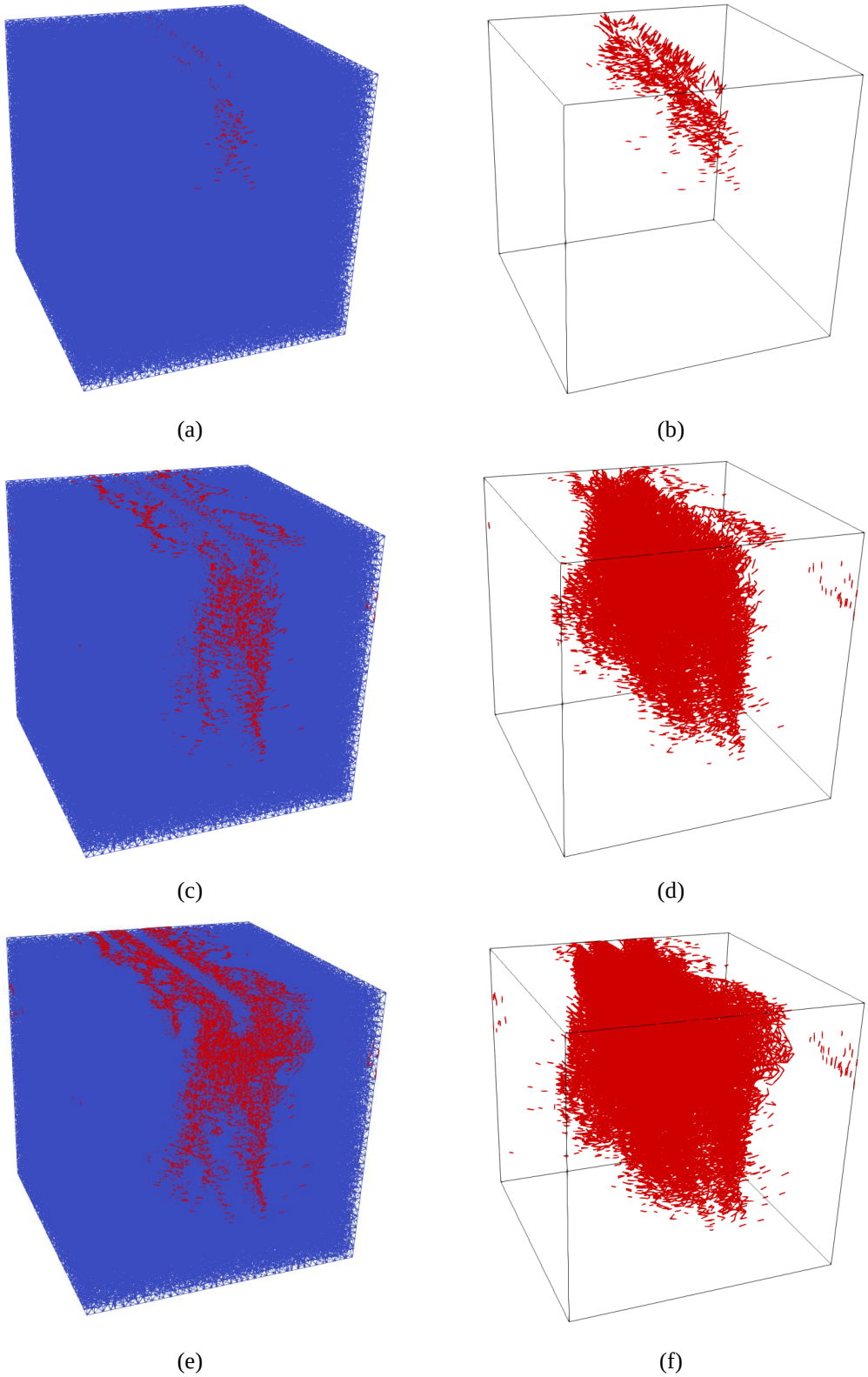

Fig. 4.16 Simulated crack pattern of the real microstructure model using greyscale mapping method: (a) crack initiates at the centre of the upper part of the specimen; (b) visualization of the crack at the initial stage; (c) crack propagates from the middle part of the specimen; (d) visualization of the crack at the crack propagation stage; (e) crack propagates through the centre of the micro-cube and it is split in half; (f) visualization of the crack at the final stage.

4.4 Conclusions

Lattice models with simplified and real microstructures were built in this Chapter. For the simplified model, the mechanical properties of local phases were calibrated by validating the simulated results with the experimental results. It is shown in this chapter that the adopted mechanical properties of local phases are critical for the investigation in terms of load-displacement response and failure mechanism. Therefore, it is of great importance to fit these parameters by designing experiments on specimens of the same size as well as under well-controlled boundary conditions. The modelling result of the model with simplified microstructure shows that the material properties of the ITZ are approximately equivalent to 20% of the paste properties regardless of the w/c ratio. The lattice model with real microstructure was built based on a microstructure of cement paste prisms containing one single fibre obtained from XCT. For the this model, two material assignment methods, thresholding and greyscale mapping, were compared. The simulation results showed significant differences between the two methods, which may be attributed to the empirical parameters used to calculate tensile strength. These parameters were directly taken from previous literature without experimental validation in this study.

5

Testing and Modelling on Single Fibre Pullout Behaviour

Chapter 5 details the experimental and modelling procedures and results of the single fibre pullout test, discussing the relationship between the microscale test results and the outcomes of the pullout test.

5.1 Introduction

In this chapter, single fibre pullout tests were conducted to evaluate the composite performance and the interphase properties. To simulate the debonding phase of the fibre pullout process, a single fibre pullout model with simplified microstructure was developed. The microstructure features of the ITZ were characterised using X-ray computed tomography (XCT). The mechanical properties of ITZ, as derived from Chapter 4, were used as input for the model. The modelling results were then compared with the experimental results for validation.

5.2 Materials and Tests

5.2.1 Materials and Sample Preparation

The materials involved in the single fibre pullout test are the same as those used in the indentation splitting tensile test, as mentioned in Section 3.2.1. After the cement paste prisms shown in Fig. 3.1a were cast and cured for 28 days, slices were cut using a low-speed saw (Minitom, Struers) with fibre protruding from both ends of the specimen, as shown in Fig. 5.1a. The thickness of the sample, which also represents the embedded length (L_e) of fibre, was controlled to be around 1 mm to avoid fibre rupture during the pullout process. The cut pullout specimen was glued to a hex nut using a strong adhesive, as shown in Fig. 5.1b. The centre of the fibre was aligned with the centre of the hex nut, with only the surrounding paste affixed to the hex nut.

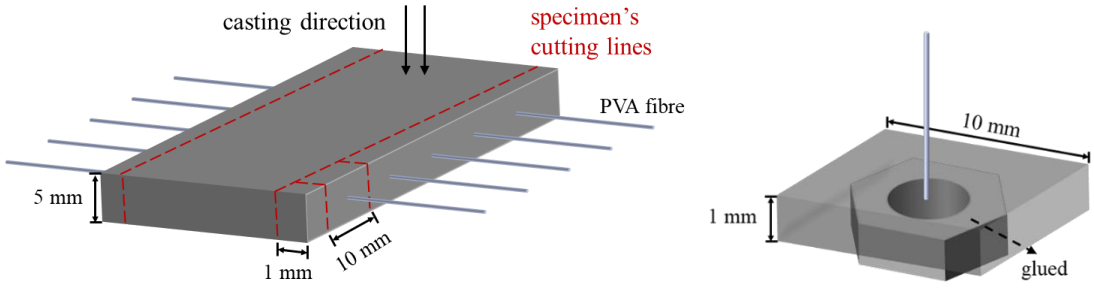

(a) (b)

Fig. 5.1 The specimens of single fibre pullout test cut from the cement paste prism

5.2.2 Test

The interface bonding properties were evaluated through a single fibre pullout test based on the method outlined by Redon et al. [16], and the test set-up is a micro tension-compression testing device from Kammrath & Weiss GmbH, as shown in Fig.5.2. The bottom of the hex nut and

the free end of the PVA fibres in Fig. 5.1b was glued to two small metal blocks which were then clamped using an actuator and a load cell with 50 N capacity, respectively. The pullout process was executed at a displacement rate of 0.005 mm/s. The interface bond properties were characterized based on the principles introduced by Lin et al. [93], encompassing the chemical bond strength G_d quantified by interfacial fracture toughness, the constant frictional bond strength τ_0 for small sliding and the slip hardening coefficient β representing the increasing effective frictional bond during large sliding (pullout) stage. Around 10 specimens were tested for each mixture, the results of which were then analysed to determine the interface properties according to Eq. 7-Eq. 9:

$$G_d = \frac{2(P_a\text{-}P_b)^2}{\pi^2 E_f d_f^3} \quad \text{Eq. 7}$$

$$\tau_0 = \frac{P_b}{\pi d_f L_e} \quad \text{Eq. 8}$$

$$\beta = \frac{d_f}{L_e}\left(1+\frac{1}{\pi\tau_0 d_f}\cdot\frac{\Delta P}{\Delta u'}\Big|_{u'\to 0}\right) \quad \text{Eq. 9}$$

where E_f, d_f and L_e represent the elastic modulus [GPa], diameter [mm], and embedded length of PVA fibre [mm], respectively. $\Delta P/\Delta u$ is the initial slope of the pullout load vs displacement. P_a represents the maximum load up to full deboned length, while P_b represents the load at which the fibre begins to slip.

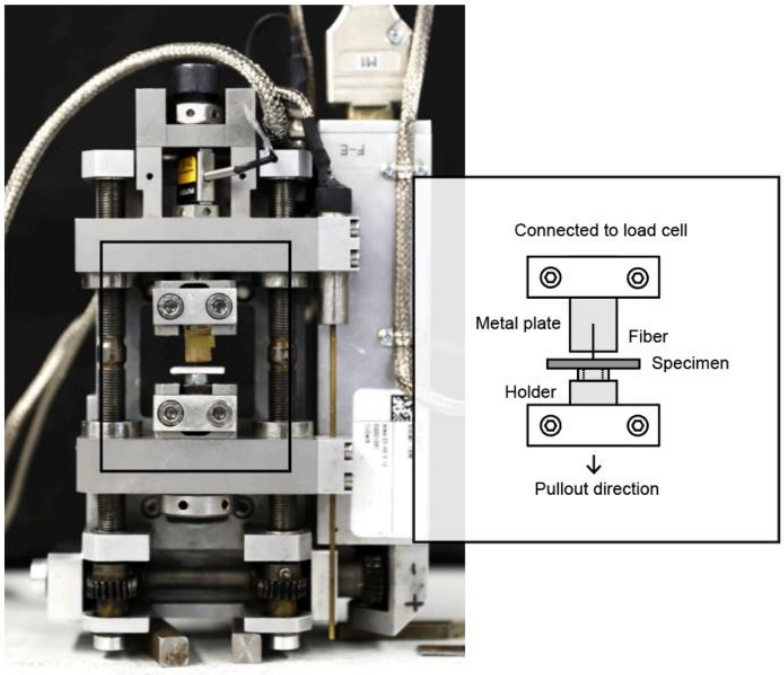

Fig.5.2 Experimental set-up for single fibre pullout test [17]

5.2.3 Modelling Approach

The lattice model with simplified microstructure mentioned in Section 4.2.1 was applied to conduct the single fibre pullout simulation. Except for the mesh size and the boundary conditions, the other settings were the same as the simplified model in Chapter 0. Similarly, the simulations in this chapter only involve CEM I materials.

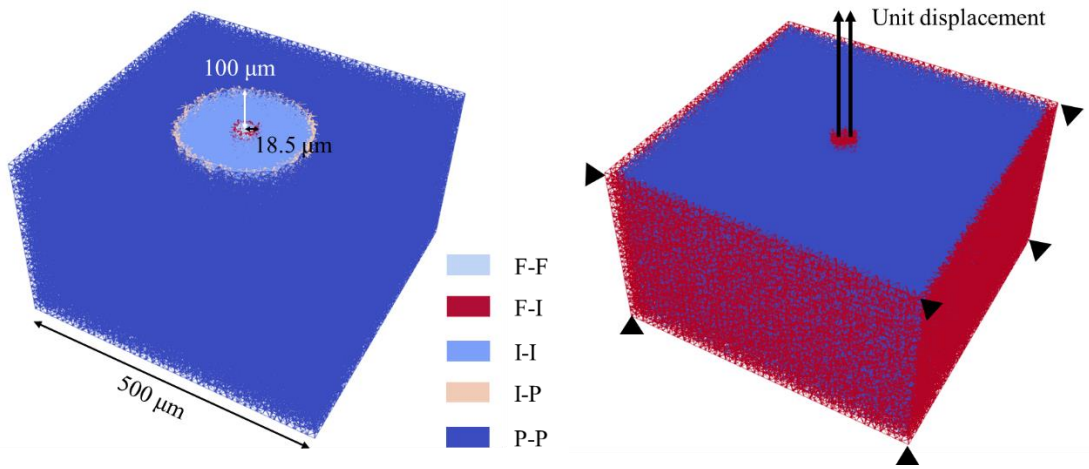

(a) (b)

Fig.5.3 Schematic view of (a)single fibre pullout model; (b)its boundary conditions

In single fibre pullout tests, the affected range of the cement matrix depends on the type of fibre and the strength of the matrix. Studies have shown that for steel fibres, the impact zone in the cement matrix can extend up to several hundred μm. Specifically, a damaged zone typically forms around the crack tip in the cement matrix, with a radius usually ranging from 100 to 500 μm [94]. To encompass the fibre pullout effect on the paste as much as possible while minimizing the computational load, the model dimensions were set to 500 μm × 500μm × 300 μm. The element types used in this section are the same as those described in Section 4.2.1, including three phases and five types of elements. The cross-section of the lattice elements was also calibrated until the simulated global Young's modulus matched the assumed local value. According to the simulation results of the indentation splitting tensile tests, for all samples with varying w/c ratios, the properties of ITZ are approximately 20% of the properties of performance. Therefore, in this section, 20% of the paste's performance was directly assigned to the ITZ. The local mechanical properties of the single fibre pullout model are presented in Table 6. To accurately simulate the actual condition where the sample had adhered to the hex nut in the experiment, the nodes on the four sides of the model were set to neither tension nor compression. As shown in Fig.5.3b, a vertical displacement was applied to the fibre nodes at the top, covering a depth of 30 μm, to simulate the pullout tension force.

Table 6 Local mechanical properties of lattice elements in Fig.5.3b.

Phase		Young's modulus (GPa)	Compressive strength (MPa)	Tensile strength (MPa)
Fibre		12.5	50	50
Paste	w/c 0.3	22	280	22
	w/c 0.4	20	200	19
	w/c 0.5	16	140	16
ITZ	w/c 0.3	4.4	56	4.4
	w/c 0.4	4	40	3.8
	w/c 0.5	3.2	28	3.2

5.3 Result and Discussion

5.3.1 Experimental Result

Fig.5.4 presents the typical single fibre pullout curve of PVA fibre from cement based matrix, which can be divided into three main regimes [16]: (1) the stable debonding stage, where the load increases to P_a until the deboned length equals the embedded length of the fibre; (2) the slippage stage, where the fibre begins to slide from load P_b and the pullout is resisted solely by frictional forces; and (3) the slip-hardening stage, where the friction force increases linearly with the pullout distance, reaching the maximum load P_{max} before the fibre ruptures. The increasing pullout resistance in this stage is known as the slip-hardening effect and is characterized by the slip-hardening coefficient β [95]. Table 7 presents the values of various interface bonding properties, which include chemical bonding energy G_d, initial frictional bond τ_0, and slip-hardening coefficient β.

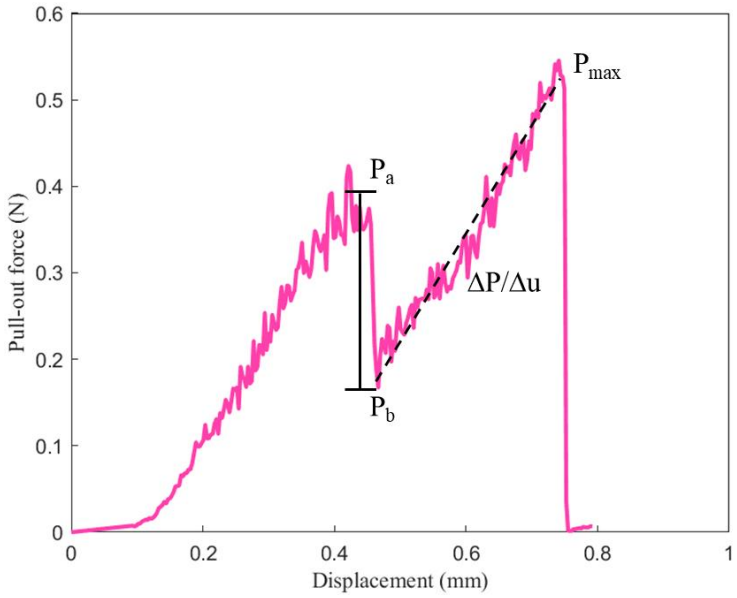

Fig.5.4 Representative results of single fibre pullout test

Most previous studies assume that the debonding process in the fibre pullout test is a tunnel crack propagation, where the pullout of the fibre is resisted by the debonding fracture energy of the tunnel-shaped crack [93]. This fracture energy, also known as the chemical bonding energy G_d, can be calculated by Eq. 7. The chemical bond energy for different types of materials at various w/c ratios is shown in Table 7. For CEM I, CEM III and CEM III+L, the values of G_d vary from 4.5 to 6.9, 1.2 to 2.6 and 1.0 to 2.7 J/m2, respectively. It is evident in CEM I and CEM III that as the w/c ratio increases, the chemical bond energy shows a significant decreasing trend. However, with the addition of limestone powder in CEM III+L, the group with a w/c ratio of 0.3 surprisingly has the lowest chemical bond energy, while the group with a w/c ratio of 0.4 reaches up to 2.31 J/m². In terms of frictional bond $\boldsymbol{\tau_0}$, CEM III+L shows the highest values at w/c of 0.3 with 2.99 MPa, but $\boldsymbol{\tau_0}$ stabilizes around 2 MPa for higher w/c ratios. CEM I displays relatively stable frictional bond strength, ranging from 1.82 MPa to 1.98 MPa, while CEM III exhibits a slight increase from 2.52 MPa at w/c of 0.3 to 2.88 MPa at w/c of 0.5. For all materials, τ_0 does not vary significantly with changes in the w/c ratio, though CEM III generally shows slightly higher values than the other two materials. Regarding the slip-hardening coefficient β, CEM III+L displays the highest value at w/c of 0.3 with 0.358, reflecting significant improvement in frictional resistance due to limestone powder addition. For CEM I, β varies but remains lower, ranging from 0.038 to 0.152, and CEM III shows considerable variability with values from 0.094 to 0.253. These findings indicate that CEM I has the strongest chemical bonds overall, the bonding properties of CEM III change notably with varying w/c ratios, and CEM III+L, especially the enhanced frictional resistance at lower w/c ratios, are significantly influenced by the presence of limestone. In terms of slip hardening

effect, CEM III+L exhibits the highest β, while CEM I shows the lowest values. However, similar to τ_0, β does not show significant variation with changes in the w/c ratio across the three materials. Comparing the trends in interface bonding properties from Table 7 with the splitting tensile strength in Fig. 3.18, it is evident that the trend of chemical bond energy is the same as the reference specimens. CEM I shows the highest test results, followed by CEM III+L, and finally CEM III. These results indicate that the chemical bond energy of the fibres does not depend on the splitting tensile strength of the ITZ, but rather shows a positive correlation with the inherent matrix strength. Previous chapters have demonstrated that the addition of limestone increases the strength of the ITZ. In the single fibre pullout tests conducted in this chapter, comparing the results for τ_0 and β of CEM III and CEM III+L shows that the addition of limestone enhances the frictional bond strength and the slip-hardening effect to some extent.

Table 7 PVA fibre-matrix interface bonding properties.

Material	w/c	Chemical bond energy G_d (J/m^2)	Frictional bond strength τ_0 (MPa)	Slip-hardening coefficient β
CEM I	0.3	6.89±4.33	1.82±0.45	0.038±0.086
	0.4	5.60±2.73	2.13±1.36	0.173±0.131
	0.5	4.46±2.82	1.98±0.93	0.152±0.076
CEM III	0.3	2.61±2.00	2.52±2.25	0.253±0.182
	0.4	2.17±1.83	2.32±1.39	0.094±0.085
	0.5	1.16±1.05	2.88±0.85	0.244±0.121
CEM III+L	0.3	1.03±0.89	2.99±1.58	0.358±0.123
	0.4	2.70±1.66	1.98±1.74	0.176±0.145
	0.5	2.31±1.19	2.21±1.01	0.240±0.087

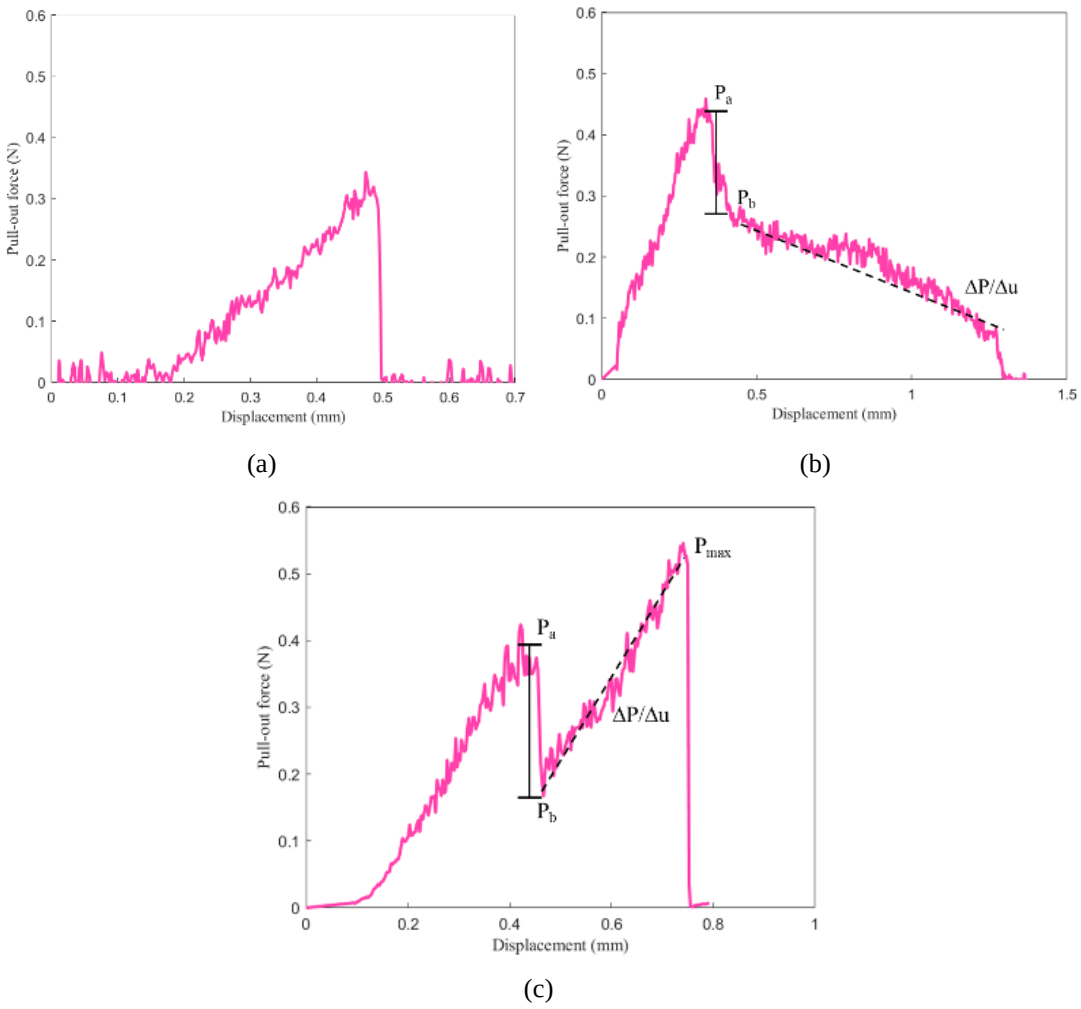

Fig.5.5 Schematic plot of the single fibre pullout test: (a)invalid; (b)fully pullout; (c)rupture after debonded.

All the curves from the single fibre pullout tests are included in Appendix A. In the figures, red circles indicate the points P_a and P_b used for calculations, and the red dashed line represents the calculated $\Delta P/\Delta U$. Fig.5.5 presents characteristic curves from three types of single-fibre pullout tests. "Invalid" indicates that the fibre broke before being fully debonded, showing only a distinct ascending segment without a sudden drop. "Fully pull out" indicates that the fibre was completely pulled out after being fully debonded, showing a relatively smooth descending segment in the curve. "Rupture after deboned" indicates that the fibre ruptured during slippage before reaching the full pullout length after being debonded. Table 8 summarises the number of specimens for each test result. Combining the data from Table 8 and the single fibre pullout test curves in Appendix A, it is evident that CEM I shows a distinct drop from P_a to P_b, indicating a strong chemical bond between the PVA fibres and the matrix. Most specimens with a w/c ratio of 0.3 were fully pulled out, but as the w/c ratio increased, the number of specimens where the fibre ruptured after debonding also increased. In contrast, for CEM III and CEM

III+L, the difference between P_a and P_b is not as pronounced, with fibres tending to break before fully pulling out, and some specimens not showing a clear deboned behaviour. This explains the results in Table 7, where the chemical bond energy for CEM I is significantly higher than for the other two materials. Literature [16] suggests that when fibres and matrix are non-chemically bonded, the P_a of the curve is very close to P_b. Unlike other polymer fibres with low surface energy, PVA fibre has strong surface chemical bonding properties. High chemical bonding between PVA fibre and matrix leads to an aggressive debonding process, with the ITZ having to carry an increasing shear force between fibre surface frictional debonding and the force caused by chemical debonding of ITZ microstructure decomposition from matrix bulk. In this experiment, the debonding mechanism of fibres in CEM III and CEM III+L may differ from that in CEM I. This requires further exploration of the formation of hydration products and chemical bonds on the fibre surface in the interphase in future research.

Table 8 Summary of the number of different types of test results

Material	w/c	Test number	Invalid	Fully pullout	Rupture after debonded
CEM I	0.3	10	0	8	2
	0.4	9	1	2	6
	0.5	9	3	0	6
CEM III	0.3	11	0	3	8
	0.4	16	4	7	5
	0.5	11	2	0	9
CEM III +L	0.3	13	2	1	10
	0.4	12	2	5	5
	0.5	13	3	2	8

5.3.2 Modelling Result

Fig.5.6 presents the comparison between the simulated load-displacement curve of single fibre pullout and those measured experimentally. In this analysis, the curves are divided into three phases for comparison: (1) load from 0 to P_a, where the fibre is not yet debonded; (2) load from P_a to P_b, where the fibre is fully debonded; (3) slippage regime after P_b, dominated by friction. At a w/c ratio of 0.3, the experimental results show that the initial load rises rapidly to about 0.4 N, then drops to 0.25 N at which point the fibre is fully debonded. Then it enters a phase of gradual load decrease, ending with the fibre being fully debonded. The simulation results for the first and second phases match the experimental results, but there is a significant difference in the slippage behaviour after full debonding. For tests with w/c ratios of 0.4 and 0.5, unlike the full pullout observed at a w/c ratio of 0.3, the fibre exhibits notable slip-hardening behaviour

after debonding and breaks during the slippage phase. The simulation results for a w/c ratio of 0.4 do not differ significantly from those for 0.3, but at a w/c ratio of 0.5, the simulated load curve shows a sudden drop, corresponding to greater resistance to chemical bonding observed in the experiments.

Overall, the simulation results align with the experimental results in the pre-slippage phases, but there are considerable differences in the slippage behaviour. This is because the current lattice model principle applies displacement in each analysis step, labelling and removing the critical beam element with the highest stress/strength ratio from the mesh. After the chemical debonding of the fibre, the model cannot further simulate the friction between the fibre and the matrix. To better simulate the slippage regime of fibre pullout, the model needs further refinement.

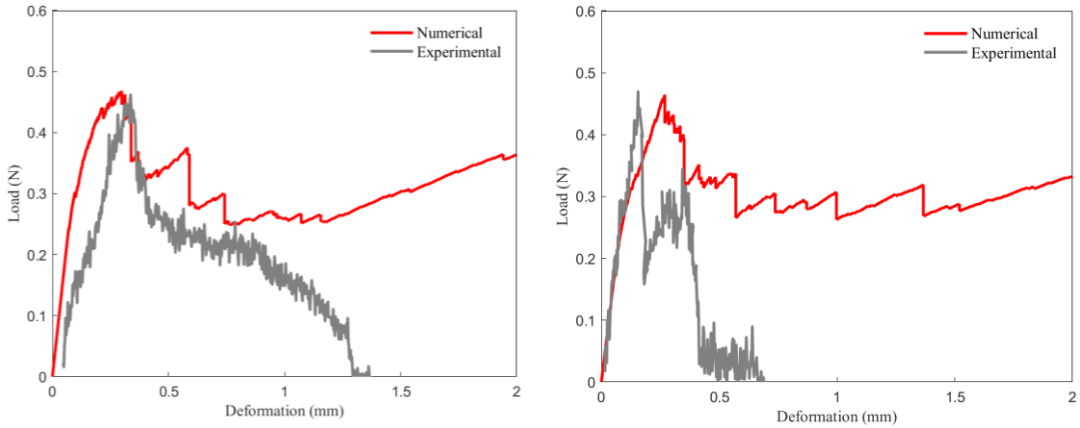

(a) (b)

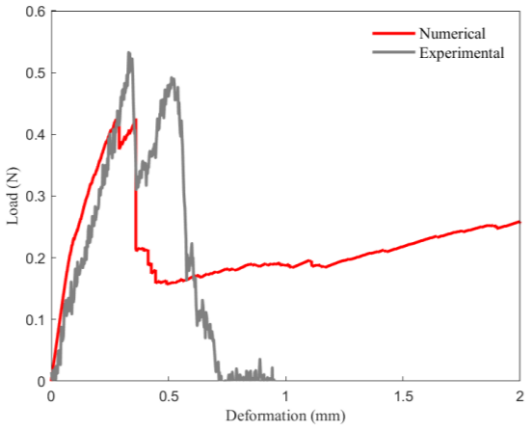

(c)

Fig.5.6 The experimental and numerical results of the single fibre pullout test: (a) w/c ratio of 0.3; (b) w/c ratio of 0.4; (c) w/c ratio of 0.5.

The simulated crack pattern of the single fibre pullout test, from the crack initiates to the breakage of the fibre, is presented in Fig.5.7. The figure only shows the crack development of the w/c ratio of 0.3. Although the simulation results for the other two w/c ratios differ from the 0.3 ratio, their simulated fracture behaviour are similar. As the weakest part of the specimen, the ITZ initiates cracking at the fibre-paste interface when a tensile stress is applied to the fibre. It is important to note that the red elements in the figure represent predefined transition elements between the fibre and the ITZ. As the displacement increases, the fractured ITZ elements gradually increase, forming a conical region; simultaneously, the red elements along the fibre surface also progressively fracture, corresponding to the chemically deboned surface of the fibre observed in experiments. Unlike the experimental results where most fibres with a w/c ratio of 0.3 are fully pulled out, in the simulations, all fibres break during the pullout process. According to the shear lag model of the fibre pullout process in [96], the stress is transferred from the fibre to the surrounding matrix by the interfacial shear stress. However, since α_M, representing the bending influence factor in Eq. 2, was set to 0.05 in this model, the transfer of interfacial shear stress was not effectively simulated. This leads to the fibre elements breaking completely before they are fully debonded. Furthermore, after the fibre breaks, the failed interface elements are deleted sequentially, failing to simulate the slippage regime observed in the experiment.

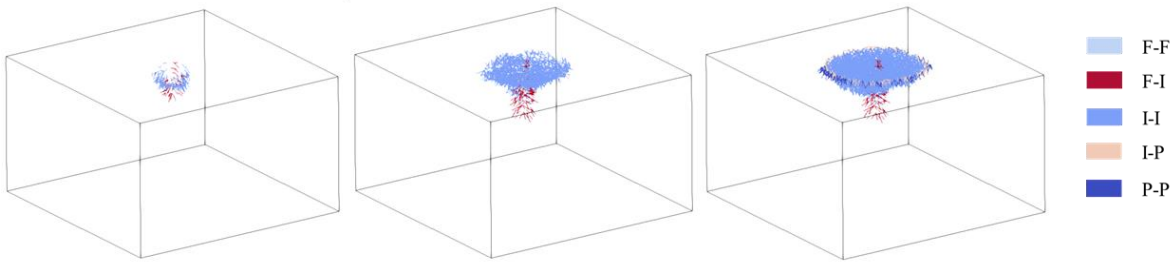

Fig.5.7 Simulated fracture patterns of micro-cube under different states: (a) Crack initiates at the centre of the upper part of the specimen; (b) crack propagates at the fibre and the ITZ around the upper end of the fibre; (c) fibre breaks, and the upper part of the fibre, along with the high porosity ITZ and a small portion of the low porosity paste is pulled out

5.4 Conclusions

The experiment and simulation of the single fibre pullout test were conducted in this chapter. The simulation utilized the model with a simplified microstructure described in Chapter 4, with modifications only to the model size and boundary conditions. The material properties of the

ITZ were input as 20% of the previously validated paste properties. The following conclusions can be drawn:

1. CEM I demonstrates the highest chemical bond energy (G_d) among the tested materials, decreasing significantly with an increase in the w/c ratio. In contrast, CEM III+L displays an inconsistent trend, with the highest G_d observed at a w/c ratio of 0.4. However, the experimental results for frictional bond strength (τ_0) and slip-hardening coefficient (β) do not exhibit significant trends or differences. The results indicate that the chemical bond energy of the fibres does not depend on the splitting tensile strength of the ITZ, but rather shows a positive correlation with the inherent matrix strength. Previous chapters have demonstrated that the addition of limestone increases the strength of the ITZ. In the single fibre pullout tests conducted in this chapter, comparing the results for τ_0 and β of CEM III and CEM III+L shows that the addition of limestone enhances the frictional bond strength and the slip-hardening effect to some extent.
2. The comparison between experimental and simulated single fibre pullout tests reveals that while the simulation accurately captures the initial load phases up to full debonding, significant discrepancies arise during the slippage regime. This is attributed to the input of since α_M, which underestimated the transfer of frictional forces between the fibre and the matrix post-debonding. As a result, the simulation fails to reproduce the gradual load decrease observed experimentally, particularly at higher w/c ratios where notable slip-hardening and fibre breakage occur.
3. The simulated crack patterns in the single fibre pullout test indicate that the fibre broke and pulled out a portion of the paste before fully debonded. The discrepancy between the simulated and experimental crack pattern may be attributed to the settings of the normal force influence factor and the bending influence factor in the lattice model. Further research is needed to identify appropriate factors to improve its accuracy in predicting the slippage behaviour of fibre pullout.

6

Conclusion and Recommendations

Chapter 6 summarizes the conclusions drawn from both experimental and numerical results and proposes recommendations for future research.

6.1 Conclusion

The main aim of the thesis is to develop a test method to evaluate the micromechanical properties of ITZ and to build a numerical model to investigate the fracture behaviour of specimens containing one single microfibre. An indentation splitting tensile test is developed and the discrete lattice fracture model is used as the numerical tool. To investigate the correlation between the splitting tensile test results and the single fibre pullout behaviour, Chapter 5 tested and simulated the single fibre pullout behaviour of three different materials. Each chapter of this thesis presents specific conclusions related to that segment of the research. Therefore, this chapter provides only the main conclusions and recommendations.

The mechanical properties, peak load, failure displacement, stiffness and fracture energy, were obtained from the indentation splitting tensile test in Chapter 3. Results show that the presence of fibres significantly reduced the peak load, stiffness, and fracture energy across all materials and w/c ratios, indicating an alteration in the surrounding microstructure of the cement matrix. The increase in the w/c ratio generally led to a decrease in peak load and stiffness, with no significant change in failure displacement, while fracture energy decreased for CEM I and CEM III but not for CEM III+L. Besides that, the addition of limestone powder (CEM III+L) enhanced the fracture energy and tensile strength of microcubes with fibre, likely due to the filler effect of the finely ground limestone improving ITZ microstructure, particularly at higher w/c ratios. Adding limestone to CEM III significantly enhances the strength of the specimens with fibre, even though it does not contribute noticeably to the reference microcubes. The findings revealed that the fabrication method ensured specimen integrity, and the indentation splitting test effectively assessed the tensile behaviour of the fibre-matrix interface.

In Chapter 4, lattice models with simplified and real microstructures were built. The experimental results obtained from Chapter 3 were used to calibrate the material properties input and validate the simulation results. The adopted mechanical properties of local phases are critical for the investigation in terms of load-displacement response and failure mechanism, so it is crucial to fit these parameters by designing experiments on specimens of the same size as well as under well-controlled boundary conditions. The modelling results of the simplified model indicate that the material properties of the ITZ are approximately 20% of the paste properties, regardless of the w/c ratio. Except for the simplified model, the lattice model with real microstructure was built based on a microstructure of cement paste prisms containing one single fibre obtained from XCT. For this model, two material assignment methods, thresholding and greyscale mapping, were compared. The simulation results showed significant differences

between the two methods, which may be attributed to the empirical parameters used to calculate tensile strength.

In Chapter 5, the pullout test results reveal that the chemical bond strength of CEM III and CEM III+L is significantly lower than that of CEM I. However, adding limestone to CEM III increases the β, making slip-hardening behaviour more pronounced. Therefore, when the splitting tensile strength of ITZ increases, it results in an increased load-resisting fibre pullout. This phenomenon can be very beneficial as long as the fibre tensile strength is not exceeded. The ITZ material parameter inputs obtained from Chapter 4 were used in the single fibre pullout simulation in Chapter 5. Experimental validation showed that the simulation results align well with the experimental results in the pre-slippage phase. However, despite the simulation accurately capturing the initial load phases up to full debonding, significant discrepancies arise during the slippage regime. This is attributed to the input parameter α_M, which underestimated the transfer of frictional forces between the fibre and the matrix post-debonding. As a result, the simulation fails to reproduce the gradual load decrease observed experimentally, particularly at higher w/c ratios where notable slip-hardening and fibre breakage occur.

Consequently, to design materials with significant strain-hardening and multiple-cracking behaviour under tension, the indentation splitting tensile test serves as an indirect tool to evaluate the tensile strength of the ITZ. The modelling results reveal that the mechanical properties of ITZ are approximately 20% of those of the paste, and this result can be upscaled to larger-scale simulations that consider the effects of ITZ. Additionally, the ideal input parameters for ITZ material can be determined through modelling. The combination of the indentation splitting tensile test and the lattice model offers an effective method for improving the interphase properties of FRC. Furthermore, the insights gained from this study can be applied to optimize the design and performance of FRC, potentially leading to cost savings and increased longevity in construction projects.

6.2 Recommendations

Due to time constraints, there are several limitations in the simulations of the indentation splitting tensile test in Chapter 3 and the single fibre pullout test in Chapter 5. Firstly, all models were only simulated for CEM I material. Future work should include simulations for CEM III and CEM III+L to compare the mechanical performance and fracture patterns among the three materials. In the simulations presented in Chapter 3, the material parameter inputs for both the

model with simplified and real microstructures were derived from previous studies. Given that cement is highly heterogeneous at the micro level, even different batches of the same type of cement can exhibit significant variations in chemical composition and hydration products. It would be ideal to conduct nanoindentation tests on specimens cast from the same batch of material to obtain accurate material properties for each phase. Furthermore, the model with real microstructure was significantly simplified, leading to a mismatch between the simulation and experimental results. In the future, the input parameters for the material properties need to be validated to ensure the model's accuracy to a reasonable extent. Additionally, the voxel size of the model should match the interaction volume of the nanoindentation when testing material inputs for each phase. When using greyscale mapping to input material parameters, the empirical model for tensile strength should be validated by experimental results. Finally, in the simulation of single fibre pullout in Chapter 5, the lattice model requires further refinement to accurately simulate the slippage behaviour after fibre fracture.

Appendix

A. The experimental results of the single fibre pullout test

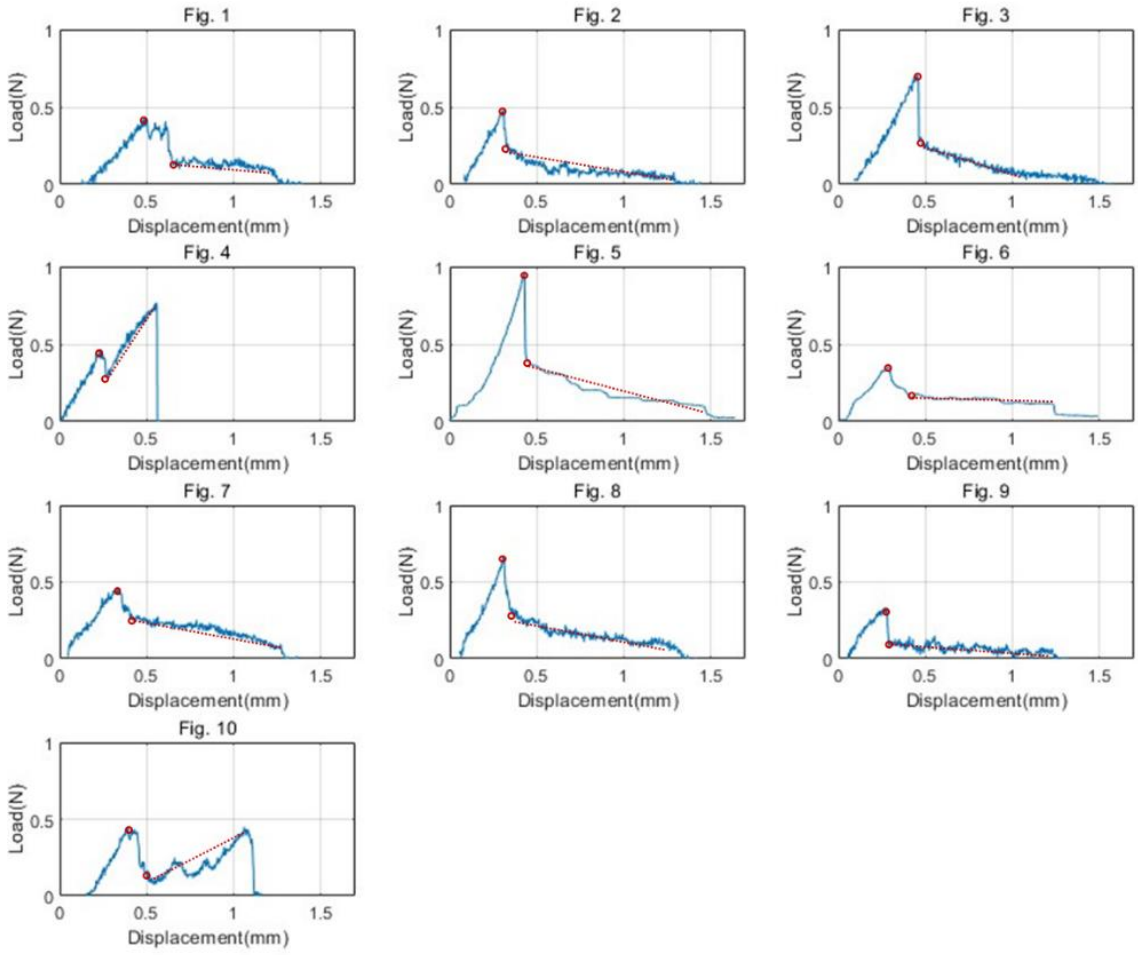

Fig. A.1 Single fibre pullout curves of CEM I with a w/c ratio of 0.3

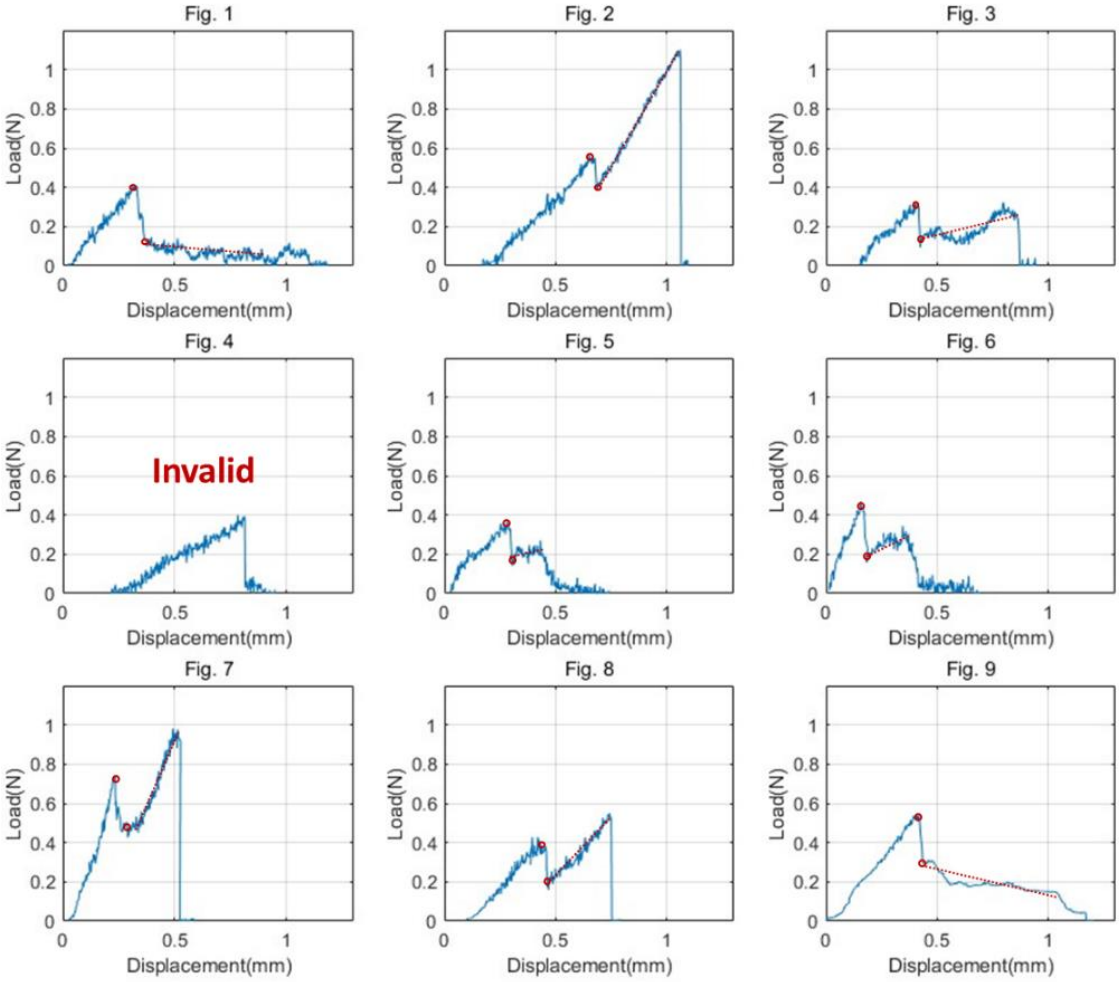

Fig. A.2 Single fibre pullout curves of CEM I with a w/c ratio of 0.4

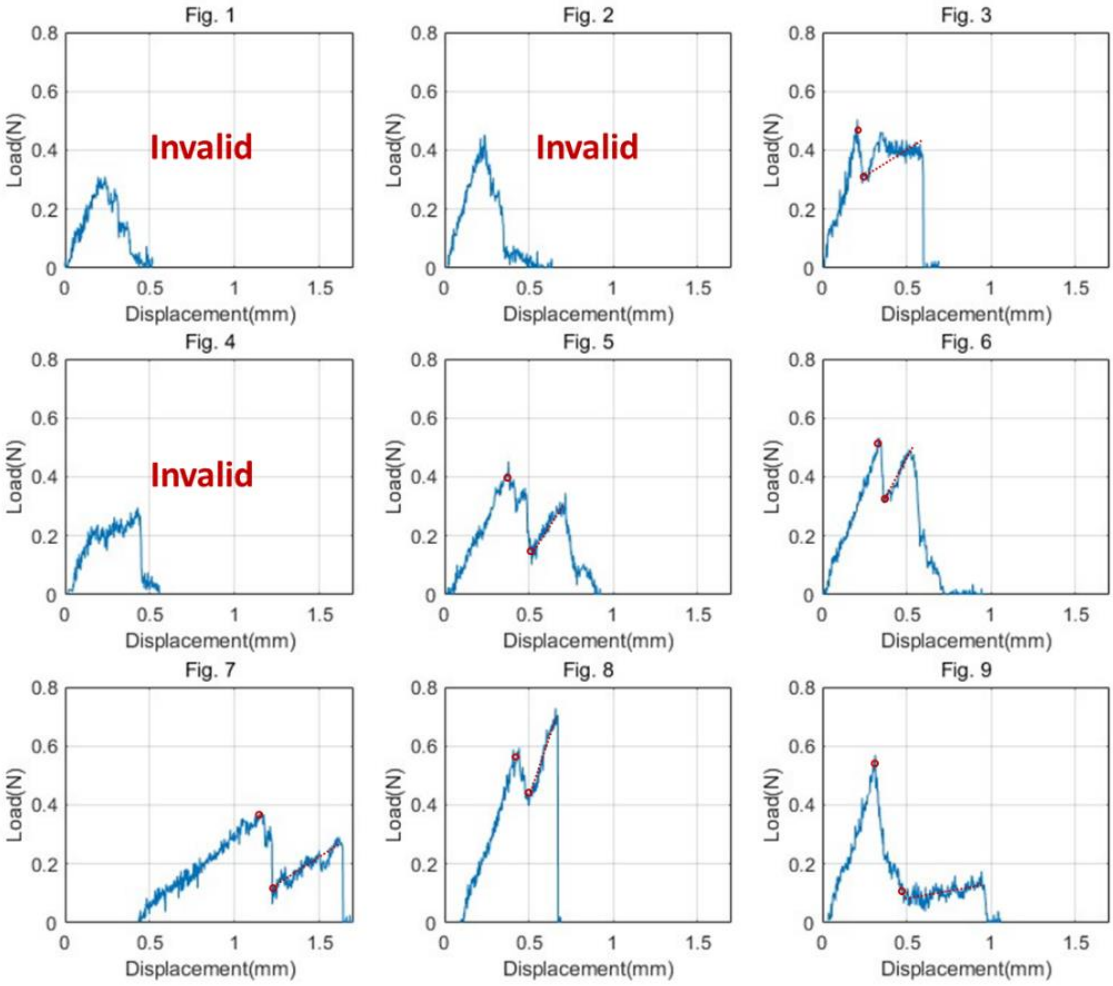

Fig. A.3 Single fibre pullout curves of CEM I with a w/c ratio of 0.5

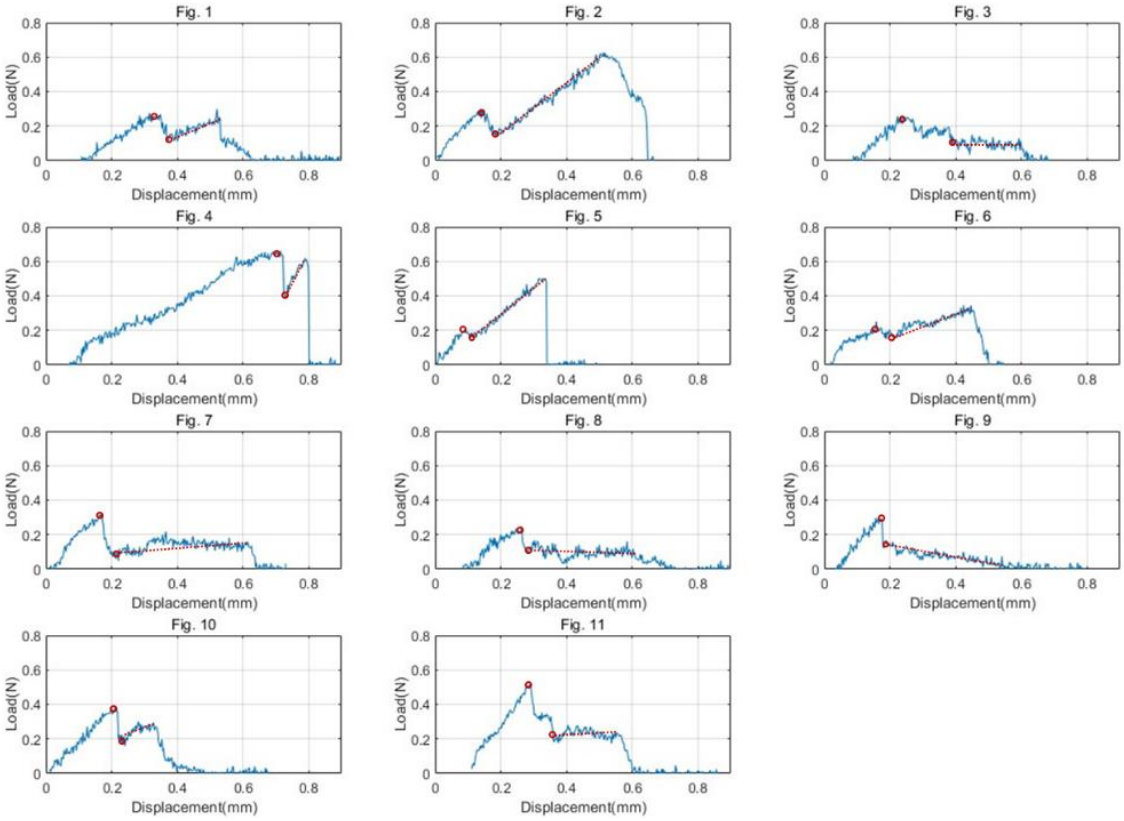

Fig. A.4 Single fibre pullout curves of CEM III with a w/c ratio of 0.3

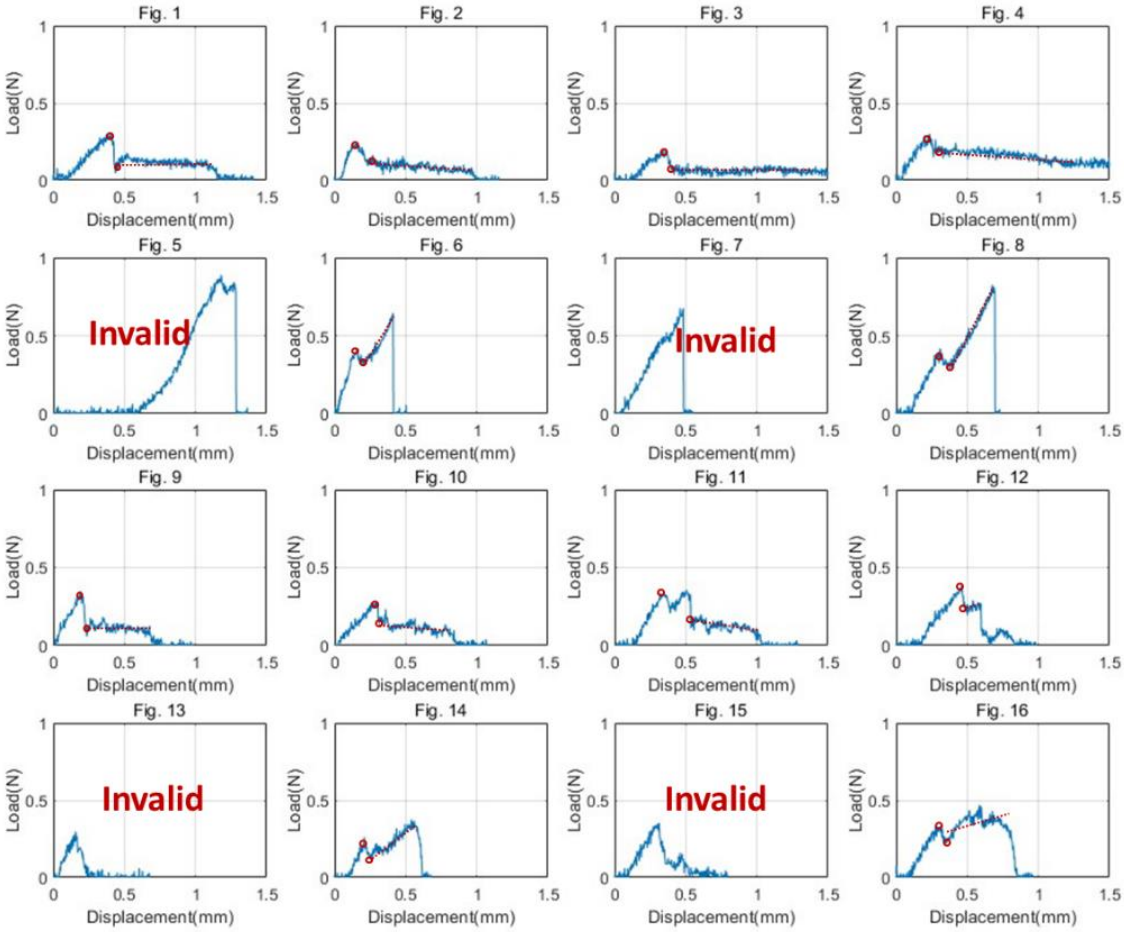

Fig. A.5 Single fibre pullout curves of CEM III with a w/c ratio of 0.4

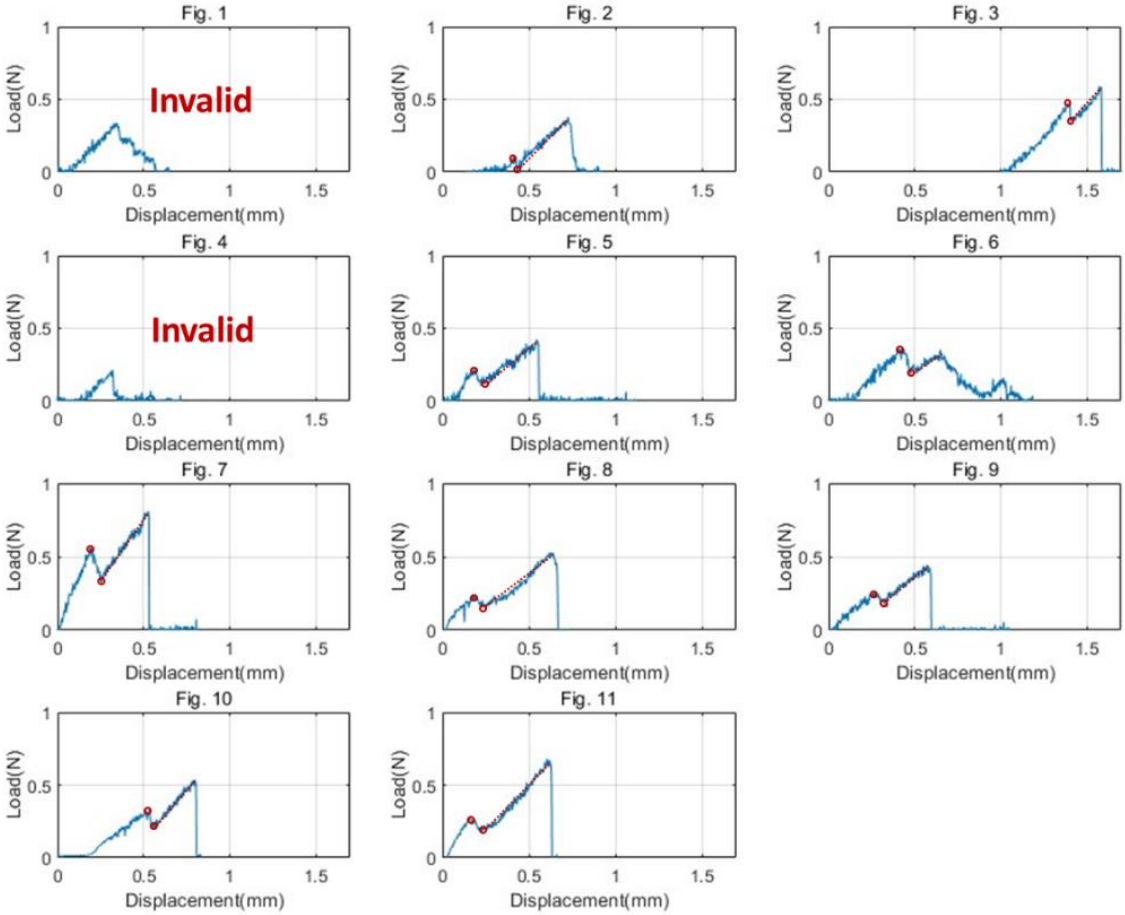

Fig. A.6 Single fibre pullout curves of CEM III with a w/c ratio of 0.5

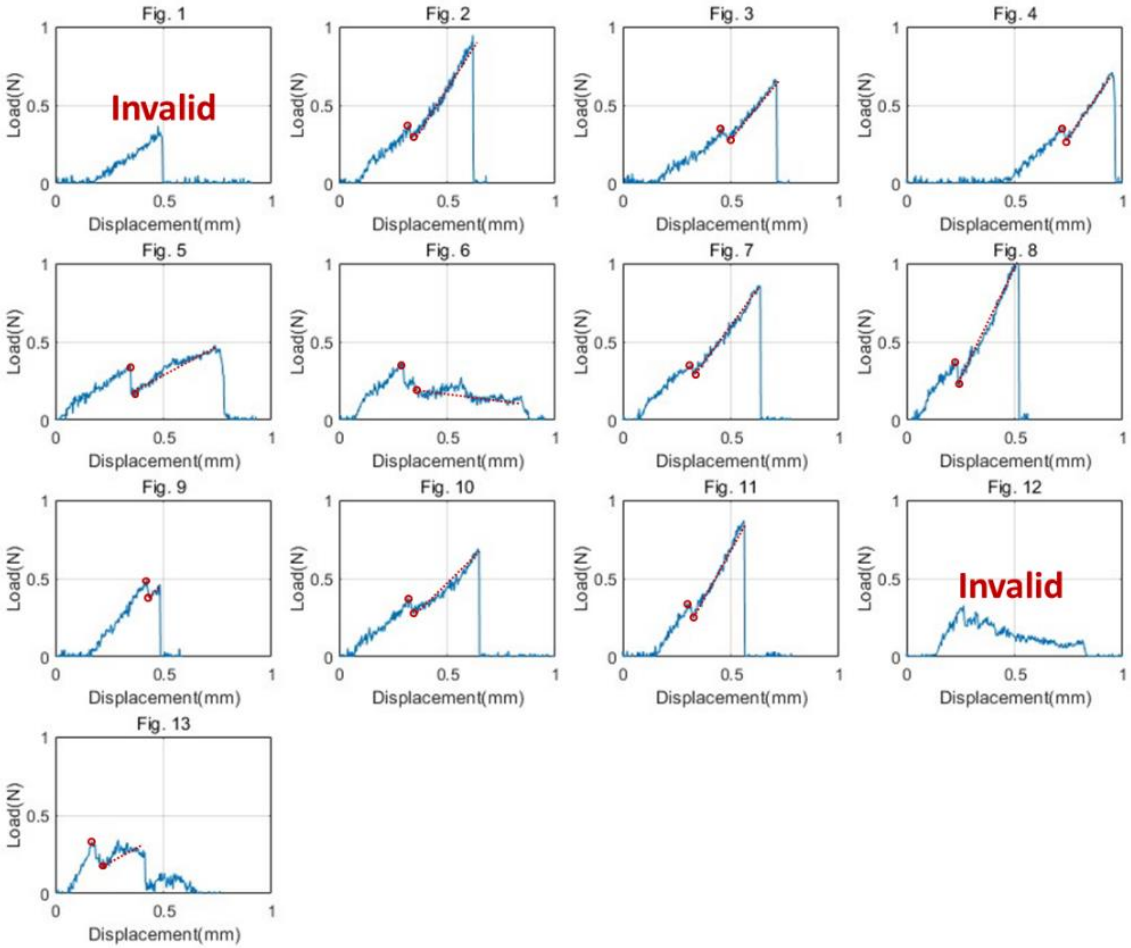

Fig. A.7 Single fibre pullout curves of CEM III+L with a w/c ratio of 0.3

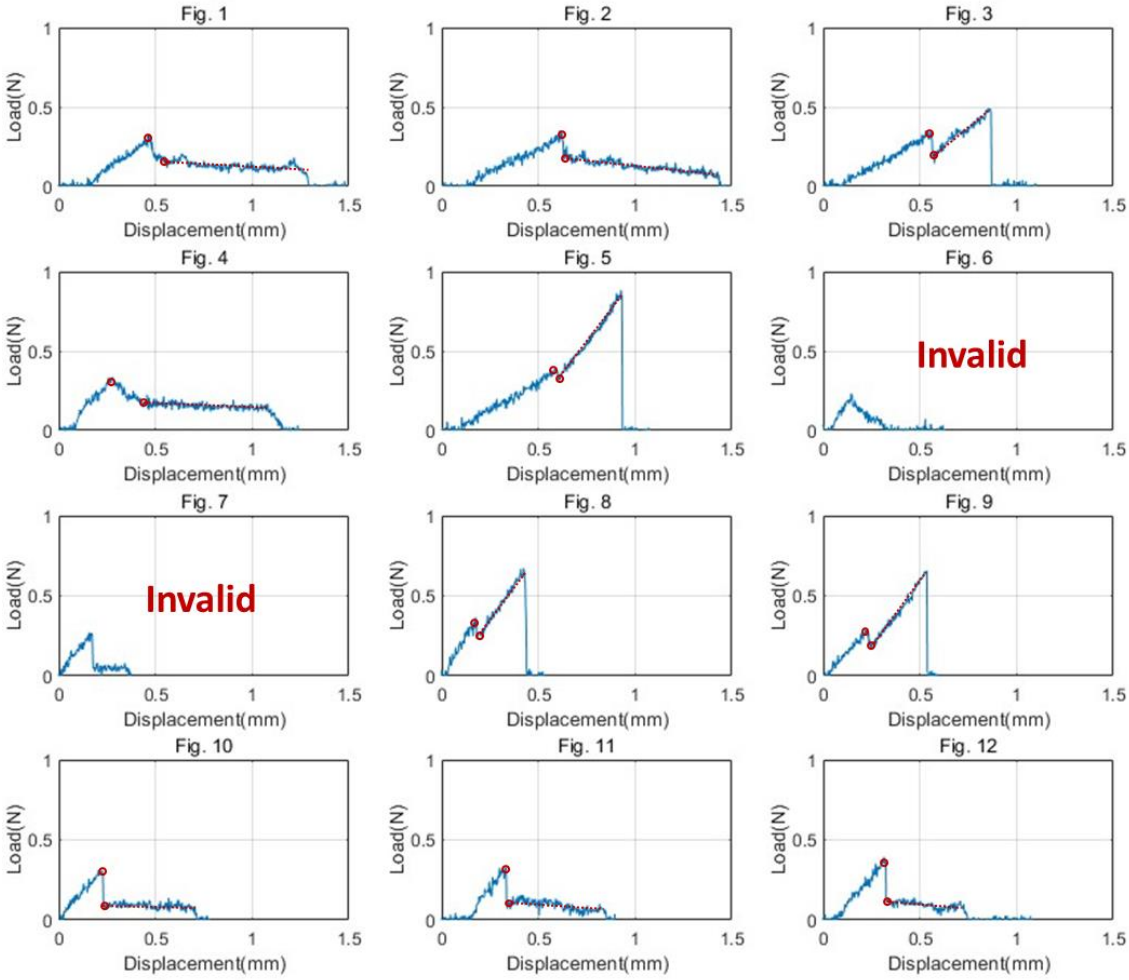

Fig. A.8 Single fibre pullout curves of CEM III+L with a w/c ratio of 0.4

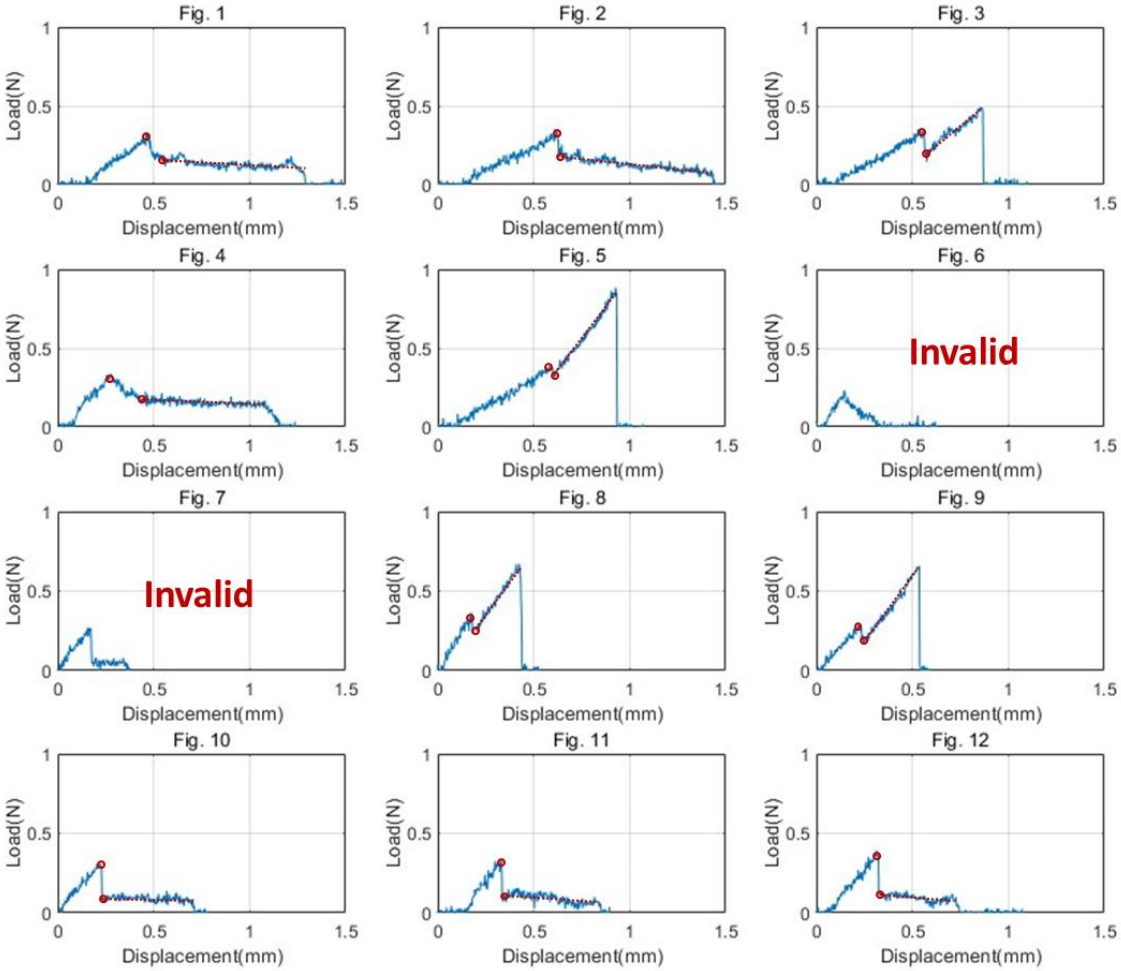

Fig. A.9 Single fibre pullout curves of CEM III+L with a w/c ratio of 0.5

Bibliography

1. Zollo, R.F., *Fiber-reinforced concrete: an overview after 30 years of development.* Cement and Concrete Composites, 1997. **19**(2): p. 107-122.
2. Tran, N.P., et al., *Microstructural characterisation of cementitious composite incorporating polymeric fibre: A comprehensive review.* Construction and Building Materials, 2022. **335**.
3. Xu, K., et al., *In-situ microtomography image segmentation for characterizing strain-hardening cementitious composites under tension using machine learning.* Cement and Concrete Research, 2023. **169**.
4. Teklal, F., et al., *A review of analytical models to describe pullout behavior – Fiber/matrix adhesion.* Composite Structures, 2018. **201**: p. 791-815.
5. Zhang, W., et al., *Experimental and numerical analysis of interfacial bonding strength of polyoxymethylene reinforced cement composites.* Construction and Building Materials, 2019. **207**: p. 1-9.
6. Zheng, Z. and D. Feldman, *Synthetic fibre-reinforced concrete.* Progress in Polymer Science, 1995. **20**(2): p. 185-210.
7. He, S., et al., *Distribution of porosity surrounding a microfiber in cement paste.* Cement and Concrete Composites, 2023. **142**.
8. *Effects of Transition Zone Densification On Fiber/Cement Paste Bond Strength Improvement.*
9. Kanda, T. and V.C. Li, *Interface property and apparent strength of high-strength hydrophilic fiber in cement matrix.* Journal of Materials in Civil Engineering, 1998. **10**(1): p. 5-13.
10. Zhandarov, S., *Characterization of fiber/matrix interface strength: applicability of different tests, approaches and parameters.* Composites Science and Technology, 2005. **65**(1): p. 149-160.
11. Chan, Y.-W. and V.C. Li, *Effects of transition zone densification on fiber/cement paste bond strength improvement.* Advanced Cement Based Materials, 1997. **5**(1): p. 8-17.
12. Li, V.C., et al., *Interface tailoring for strain-hardening polyvinyl alcohol-engineered cementitious composite (PVA-ECC).* Materials Journal, 2002. **99**(5): p. 463-472.
13. Wang, X.H., et al., *Application of nanoindentation testing to study of the interfacial transition zone in steel fiber reinforced mortar.* Cement and Concrete Research, 2009. **39**(8): p. 701-715.
14. Xu, L., F. Deng, and Y. Chi, *Nano-mechanical behavior of the interfacial transition zone between steel-polypropylene fiber and cement paste.* Construction and Building Materials, 2017. **145**: p. 619-638.
15. He, S. and E.-H. Yang, *Strategic strengthening of the interfacial transition zone (ITZ) between microfiber and cement paste matrix with carbon nanofibers (CNFs).* Cement and Concrete Composites, 2021. **119**.
16. Redon, C., et al., *Measuring and Modifying Interface Properties of PVA Fibers in ECC Matrix.* Journal of Materials in Civil Engineering, 2001. **13**(6): p. 399-406.

17. He, S., et al., *Effects of bacteria-embedded polylactic acid (PLA) capsules on fracture properties of strain hardening cementitious composite (SHCC).* Engineering Fracture Mechanics, 2022. **268**: p. 108480.
18. Romualdi, J.P. and J.A. Mandel. *Tensile strength of concrete affected by uniformly distributed and closely spaced short lengths of wire reinforcement*. in *Journal Proceedings*. 1964.
19. Naaman, A., S. Shah, and S. Freiman, *Fracture and Multiple Cracking of Cementitious Composites*, in *Fracture Mechanics Applied to Brittle Materials*. 1979, ASTM International. p. 0.
20. Li, V.C., *From micromechanics to structural engineering-the design of cementitous composites for civil engineering applications.* 1993.
21. Li, V.C., *Tailoring ECC for Special Attributes: A Review.* International Journal of Concrete Structures and Materials, 2012. **6**(3): p. 135-144.
22. Li, V.C., D.K. Mishra, and H.C. Wu, *Matrix design for pseudo-strain-hardening fibre reinforced cementitious composites.* Materials and Structures, 1995. **28**(10): p. 586-595.
23. Li, V.C., S. Wang, and C. Wu, *Tensile strain-hardening behavior or polyvinyl alcohol engineered cementitious composite (PVA-ECC).* ACI Materials Journal, 2001. **98**(6): p. 483-492.
24. Li, V.C. and T. Kanda, *Engineered cementitious composites for structural applications.* Journal of Materials in Civil Engineering, 1998. **10**(2): p. 66-69.
25. Lokuge, W., S. Setunge, and G. Sanjayan. *Lateral reinforcement requirement in high-strength concrete columns*. in *Proc, International Conference" Our World in Concrete and Structures*. 2000.
26. Richard, P. and M. Cheyrezy, *Composition of reactive powder concretes.* Cement and Concrete Research, 1995. **25**(7): p. 1501-1511.
27. Yoo, D.-Y. and N. Banthia, *High-performance strain-hardening cementitious composites with tensile strain capacity exceeding 4%: A review.* Cement and Concrete Composites, 2022. **125**.
28. Yoo, D.-Y., et al., *An experimental study on pullout and tensile behavior of ultra-high-performance concrete reinforced with various steel fibers.* Construction and Building Materials, 2019. **206**: p. 46-61.
29. Hao, Y., et al., *Enhancing fiber/matrix bonding in polypropylene fiber reinforced cementitious composites by microbially induced calcite precipitation pre-treatment.* Cement and Concrete Composites, 2018. **88**: p. 1-7.
30. Zhou, A., et al., *Interfacial performance of aramid, basalt and carbon fiber reinforced polymer bonded concrete exposed to high temperature.* Composites Part A: Applied Science and Manufacturing, 2020. **131**: p. 105802.
31. Lee, Y., S.-T. Kang, and J.-K. Kim, *Pullout behavior of inclined steel fiber in an ultra-high strength cementitious matrix.* Construction and Building Materials, 2010. **24**(10): p. 2030-2041.
32. Kim, J.-K. and Y.-W. Mai, *Engineered interfaces in fiber reinforced composites*. 1998: Elsevier.
33. Lin, C., et al., *Bonding property between fiber and cementitious matrix: A critical review.* Construction and Building Materials, 2023. **378**.
34. di Prisco, M., G. Plizzari, and L. Vandewalle, *Fibre reinforced concrete: new design perspectives.* Materials and Structures, 2009. **42**(9): p. 1261-1281.
35. Piggott, M.R., *The effect of the interface/interphase on fiber composite properties.* Polymer Composites, 1987. **8**(5): p. 291-297.

36. Plueddemann, E.P. *Interfaces in polymer matrix composites*. 1974.
37. Kim, J.-K. and Y.-W. Mai, *Interfaces in Composites*, in *Materials Science and Technology*.
38. Camargo, M.M., et al., *A Review on Natural Fiber-Reinforced Geopolymer and Cement-Based Composites.* Materials, 2020. **13**(20): p. 4603.
39. Azeem, M. and M. Azhar Saleem, *Role of electrostatic potential energy in carbon nanotube augmented cement paste matrix.* Construction and Building Materials, 2020. **239**: p. 117875.
40. Meng, W. and K.H. Khayat, *Mechanical properties of ultra-high-performance concrete enhanced with graphite nanoplatelets and carbon nanofibers.* Composites Part B: Engineering, 2016. **107**: p. 113-122.
41. Lu, M., et al., *Improved interfacial strength of SiO2 coated carbon fiber in cement matrix.* Cement and Concrete Composites, 2018. **91**: p. 21-28.
42. Velazco, G., K. Visalvanich, and S.P. Shah, *Fracture behavior and analysis of fiber reinforced concrete beams.* Cement and Concrete Research, 1980. **10**(1): p. 41-51.
43. Mobasher, B., C. Ouyang, and S.P. Shah, *Modeling of fiber toughening in cementitious materials using an R-curve approach.* International Journal of Fracture, 1991. **50**(3): p. 199-219.
44. Thouless, M.D. and A.G. Evans, *Effects of pullout on the mechanical properties of ceramic-matrix composites.* Acta Metallurgica, 1988. **36**(3): p. 517-522.
45. Stang, H., *Significance of shrinkage-induced clamping pressure in fiber-matrix bonding in cementitious composite materials.* Advanced Cement Based Materials, 1996. **4**(3): p. 106-115.
46. Mandell, J., J. Chen, and F. McGarry, *A microdebonding test for in situ assessment of fibre/matrix bond strength in composite materials.* International Journal of Adhesion and Adhesives, 1980. **1**(1): p. 40-44.
47. Sakulich, A.R. and V.C. Li, *Nanoscale characterization of engineered cementitious composites (ECC).* Cement and Concrete Research, 2011. **41**(2): p. 169-175.
48. He, S., Z. Li, and E.-H. Yang, *Quantitative characterization of anisotropic properties of the interfacial transition zone (ITZ) between microfiber and cement paste.* Cement and Concrete Research, 2019. **122**: p. 136-146.
49. Kelly, A. and W.R. Tyson, *Tensile properties of fibre-reinforced metals: Copper/tungsten and copper/molybdenum.* Journal of the Mechanics and Physics of Solids, 1965. **13**(6): p. 329-350.
50. Fraser, W.A., et al., *Evaluation of surface treatments for fibers in composite materials.* Polymer Composites, 1983. **4**(4): p. 238-248.
51. Zhang, H., B. Šavija, and E. Schlangen, *Combined experimental and numerical study on micro-cube indentation splitting test of cement paste.* Engineering Fracture Mechanics, 2018. **199**: p. 773-786.
52. Kasiri, S., G. Reilly, and D. Taylor, *Wedge Indentation Fracture of Cortical Bone: Experimental Data and Predictions.* Journal of Biomechanical Engineering, 2010. **132**(8).
53. Sajzew, R., R. Limbach, and L. Wondraczek, *Deformation and Fracture of Silica Glass Fiber Under Sharp Wedge-Indentation.* Frontiers in Materials, 2020. **7**.

54. Hsueh, C.-H., *Interfacial debonding and fiber pullout stresses of fiber-reinforced composites.* Materials Science and Engineering: A, 1990. **123**(1): p. 1-11.
55. Stang, H. and S.P. Shah, *Failure of fibre-reinforced composites by pullout fracture.* Journal of Materials Science, 1986. **21**(3): p. 953-957.
56. Gao, Y.C., Y.W. Mai, and B. Cotterell, *Fracture of fiber-reinforced materials.* ZAMP Zeitschrift für angewandte Mathematik und Physik, 1988. **39**(4): p. 550-572.
57. Cox, H.L., *The elasticity and strength of paper and other fibrous materials.* British Journal of Applied Physics, 1952. **3**(3): p. 72-79.
58. Hsueh, C.-H., *Interfacial debonding and fiber pullout stresses of fiber-reinforced composites III: With residual radial and axial stresses.* Materials Science and Engineering: A, 1991. **145**(2): p. 135-142.
59. Hsueh, C.-H., *Interfacial debonding and fiber pullout stresses of fiber-reinforced composites IV: sliding due to residual stresses.* Materials Science and Engineering: A, 1991. **145**(2): p. 143-150.
60. Hsueh, C.-H., *Interfacial debonding and fiber pullout stresses of fiber-reinforced composites Part V. With a viscous interface.* Materials Science and Engineering: A, 1991. **149**(1): p. 1-9.
61. Nairn, J.A., *On the use of shear-lag methods for analysis of stress transfer in unidirectional composites.* Mechanics of Materials, 1997. **26**(2): p. 63-80.
62. Nairn, J.A., *A variational mechanics analysis of the stresses around breaks in embedded fibers.* Mechanics of Materials, 1992. **13**(2): p. 131-154.
63. Jiang, Y., W. Guo, and H. Yang, *Numerical studies on the effective shear modulus of particle reinforced composites with an inhomogeneous inter-phase.* Computational Materials Science, 2008. **43**(4): p. 724-731.
64. Wang, J., S.L. Crouch, and S.G. Mogilevskaya, *Numerical modeling of the elastic behavior of fiber-reinforced composites with inhomogeneous interphases.* Composites Science and Technology, 2006. **66**(1): p. 1-18.
65. Shen, L. and J. Li, *Homogenization of a fibre/sphere with an inhomogeneous interphase for the effective elastic moduli of composites.* Proceedings of the Royal Society A: Mathematical, Physical and Engineering Sciences, 2005. **461**(2057): p. 1475-1504.
66. Jayaraman, K. and K.L. Reifsnider, *Residual Stresses in a Composite with Continuously Varying Young's Modulus in the Fiber/Matrix Interphase.* Journal of Composite Materials, 1992. **26**(6): p. 770-791.
67. Jayaraman, K. and K.L. Reifsnider, *The interphase in unidirectional fiber-reinforced epoxies: Effect on residual thermal stresses.* Composites Science and Technology, 1993. **47**(2): p. 119-129.
68. Arain, M.F., et al., *Experimental and numerical study on tensile behavior of surface modified PVA fiber reinforced strain-hardening cementitious composites (PVA-SHCC).* Construction and Building Materials, 2019. **217**: p. 403-415.
69. Zhang, C., et al., *Numerical and analytical modeling of fiber-matrix bond behaviors of high performance cement composite.* Cement and Concrete Research, 2019. **125**.
70. Jia, Y., Z. Chen, and W. Yan, *A numerical study on carbon nanotube–hybridized carbon fibre pullout.* Composites Science and Technology, 2014. **91**: p. 38-44.

71. Liu, F., et al., *Microstructural characteristics and their impact on mechanical properties of steel-PVA fiber reinforced concrete.* Cement and Concrete Composites, 2021. **123**: p. 104196.
72. Lee, S.F. and S. Jacobsen, *Study of interfacial microstructure, fracture energy, compressive energy and debonding load of steel fiber-reinforced mortar.* Materials and Structures, 2011. **44**(8): p. 1451-1465.
73. Luković, M., E. Schlangen, and G. Ye, *Combined experimental and numerical study of fracture behaviour of cement paste at the microlevel.* Cement and Concrete Research, 2015. **73**: p. 123-135.
74. Zhang, H., et al., *Microscale Testing and Modelling of Cement Paste as Basis for Multi-Scale Modelling.* Materials (Basel), 2016. **9**(11).
75. *A review of nanoindentation continuous stiffness measurement technique and its applications.*
76. Kim, J.-K. and Y.-w. Mai, *High strength, high fracture toughness fibre composites with interface control—A review.* Composites Science and Technology, 1991. **41**(4): p. 333-378.
77. Petersson, P.E., *Fracture energy of concrete: Practical performance and experimental results.* Cement and Concrete Research, 1980. **10**(1): p. 91-101.
78. Yoo, D.-Y., Y.-S. Yoon, and N. Banthia, *Predicting the post-cracking behavior of normal- and high-strength steel-fiber-reinforced concrete beams.* Construction and Building Materials, 2015. **93**: p. 477-485.
79. Khalilpour, S., E. BaniAsad, and M. Dehestani, *A review on concrete fracture energy and effective parameters.* Cement and Concrete Research, 2019. **120**: p. 294-321.
80. Zhuang, W., et al., *Impact of micromechanics on dynamic compressive behavior of ultra-high performance concrete containing limestone powder.* Composites Part B: Engineering, 2022. **243**.
81. Penn, L.S. and C.T. Chou, *Identification of Factors Affecting Single Filament Pullout Test Results.* Journal of Composites Technology & Research, 1990. **12**: p. 164-171.
82. Kahl, C., J. Bagnucki, and J.A.-O. Zarges, *Demonstration of Hybrid Effect in Single Fiber Pullout Tests for Glass/Cellulose-Reinforced Polypropylene with Different Fiber-Matrix Adhesions. LID - 10.3390/polym14132517 [doi] LID - 2517.* (2073-4360 (Electronic)).
83. Qian, Z. *Multiscale Modeling of Fracture Processes in Cementitious Materials*. 2012.
84. Lilliu, G. and J.G.M. van Mier, *3D lattice type fracture model for concrete.* Engineering Fracture Mechanics, 2003. **70**(7): p. 927-941.
85. Qian, Z., et al., *Modeling Framework for Fracture in Multiscale Cement-Based Material Structures.* Materials (Basel), 2017. **10**(6).
86. Schlangen, E. and E.J. Garboczi, *Fracture simulations of concrete using lattice models: Computational aspects.* Engineering Fracture Mechanics, 1997. **57**(2): p. 319-332.
87. Zhang, H., et al., *Combined experimental and numerical study of uniaxial compression failure of hardened cement paste at micrometre length scale.* Cement and Concrete Research, 2019. **126**.
88. Zhang, M. and A.P. Jivkov, *Microstructure-informed modelling of damage evolution in cement paste.* Construction and Building Materials, 2014. **66**: p. 731-742.

89. Jennings, H.M., et al., *A multi-technique investigation of the nanoporosity of cement paste.* Cement and Concrete Research, 2007. **37**(3): p. 329-336.
90. Constantinides, G. and F.-J. Ulm, *The effect of two types of C-S-H on the elasticity of cement-based materials: Results from nanoindentation and micromechanical modeling.* Cement and Concrete Research, 2004. **34**(1): p. 67-80.
91. Hu, C. and Z. Li, *Micromechanical investigation of Portland cement paste.* Construction and Building Materials, 2014. **71**: p. 44-52.
92. Zhang, H., et al., *Experimentally informed micromechanical modelling of cement paste: An approach coupling X-ray computed tomography and statistical nanoindentation.* Composites Part B: Engineering, 2019. **157**: p. 109-122.
93. Lin, Z., T. Kanda, and V.C. Li, *On interface property characterization and performance of fiber reinforced cementitious composites.* 1999.
94. Abdallah, S. and D.W.A. Rees, *Comparisons Between Pullout Behaviour of Various Hooked-End Fibres in Normal–High Strength Concretes.* International Journal of Concrete Structures and Materials, 2019. **13**(1).
95. Lin, Z. and V.C. Li, *Crack bridging in fiber reinforced cementitious composites with slip-hardening interfaces.* Journal of the Mechanics and Physics of Solids, 1997. **45**(5): p. 763-787.
96. *Interfacial Debonding and Fiber Pullout Stresses of Fiber-reinforced Composites.*